



UPPSALA
UNIVERSITET

*Digital Comprehensive Summaries of Uppsala Dissertations
from the Faculty of Science and Technology 1938*

Atomistic Modelling of Low Dimensional Materials for Energy Harvesting and Gas Sensing Applications

S. RABAB NAQVI



ACTA
UNIVERSITATIS
UPSALIENSIS
UPPSALA
2020

ISSN 1651-6214
ISBN 978-91-513-0955-2
urn:nbn:se:uu:diva-409006

Dissertation presented at Uppsala University to be publicly examined in Polhemsalen, Ångströmlaboratoriet, Lägerhyddsvägen 1, Uppsala, Thursday, 11 June 2020 at 10:00 for the degree of Doctor of Philosophy. The examination will be conducted in English. Faculty examiner: Professor Abir De Sarkar (Institute of Nano Science and Technology, Mohali, India).

Abstract

Naqvi, S. R. 2020. Atomistic Modelling of Low Dimensional Materials for Energy Harvesting and Gas Sensing Applications. *Digital Comprehensive Summaries of Uppsala Dissertations from the Faculty of Science and Technology* 1938. 93 pp. Uppsala: Acta Universitatis Upsaliensis. ISBN 978-91-513-0955-2.

Energy crisis and pollution are the two biggest issues of the present times which are extremely important to address on priority. Scientists/Researchers are trying to explore and create alternate means of energy production which are sustainable and free from greenhouse emissions. Use of the hydrogen (H_2) as an energy carrier can promise energy sustainability, economic viability, and environmental friendliness. H_2 is abundant in nature and delivers the highest energy density compared to all types of fossil fuels. However, the gaseous nature of the H_2 makes its storage difficult for practical applications. Previously employed H_2 storage strategies (liquefaction and pressurized storage) suffer from economic and safety concerns. H_2 storage in solid-state materials via non-dissociative adsorption is the most suitable technique. However, adsorption energies of the H_2 with the storage medium are typically very weak therefore operations under ambient working conditions are not possible. We used density functional theory to design the H_2 storage media, which are capable to adsorb H_2 in a non-dissociative manner with high gravimetric capacity and adequate adsorption energies for storage under the ambient conditions. Our findings point to the fact that the H_2 adsorption on the functionalized nanostructures is the most efficient approach for the materials based storage. Furthermore, for environmental safety and monitoring perspective, we investigated and proposed novel two-dimensional nanomaterials that are capable to sense and capture hazardous gases from the environment. In short, this thesis work is an attempt towards designing efficient materials for H_2 based energy harvesting and gas sensing applications.

Keywords: Density functional theory, Low dimensional materials, Energy harvesting, Hydrogen storage, Gas Sensing

S. Rabab Naqvi, Department of Physics and Astronomy, Materials Theory, Box 516, Uppsala University, SE-751 20 Uppsala, Sweden.

© S. Rabab Naqvi 2020

ISSN 1651-6214

ISBN 978-91-513-0955-2

urn:nbn:se:uu:diva-409006 (<http://urn.kb.se/resolve?urn=urn:nbn:se:uu:diva-409006>)

Dedicated to my beloved parents & family

List of Papers

This thesis is based on the following papers, which are referred to in the text by their Roman numerals.

- I. **Manipulating energy storage characteristics of ultrathin boron carbide monolayer under varied scandium doping**
S. R. Naqvi, T. Hussain, P. Panigrahi, W. Luo and R. Ahuja. RSC. Adv. **7**, 8598, (2017)
- II. **Hexagonal boron nitride (h-BN) sheets decorated with OLi, ONa, and Li₂F molecules for enhanced energy storage**
S. R. Naqvi, G. S. Rao, W. Luo, R. Ahuja and T. Hussain. Chem-PhysChem **18**, 513, (2017)
- III. **Metallized siligraphene nanosheets (SiC₇) as high capacity hydrogen storage materials**
S. R. Naqvi, T. Hussain, W. Luo and R. Ahuja. Nano Research **11**, 3802, (2018)
- IV. **Exploring doping characteristics of various adatoms on single-layer stanene**
S. R. Naqvi, T. Hussain, W. Luo, and R. Ahuja. J. Phys. Chem. C **121**, 7667, (2017)
- V. **Light metal decorated graphdiyne nanosheets for reversible hydrogen storage**
P. Panigrahi, A. K. Dhinakaran, S. R. Naqvi, S. R. Gollu, R. Ahuja, and T. Hussain, Nanotechnology **29**, 355401, (2018)
- VI. **Enriching the hydrogen storage capacity of carbon nanotube doped with polylithiated molecules**
P. Panigrahi, S. R. Naqvi, M. Hankel, R. Ahuja, and T. Hussain, Appl. Surf. Sci. **444**, 467, (2018)

- VII. Exploring two-dimensional M_2NS_2 ($M= Ti, V$) MXenes based sensors for air pollutants**
S. R. Naqvi, V. Shukla, N. K. Jena, W. Luo, and R. Ahuja, Appl. Mater. Today, **19**, 100574, (2020)
- VIII. Superior sensitivity of metal functionalized boron carbide (BC_3) monolayer towards carbonaceous pollutants**
S. R. Naqvi, T. Hussain, S. R. Gollu, W. Luo, and R. Ahuja, Appl. Surf. Sci. **512**, 145637 (2020)
- IX. Computational insights into the hydrogen storage characteristics of Li and Na decorated 2D Boron Phosphide**
N. Khossossi, Y. Benhouria, S. R. Naqvi, P. K. Panda, Y. K. Mishra, I. Essaoudi, A. Ainane, and R. Ahuja
Manuscript

Reprints were made with permission from the respective publishers.

Comments on my own contribution

All the work in the paper I to IX was performed in close collaboration with the coauthors. The papers where I appear as the First author, I was responsible for performing the computations using the VASP code, analyzing the data, preparing the figures and writing the paper. In paper V and VI, I partly analyzed the data, prepared the figures and contributed to writing the papers. In paper IX, I designed the project, helped with VASP based computations, and contributed to writing the paper.

List of papers not included in the thesis

The following papers were produced during the time frame of this thesis, but are not included in the thesis.

- I. **Modelling high-performing batteries with MXenes: The case of S-functionalized two-dimensional Nitride MXene Electrode**
V. Shukla, N. K. Jena, S. R. Naqvi, W. Luo, and R. Ahuja. Nano Energy **58**, 877, (2019)

- II. **Energy loss of slow Ne ions in Pt and Ag from TOF-MEIS and Monte-Carlo simulations**
S. R. Naqvi, G. Possnert, and D. Primetzhofer, Nucl. Instrum. Methods Phys. Res., Sect. B, **371**, 76, (2016)

- III. **Metallized nitrogenated holey graphene nanosheets (C₂N): A promising material for high capacity clean energy storage**
S. R. Naqvi, T. Hussain, A. Karton, W. Luo, and R. Ahuja
Manuscript

Contents

Part I: Introduction and Theoretical Background	11
1 Introduction	13
1.1 Outline of the Thesis	18
2 Theoretical Background	19
2.1 The Many-Body Problem	19
2.2 Density Functional Theory (DFT) Formalism	23
2.2.1 Hohenberg-Kohn (HK) Theorems	24
2.2.2 The Kohn-Sham Ansatz	25
2.3 Exchange-Correlation Functionals	27
2.3.1 Local Density Approximations (LDA)	28
2.3.2 Generalized Gradient Approximations (GGA)	28
2.4 Van der Waals Interactions	29
2.5 Computational Methods	31
2.5.1 Basis Sets	31
2.5.2 Periodicity in Solids and Bloch's Theorem	32
2.5.3 Projector Augmented Wave Method	33
2.5.4 Force Theorem	35
2.5.5 Molecular Dynamics	36
Part II: Summary of the Results	37
3 Solid-State Materials for Hydrogen Storage	39
3.1 Hydrogen Storage via Chemisorption	40
3.2 Hydrogen Storage via Physisorption	41
3.2.1 Challenges of Hydrogen Physisorption	42
3.3 Strategies for Efficient Non-dissociative Hydrogen Storage	43
3.3.1 H ₂ Adsorption on Metallized Structures	44
3.3.2 Molecular Functionalization for Enhanced H ₂ Capture	52
4 Two-dimensional (2D) Structures for Gas Sensing Applications	58
4.1 Basic Mechanism of Gas Sensing	59
4.2 Gas Sensors Based on 2D Nanostructures	60
4.2.1 MXene Sheets	61
4.2.2 Metal Functionalized BC ₃ Sheets	65

5	Tuning the Structure and Electronic Properties of 2D Materials	68
5.1	Doping Characteristics of Stanene Monolayer.....	68
5.1.1	Adsorption Energies and Diffusion Pathways.....	69
5.1.2	Structural Deformations.....	72
5.1.3	Electronic Structure and Charge Analysis.....	73
	Part III: Final Remarks.....	75
6	Summary and Outlook.....	77
7	Svensk Sammanfattning	80
8	Acknowledgements	82
	References.....	84

Part I:
Introduction and Theoretical Background

1 Introduction

Since the beginning of life on the planet, mankind has been using science and technology to find the ease, luxuries, and comforts for living. For instance, advanced means of transportation are utilized on the ground, inside the water, and in the air. Heating and cooling systems are used for temperature adjustment inside the residential areas, and the offices. Advanced revolutionary materials are designed and used for information handling, entertainment, and global networking. In short, the endeavoring efforts and intelligence of human beings led this world to the point where life of an average man is much more comfortable than it could ever be imagined. Besides all the progress and accomplishments, however, our planet is much more vulnerable to natural calamities and disasters due to irreversible and devastating climate changes. According to a recent report of the World Bank [1], if the climate changes continue at the same pace then the parts of various coastal megacities would be under water near the year 2030. Additionally, an ever-growing trend in forest fires is expected due to the increase in the earth's temperature [2]. The major stimulus behind the unprecedented climate catastrophe is the *Energy crisis*.

Energy is a prerequisite for living and sustainable energy harvesting is the biggest technological challenge of the current times. Additionally, it is essential for uninterrupted scientific and technological development. Thanks to their high abundance in the earth's crust and the high energy-efficiency, fossil fuels were employed to meet the never-ending demands of energy for a very long time. However, relentless consumption of fossil fuels gave birth to potential environmental concerns. For instance, a drastic amount of CO_2 is emitted to the atmosphere which is the major culprit behind the global climate crisis. On the other hand, the available fossil reserves are gradually depleting and demands of energy are growing with time, which is responsible for a rapid rise in fuel prices. As reported, the demands of energy between the year 2009 and 2035 are expected to grow from 12 to 18 billion tons of oil equivalent [1–3]. Due to the higher demands of energy consumption and the continuous depletion of the fossil reserves, coal is expected to be the only available fossil reserve in the earth's crust after the year 2042 [4]. It is the need of the hour to find alternative means of energy production which are reversible, sustainable, cost-effective and environment friendly. In this regard, the energy from photovoltaics, solar, windmill, nuclear, biomass, and geothermal sources are being produced and utilized for industrial and domestic applications [5–7].

Meanwhile, Li-ion batteries earned huge scientific interest due to the high energy density, storage efficiency, and versatility of applications ranging from small scale electronic devices to vehicles and large-scale energy systems [8].

However, by virtue of its abundance in nature and high energy content, hydrogen (H_2) is so far an ideal carrier of sustainable energy [9, 10]. H_2 has unique characteristics surpassing all the other energy carriers, for instance, its high energy density, renewability, and a clean reaction in the fuel cell where water is emitted as the only by-product [11]. The comparison of the H_2 output energy content with the gasoline yields that 1kg of H_2 produces 143 MJ of energy which is equivalent to the heat content produced by combustion of 3 Kg of gasoline [12]. Similarly, the efficiency of the H_2 fuel cells is reported to be superior to Li-ion batteries in the transport sector [13–15]. Particularly for the vehicles with a range of more than 100 miles, H_2 fuel cells are reported to offer better energy efficiency, smaller refueling time and a higher environmental friendliness [16]. Besides automobiles, fuel cells are used in aircrafts, ships, forklifts, trains, as well as for stationary applications [17]. However, the fuel cell technology is under development and efficient means of H_2 production and storage for fuel cell applications are scarce as yet.

Although H_2 is the major constituent of the universe, still very small amounts of gaseous H_2 (5×10^{-5} mole fraction) exist in the earth's atmosphere [18]. This is partly due to the highly reactive nature of H_2 which allows it to form bonds with other elements. For example, H_2 is found in the form of water or it reacts with carbon, nitrogen, and oxygen to form the fossil fuels or biomass. Here it is important to state that H_2 itself is not a primary fuel, however, it becomes an energy carrier when energy is used to split the H_2 from other elements [19]. For H_2 production, steam reforming of natural gas and the coal gasification were previously employed, however, emission of CO and CO_2 as by-products makes these processes environmentally unsafe [19]. Recently, electrolysis of water using the energy obtained from solar or wind resources, and the thermochemical processes are considered as efficient, environmentally benign and reliable technologies for H_2 production [19–22].

An ideal H_2 fuel cell is expected to replace the fossil fuel dependence of the whole world while eliminating the environmental issues; the vision is called the *Hydrogen Economy*. The hydrogen economy works on a sustainable cycle, which starts from the production of H_2 from the electrolysis of water with the help of renewable energy, such as, solar or wind. H_2 is stored and later used in a fuel cell where H_2 reacts with O_2 and releases water as a by-product. The produced energy is used for transportation, industrial or domestic usages and finally the released water again becomes available for H_2 production. In this sustainable cycle, H_2O acts as a carrier of H_2 and H_2 acts as a carrier of energy. The concept of H_2 - H_2O sustainable cycle is illustrated in Figure 1.1.

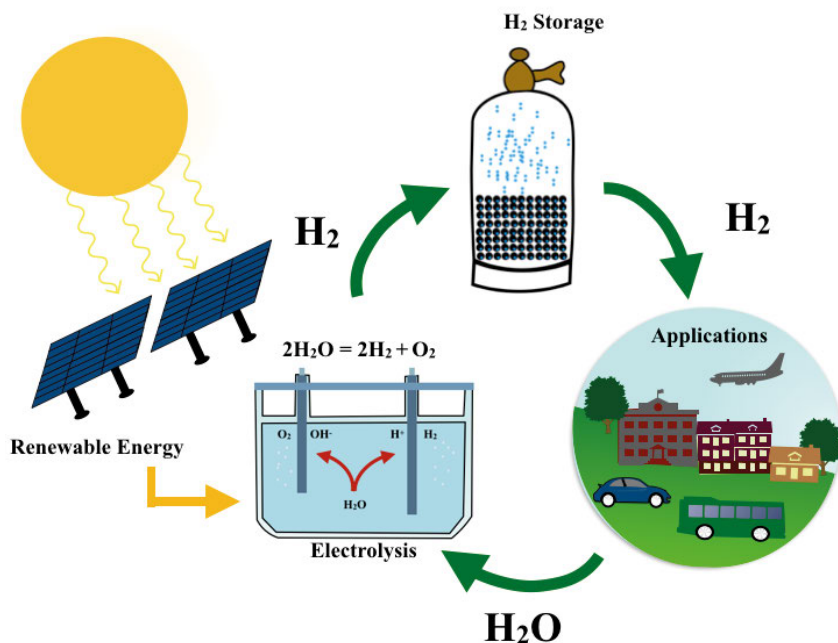


Figure 1.1. The perception of the hydrogen economy as a sustainable H_2 - H_2O cycle.

The major obstacle in the H_2 economy is to store H_2 under ambient conditions for onboard applications. This is the first main topic of this thesis and details are contained in Chapter 3. Here, a brief introduction of the H_2 storage problem, conventional strategies and new developments along with their pros and cons are discussed.

The challenge of H_2 storage arises from the fact that H_2 has a very low volumetric density $\sim 0.09 \text{ Kg/m}^3$ at ambient conditions (at 25°C or 298 K , and 100 kPa or 1 Bar). For instance, 1 Kg of H_2 occupies a volume roughly equivalent to 12 m^3 . Thus, the energy produced from H_2 contained in 1 m^3 of the volume is only 0.1 MJ , whereas, the equivalent volume of gasoline produces 34.2 MJ [12]. To utilize the potential of H_2 as a fuel, either it must be mechanically transformed to a state which is easier to handle for fuel cell applications, e.g., liquefied and compressed states, or it should be trapped inside the materials making chemical bonds or interacting via van der Waals forces. For practical implications, H_2 storage technique should be able to meet the following criteria: (1) high storage capacity, (2) low system-weight, (3) safety of operation, (4) cost-effectiveness, (5) environmental friendliness, (6) operability under ambient conditions and (7) reversibility.

The strategy of mechanical storage is conventionally employed to increase the volumetric capacity, however, transforming H_2 to a liquid or a compressed state is the unviable and a tedious approach which poses several practical con-

cerns, such as, volume, weight, and safety issues. The compression, for example, needs very high pressure up to ~ 700 bar to compress the gas with a gravimetric capacity of 5.2 wt% [23]. Another important issue is the fabrication of the storage tank because the compression tank is required to be lightweight, low cost, and durable to withstand the possible embrittlement during the operation. Several materials are designed and utilized for this purpose, however, the durability of the material, high cost, and the risk of explosion in case of a car crash are potential concerns which call for the improved design and manufacturing technologies [24–26]. On the other hand, the liquefaction, also called cryogenic cooling, requires energy for cooling down to ~ 20 K, moreover, a large amount of energy is required for maintaining the liquid phase. This is a very expensive process that requires almost 35% of the fuel energy content for liquefaction. Additionally, there is a loss of H_2 by evaporation and boil-off processes which are typically caused due to the heat adsorption during operation on vehicles, during refueling, and delivery procedures [27]. Another mechanical H_2 storage technique which was practically employed in Toyota Prius cars, named as cryocompression, exhibited better performance than other mechanical H_2 storage methods [28]. This technique uses the combination of compression and cryogenic H_2 storage techniques and fulfills the standard of the Department of Energy (DOE) for gravimetric capacity, however, the cost of a prototype system for H_2 storage and the cost of the fuel is much higher than the DOE criteria [29].

The second approach for H_2 storage, which is based on trapping H_2 inside the solid-state materials, via chemical bonding or physical adsorption mechanisms, seems the promising and viable choice to fulfill the H_2 storage criteria. During the chemical adsorption process, H_2 bond dissociates and each H atom forms chemical bonds with the host material typically with the adsorption strength of ~ 2 -3 eV [26, 30, 31]. A large number of H atoms can be stored in the form of metal hydrides, however, the total weight of the system turns out to be very high which limits the gravimetric and volumetric capacities. Some prominent metal hydride systems are $LiAlH_4$, $LiNH_2$, Li_2NH , $LiBH_4$, $NaAlH_4$, $KAlH_4$, MgH_2 , and $LaNi_5H_6$ [32–37]. Conversely, non-metal hydrides, such as boron and nitrogen hydrides, captured wide interest due to their lighter weight and higher gravimetric capacity. However, slower kinetics during the H_2 release is another practical hindrance which limits the applications of most of the chemical hydride based systems [38–40]. Additionally, the onboard refueling for chemical hydride materials is not possible, which limits the applicability to only those situations where onboard refueling is not preferred, such as, jets, rockets, and non-rechargeable batteries.

The physisorption or non-dissociative H_2 adsorption via van der Waals interaction, on the other hand, offers advantages of reversibility, and faster kinetics. Due to the high surface-to-volume ratio, low dimensional nanostructures are capable to adsorb a large quantity of H_2 , fulfilling the criterion of gravimetric capacity described by the DOE. The light weight of the material

further ensures the convenience of operation for portable applications. Examples of H_2 adsorption materials include carbonaceous structures, such as graphene, carbon nanotubes, and non-carbon materials including metal-organic frameworks (MOFs) and clathrates [27, 41–45]. The difficulty with non-dissociative materials-based H_2 storage arises due to the weaker (~ 0.1 eV) adsorption energies of the H_2 with the host material which are not sufficient for H_2 adsorption at ambient conditions [30, 31]. Based on the literature, H_2 storage via adsorption could be a prospective storage technique for the H_2 economy, however, it is required to tune the adsorption energies employing external species or surface modifications in the host material [41–45]. Chapter 3 of the thesis comprises the discussion and important outcomes of our work for H_2 storage on low dimensional structures.

Designing efficient materials for H_2 storage paves the way for clean energy and ensures the sustainability of the environment. However, monitoring and capturing of the suspended pollutants in the air is another important issue. A large amount of hazardous gases that can severely affect human health are emitted in the atmosphere due to industrial, natural, and biogenic processes. Moreover, the greenhouse effect is one of the several reasons which calls for efficient gas sensing and capturing of the gases. Among others, carbon-containing gases, such as carbon monoxide (CO), carbon dioxide (CO_2) and methane (CH_4) are directly or indirectly causing the greenhouse effect. For instance, CO is extremely hazardous as it can severely damage the human heart and the brain, causing sudden death. Similarly, ammonia (NH_3), nitric oxide (NO), nitrogen dioxide (NO_2), hydrogen sulfide (H_2S) and sulfur dioxide (SO_2) have adverse effects on the climate and the human health. Therefore, it is inevitable to monitor the leakage of these gases in the atmosphere to avoid serious health hazards. Semiconducting metal oxides and conducting polymers were previously employed for this purpose. Metal oxide-based sensors offer good sensitivity and low cost, but the operability is limited to higher operating temperatures and large power consumption, moreover, the selectivity of gases in these sensors is compromised [46, 47]. Contrarily, conducting polymers offer room temperature applicability and easy processing but suffer from humidity and degradation which limit their efficiency [48, 49]. Carbon nanotubes (CNTs) exhibit superior sensing performance with high selectivity of gases, however, long recovery times and processing difficulties hinder the performance of CNTs as a gas sensor [48]. Therefore, it is important to design materials that can efficiently sense pollutant molecules with high selectivity and less signal-to-noise ratio. In Chapter 4 of the thesis, the role of two-dimensional structures for efficient gas sensing is discussed along with important outcomes of our research. Meanwhile, understanding the structure and electronic properties of 2D structures can pave ways for their nanoscale device applications. In this regard, the effects of adatoms on structural and electronic properties of stanene monolayer are investigated and the results are briefly summarized in Chapter 5.

1.1 Outline of the Thesis

We used Density Functional Theory (DFT) to design the nanomaterials for H_2 storage and gas sensing applications. In this regard, the H_2 storage on functionalized boron carbide (BC_3), boron nitride (BN), siligraphene (SiC_7), carbon nanotubes (CNTs) and graphdiyne (GDY) nanostructures were studied. Similarly, metal-functionalized BC_3 sheets and S-functionalized M_2N MXene sheets were investigated for sensing and capturing of toxic gases. Also, the adsorption of different adatoms on two-dimensional stanene sheets was investigated. The Chapter 1, *Introduction*, is a brief description of the essence and motivation of this work, a summary of the previously made development in the field, major challenges and, the helpful strategies to tackle the challenges are introduced. Most importantly, it is described how the present work is going to contribute towards the field of energy harvesting and gas sensing. The Chapter 2, *Theoretical Background*, is dedicated to density functional theory. In the first part of this chapter, the many-body problem in physics is introduced and the essence of a DFT based computational approach is described. The development of DFT along with the associated formalism for solving the multi-electron systems are further described in the preceding sections of the chapter. In the second part, the computational methods for efficiently employing the DFT are explained in detail. In Chapter 3, entitled *Solid-State Materials for Hydrogen Storage*, different strategies for H_2 storage in solid-state materials are explained. Moreover, some of the important findings of this thesis work on the subject of H_2 storage are presented in this chapter. The Chapter 4 of the thesis, *2D Structures for Gas Sensing Applications*, covers the applications of 2D materials for sensing of air pollutants. In this perspective, types of pollutants, the mechanism of gas sensing, and sensing performance of investigated 2D structures are discussed. The Chapter 5, *Tuning the Structure and Electronic Properties of 2D Materials*, constitutes the effects of adatom adsorption on two-dimensional sheets. Particularly, the important outcomes of the adatom adsorption on stanene sheets are discussed. The Summary and outlook of the thesis are presented in Chapter 6. The summary of the thesis in Swedish, *Svensk Sammanfattning*, is provided in Chapter 7. Further details of the work, complete methodology, and the detailed discussions are present in the original papers which are attached at the end of this thesis.

2 Theoretical Background

Density functional theory (DFT) is the powerful computational approach to efficiently solve the puzzles of chemistry, physics, material sciences, and multiple disciplines of engineering. With widespread development spanned over more than 50 years, DFT is one of the most cost-effective, reliable and valuable tools for predicting the geometry, electronic structure, and a broad spectrum of compelling material properties. DFT is inevitable for the progressive engineering of materials, as the in-depth knowledge and understanding of the complicated scientific problems can't be achieved solely based on the experiments. Since all the computations in this thesis are performed using DFT, therefore, this section of the thesis is dedicated to describing the background and theoretical formalism of DFT.

2.1 The Many-Body Problem

The basic properties of materials depend on their fundamental constituents, i.e. the electrons and the nuclei. If one can thoroughly predict the nature of interactions between electrons in the matter then a widespread knowledge of the material properties can be extracted, such as electronic, electrical, optical, and magnetic behaviors. To understand the underlying physics of the materials, we need to solve the systems with plenty of atoms dressed up with many electrons, typically known as *Many-body problem* [50]. Quantum physics represents the many-body problem in the form of a many-body equation, named as Schrödinger equation. Time-independent non-relativistic Schrödinger equation can be written as under

$$H\Psi(\mathbf{r}_1, \mathbf{r}_2, \dots, \mathbf{r}_n, \mathbf{R}_1, \mathbf{R}_2, \dots, \mathbf{R}_N) = E\Psi(\mathbf{r}_1, \mathbf{r}_2, \dots, \mathbf{r}_n, \mathbf{R}_1, \mathbf{R}_2, \dots, \mathbf{R}_N) \quad (2.1)$$

Here, $\Psi(\mathbf{r}_1, \mathbf{r}_2, \dots, \mathbf{r}_n, \mathbf{R}_1, \mathbf{R}_2, \dots, \mathbf{R}_N)$ represents a wavefunction for the system of n electron and N nuclei whose positions are described by \mathbf{r}_i and \mathbf{R}_i , respectively. All the information that can be attained about the system at some particular state is contained in Ψ . Here, the Hamiltonian operator H acts on Ψ and yields the energy eigenvalue E . The complete form of Hamiltonian can be expressed as,

$$H = -\frac{\hbar^2}{2m_e} \sum_i \nabla_i^2 - \frac{\hbar^2}{2} \sum_I \frac{\nabla_I^2}{M_I} + \frac{1}{2} \sum_{i \neq j} \frac{e^2}{|\mathbf{r}_i - \mathbf{r}_j|} + \frac{1}{2} \sum_{I \neq J} \frac{Z_I Z_J e^2}{|\mathbf{R}_I - \mathbf{R}_J|} - \sum_{i,I} \frac{Z_I e^2}{|\mathbf{r}_i - \mathbf{R}_I|} \quad (2.2)$$

Here, in atomic units \mathbf{r}_i , m_e and e denote the electronic spatial coordinates, mass, and charge of i^{th} electron, respectively. Similarly \mathbf{R}_I , M_I and, Z are the respective nuclear components for the I^{th} nucleus and the term $\hbar = h/2\pi$ represents the reduced Plank's constant. The kinetic energy of the electrons and the nuclei is computed by using the first two terms in eq. (2.2), respectively. The remaining three terms compute the potential energy due to the Coulomb forces between the electron-electron, the nucleus-nucleus, and the electron-nucleus pairs, respectively. Eq. (2.2) yields an exact solution for the small systems, for example, a particle in a box and atoms with a single electron (H, He^+ , Li^{2+}). For a multiple-electron system, the *Born-Oppenheimer approximation* (BOA) is employed to simplify the Hamiltonian [51]. BOA splits the wavefunction into electronic and nuclear components based on the assumption that there is a huge mass difference between an electron and the nucleus. As the electrons are much lighter compared to the nuclei ($1836 \times m_e \cong M_I$), therefore the speed of electrons is much higher compared to the nuclei ($v_e \gg v_I$). For this reason, the nuclei can be imagined as frozen particles in the sea of high-speed electrons. Thus one can consider that electrons are moving on a potential energy surface provided by the nuclei. Due to this approximation, the nuclear kinetic energy term enters in the Eq. (2.2) only as the potential (V_{ext}) externally supplied to the electrons. The wavefunction can thus be rewritten as follows

$$\Psi(\mathbf{r}_1, \mathbf{r}_2, \dots, \mathbf{r}_n, \mathbf{R}_1, \mathbf{R}_2, \dots, \mathbf{R}_N) = \Psi_e(\mathbf{r}_1, \mathbf{r}_2, \dots, \mathbf{r}_n) \Psi_N(\mathbf{R}_1, \mathbf{R}_2, \dots, \mathbf{R}_N) \quad (2.3)$$

The Hamiltonian transforms according to BOA [52], as under

$$H = -\frac{\hbar^2}{2m_e} \sum_i \nabla_i^2 + \frac{1}{2} \sum_{i \neq j} \frac{e^2}{|\mathbf{r}_i - \mathbf{r}_j|} - \sum_{i,I} \frac{Z_I e^2}{|\mathbf{r}_i - \mathbf{R}_I|} \quad (2.4)$$

Thus a purely electronic Hamiltonian is written, where the kinetic energy of the nuclei vanishes and the nuclear contribution acts as a constant (V_{ext}). The use of BOA reduces the complexity of the problem, however, the exact wavefunction for a many-body system is still not easy to find due to the electronic correlations. The motion of electron 1 in a N-electron system and its interaction with the frozen nuclei are affected by the Coulomb forces provided by N-1 electrons. Thus, the electronic correlation further adds to the complexity of the problem, therefore, eq. (2.4) lacks to provide a complete analytical solution for the multiple-electron systems. To simplify the situation, the concept of independent-electrons was introduced in the form of *Hartree and Hartree-*

Fock formalism which is based on the assumption that the electrons are non-interacting (i.e., $V_{ee} = 0$). Under these theories, the Hamiltonian is separable and the problem of correlated N electrons can be transformed into a N single-electron problem. Thus, the Hamiltonian for a system of N non-interacting particles is defined as under,

$$H = \sum_{i=1}^N h(i) \quad (2.5)$$

Here $h(i)$ is the operator that gives the kinetic energy and the potential energy of the electron i . Eigenfunction of the H operator is a wavefunction which is a product of spin-orbital wavefunctions $\chi(\mathbf{x})$, as under,

$$\psi^{HP}(\mathbf{x}_1, \mathbf{x}_2, \dots, \mathbf{x}_N) = \chi_i(\mathbf{x}_1) \chi_j(\mathbf{x}_2) \dots \chi_k(\mathbf{x}_N) \quad (2.6)$$

Here, ψ^{HP} denotes the *Hartree Product*. The Hamiltonian operator H acts on ψ^{HP} which yields $H\psi^{HP} = E\psi^{HP}$. The energy is defined as the sum of spin-orbital energies ($E = \epsilon_i + \epsilon_j + \dots + \epsilon_k$). The Hartree product defined as Eq. (2.6) has a serious shortcoming that it does not obey Pauli's exclusion principle and electrons are distinguishable. For instance, the probability of finding electrons 1 to N in a volume element could be expressed by the following relationship,

$$|\psi^{HP}(\mathbf{x}_1, \mathbf{x}_2, \dots, \mathbf{x}_N)|^2 d\mathbf{x}_1 \dots d\mathbf{x}_N = |\chi_i(\mathbf{x}_1)|^2 d\mathbf{x}_1 |\chi_j(\mathbf{x}_2)|^2 d\mathbf{x}_2 \dots |\chi_k(\mathbf{x}_N)|^2 d\mathbf{x}_N \quad (2.7)$$

Here, the simultaneous probability of finding electron 1 in $d\mathbf{x}_1$ and electron 2 in $d\mathbf{x}_2$ is equal to the product of probabilities. According to this formalism, electron 1 is completely independent of other electrons. This is not true for the case of electrons with parallel spins. If we have a system of two electrons with parallel spins, then the probability of finding both electrons at position \mathbf{r}_1 is zero i.e., $P(\mathbf{r}_1, \mathbf{r}_1) = 0$. However, electrons with opposite spins are always uncorrelated and independent of each other. Hartree Product (ψ^{HP}) for electrons 1 and 2 can be written as follows

$$\psi_{12}^{HP}(\mathbf{x}_1, \mathbf{x}_2) = \chi_i(\mathbf{x}_1) \chi_j(\mathbf{x}_2) \quad (2.8)$$

$$\psi_{21}^{HP}(\mathbf{x}_1, \mathbf{x}_2) = \chi_i(\mathbf{x}_2) \chi_j(\mathbf{x}_1) \quad (2.9)$$

A wavefunction which obeys anti-symmetry could be obtained as an appropriate linear combination of the above two Hartree Products.

$$\psi(\mathbf{x}_1, \mathbf{x}_2) = 2^{-1/2} (\chi_i(\mathbf{x}_1) \chi_j(\mathbf{x}_2) - \chi_j(\mathbf{x}_1) \chi_i(\mathbf{x}_2)) \quad (2.10)$$

This anti-symmetrized wavefunction was named as *Hartree-Fock (HF)* wavefunction. HF wavefunction could be generalized in the form of a determinant, called Slater determinant named after John Slater. For two electrons Slater determinant form of the HF wavefunction is written as below,

$$\psi(\mathbf{x}_1, \mathbf{x}_2) = 2^{-1/2} \begin{vmatrix} \chi_i(\mathbf{x}_1) & \chi_j(\mathbf{x}_1) \\ \chi_i(\mathbf{x}_2) & \chi_j(\mathbf{x}_2) \end{vmatrix} \quad (2.11)$$

It is easy to see that if two electrons are introduced in a similar orbital (i.e., $\chi_i = \chi_j$), then $\Psi(\mathbf{x}_1, \mathbf{x}_2)$ goes to zero which is another way to justify *Pauli exclusion principle*. Electrons are indistinguishable and therefore belong to every orbital. For N electrons, the Slater determinant is written as under,

$$\psi(\mathbf{x}_1, \mathbf{x}_2, \dots, \mathbf{x}_N) = (N!)^{-1/2} \begin{vmatrix} \chi_i(\mathbf{x}_1) & \cdots & \chi_k(\mathbf{x}_1) \\ \vdots & \ddots & \vdots \\ \chi_i(\mathbf{x}_N) & \cdots & \chi_k(\mathbf{x}_N) \end{vmatrix} \quad (2.12)$$

The Slater determinant is symbolically represented as $|\psi_1, \psi_1, \dots, \psi_1\rangle$ and provides the solution of the Schrödinger equation. HF theory is based on the approximation that each particle feels an average field due to the presence of surrounding charged particles, named as *Mean-field approximation*. HF solution gives the accurate ground state energy by using a single Slater determinant (N-electron) to approximate a ground state wavefunction of N electrons. Within single Slater determinant, motion of electrons with parallel spins are correlated whereas electrons with antiparallel spins are uncorrelated. In order to obtain the ground state energy according to HF theory, the Slater determinant is minimized $E_{HF} = \min_{\psi_{SD \rightarrow N}} E[\psi_{SD}]$ with the help of variational theorem. This is a *Self-Consistency Field (SCF)* method which begins with a random guess of a set of atomic orbitals. Those sets of orbitals are used to find the energy and subsequently the new orbitals. The process continues until the convergence is achieved. The wavefunction for the N electrons is defined in terms of four variables, i.e. three position coordinates and one spin coordinate. The exponential scaling of the HF method with $4N$ leads to a great deal of computational challenges. However, HF formalism was a great breakthrough which simplified the many-body problem and laid down the foundations of the most advanced electronic structure methods and density functional theory (DFT) is one of them.

The problem of $4N$ variables could be simplified by replacing the wavefunction with the electron density which is a 3 variable function. Due to the complex nature of the electronic interactions, the exact solution of the Schrodinger equation is scarce as yet, however, the complexity of the problem is minimized with the help of density functional theory (DFT). This thesis is based on the computations performed by the Vienna Ab-initio Simulation

Package (VASP) which is a DFT based code. In the subsequent sections, the development of the DFT formalism and the computational methods are explained in the detail.

2.2 Density Functional Theory (DFT) Formalism

As mentioned in the previous section, HF theory was based on a reasonable approach for computing the accurate ground state energy of the many-body system. However, the biggest challenge was to determine the complicated many-body wavefunction. If one could replace a wavefunction based approach with a much simpler electron density based formalism then the computational difficulties could be handled without sacrificing the quality of results. Hence, DFT formalism was born as a reliable and cost-effective solution to the many-body problem.

Before digging deep into the DFT theory, it is worthwhile to understand the importance of using the density of electrons $\rho(\mathbf{r})$ instead of the wavefunction. The first reason is that $\rho(\mathbf{r})$ is a mathematical parameter that is possible to measure. This observable entity makes it possible to get a mapping of the system which is relatively closer to reality. The integral of $\rho(\mathbf{r})$ over the volume element gives the total number of electrons N contained in that specific volume as follows,

$$\int \rho(\mathbf{r}) d\mathbf{r} = N \quad (2.13)$$

The nuclear charges can be computed by the information of $\rho(\mathbf{r})$ around the nuclei. As the nuclear attractive forces tend to keep the electrons together and the density $\rho(\mathbf{r})$ is maximum close to the nuclei, \mathbf{R}_i . The gradient of density undergoes discontinuity around this region and cusps are formed. Thomas and Fermi were the first to use the concept of $\rho(\mathbf{r})$ as a variable to determine the total energy of the system [52, 53]. However, due to the absence of exchange and correlation parts in the Thomas-fermi theory, one could not apply this formalism to solve the many-body problem. The consideration of simplified non-interacting uniform electron gas for computing the kinetic energy of electrons was not realistic. Moreover, the electron-electron Coulomb repulsion and electron-nuclei attractive potentials were classically treated. This simplified approach for computing the kinetic energy of electrons was inefficient, since the exchange and correlation parts were completely missing. The accurate depiction of the many-body system was lacking even after the inclusion of exchange energy suggested by Dirac [54]. The present-day DFT is standing on the pillars of some fundamental theories which were first introduced by Hohenberg and Kohn [55].

2.2.1 Hohenberg-Kohn (HK) Theorems

Hohenberg and Kohn provided the solution of an interacting many-body system using $\rho(\mathbf{r})$ in their sensational work which laid down the foundations of contemporary DFT. The theory was presented in the form of two landmark theorems¹:

Theorem I:

For any system of interacting particles in an external potential $V_{ext}(\mathbf{r})$, the potential $V_{ext}(\mathbf{r})$ can be determined uniquely, except for a constant, by the ground state particle density $\rho_0(\mathbf{r})$.

Theorem II:

A universal functional for the energy $E[\rho]$ in terms of density $\rho(\mathbf{r})$ can be defined, valid for any external potential $V_{ext}(\mathbf{r})$. For any particular $V_{ext}(\mathbf{r})$, the exact ground state energy of the system is the global minimum value of this functional, and the density $\rho(\mathbf{r})$ that minimizes the functional is the exact ground state density $\rho_0(\mathbf{r})$.

The first HK theorem suggests that the density of electrons at the ground state $\rho_0(\mathbf{r})$ is sufficient to unveil the properties of a system of interacting particles, whereas, $V_{ext}(\mathbf{r})$ is just included as a constant. More explicitly, the ground state density is sufficient to determine the exact form of the many-body Hamiltonian. Further, the functional of electron density can be utilized to determine all the observable entities of the system as

$$\langle \psi | A | \psi \rangle = A[\rho(\mathbf{r})] \quad (2.14)$$

The second theorem reveals how to determine the exact ground state density $\rho_0(\mathbf{r})$. The electron density at the ground state can be determined by finding the minimum value of the energy functional $E[\rho]$. The density corresponding to that minimum $E_0[\rho]$ is the ground state density $\rho_0(\mathbf{r})$. Based on these theorems, the functional of total energy can be expressed in terms of electron density as

$$E_{HK}[\rho(\mathbf{r})] = F_{HK}[\rho(\mathbf{r})] + \int d\mathbf{r} V_{ext}(\mathbf{r})\rho(\mathbf{r}) \quad (2.15)$$

¹The statements of the HK theorems are quoted from the book entitled “Electronic structure: Basic Theory and Practical Methods” by Richard. M. Martin [50].

Here, $F_{HK}[\rho(\mathbf{r})]$ is the universal functional which contains the total internal energies of the system of interacting particles as below,

$$F_{HK}[\rho(\mathbf{r})] = T[\rho(\mathbf{r})] + J[\rho(\mathbf{r})] + E_{ncl}[\rho(\mathbf{r})] \quad (2.16)$$

Where the first two terms in Eq. (2.16) represent the kinetic energy of electrons and the potential energy due to classical Coulomb interaction, respectively. The third term accounts for the non-classical contributions to the total energy, i.e. self-interaction, correlation, and exchange effects. By accurately predicting the universal functional $F_{HK}[\rho(r)]$, one can successfully obtain the exact energy of the system at the ground state. Similarly, the ground state density can be obtained by minimizing the energy functional, $E[\rho(r)]$. Due to the non-classical contributions to the energy of the correlated system, only the second term in the above equation could be accurately computed. Thus, the ambiguity of computationally solving a complicated interacting system of particles remained unresolved as the exact form of the first and third terms in Eq. (2.16) is unknown.

2.2.2 The Kohn-Sham Ansatz

In the outclass work of Hohenberg and Kohn, the solution of a many-body problem is provided in terms of a universal functional, however, the exact solution of the ground state density is not provided. The Kohn-Sham (KS) formalism shows a simplified approach for the realization of the exact form of the ground state density. It is based on the idea that a system of interacting particles can be replaced with a relatively simpler reference system of non-interacting particles having the exact same density of electrons such that the applicability of the HK theorems is still validated [56]. The kinetic energy of the real system T can be mapped to the exact kinetic energy of auxiliary systems T_S because of the density constraint. The expression for the kinetic energy of the uncorrelated system T_S in terms of Kohn-Sham orbitals takes the form as,

$$T_S = -\frac{\hbar^2}{2m_e} \sum_{i=1}^N \langle \xi_i | \nabla_i^2 | \xi_i \rangle \quad (2.17)$$

The kinetic energies of the real and auxiliary system are related as under

$$T = T_S + T_C \quad (2.18)$$

Here T_C accounts for the residual forces in the kinetic energy of correlated electrons. The Eq. (2.16) can be modified as

$$F[\rho(\mathbf{r})] = T_S[\rho(\mathbf{r})] + J[\rho(\mathbf{r})] + T_C[\rho(\mathbf{r})] + E_{ncl}[\rho(\mathbf{r})] \quad (2.19)$$

$$= T_S[\rho(\mathbf{r})] + J[\rho(\mathbf{r})] + E_{XC}[\rho(\mathbf{r})] \quad (2.20)$$

Here, the residual contribution of the total kinetic energy and non-classically treated electrostatic potential are grouped in the form of E_{XC} , which is named as *the exchange and correlation energy*. The functional of total energy in Eq. (2.15) can be redefined as

$$E[\rho(\mathbf{r})] = T_S[\rho(\mathbf{r})] + \frac{1}{2} \iint \frac{\rho(\mathbf{r}_1)\rho(\mathbf{r}_2)}{|\mathbf{r}_1 - \mathbf{r}_2|} d\mathbf{r}_1 d\mathbf{r}_2 + \int d\mathbf{r} V_{ext}(\mathbf{r})\rho(\mathbf{r}) + E_{XC}[\rho(\mathbf{r})] \quad (2.21)$$

The above Eq. (2.21) contains the terms for the kinetic energy of the auxiliary non-interacting system, the classical Coulomb potential between the electrons, the external potential acting on electrons due to the presence of nuclei, and exchange-correlation energies, respectively. Combining the findings of KS formalism with the second theorem of HK provides the solution of the auxiliary KS system in the form of a Schrodinger-like single-particle KS equation as

$$H_{KS}(\mathbf{r})\xi_i(\mathbf{r}) = \left[-\frac{\hbar^2}{2m_e} \nabla^2 + V_{KS}(\mathbf{r}) \right] \xi_i(\mathbf{r}) = \varepsilon_i \xi_i(\mathbf{r}) \quad (2.22)$$

Here, $\xi_i(\mathbf{r})$, $V_{KS}(\mathbf{r})$ and, ε_i denote the i th KS orbital, the KS effective potential, and eigenvalues of the H_{KS} operator, respectively. The effective potential $V_{KS}(\mathbf{r})$ can be explicitly written in the form

$$V_{KS}(\mathbf{r}) = V_{ext}(\mathbf{r}) + V_H(\mathbf{r}) + V_{XC}(\mathbf{r}) \quad (2.23)$$

Here, second term $V_H(\mathbf{r})$ symbolizes the Hartree potential which is determined as

$$V_H(\mathbf{r}) = \int \frac{\rho(\mathbf{r}_2)}{|\mathbf{r}_1 - \mathbf{r}_2|} d\mathbf{r}_2 \quad (2.24)$$

The last term in Eq. (2.23) represents the exchange and correlation potential which is not defined in the exact form, however, it can be defined as a derivative of the exchange-correlation energy functional $E_{XC}[\rho(\mathbf{r})]$ with respect to the density $\rho(\mathbf{r})$.

$$V_{XC} = \frac{\delta E_{XC}[\rho(\mathbf{r})]}{\delta \rho(\mathbf{r})} \quad (2.25)$$

Finally, the expression for the ground state density can be written as

$$\rho(\mathbf{r}) = \sum_{i=1}^N |\xi_i(\mathbf{r})|^2 \quad (2.26)$$

The effective potential $V_{KS}(\mathbf{r})$ can be obtained according to Eq. (2.23) by inserting $V_H(\mathbf{r})$ and V_{XC} parameters. If the exact form of V_{XC} is known, the exact density and consequently the energy of the system at the ground-state can be computed by applying the self-consistent field (SCF) approach. This iterative method searches for the KS orbitals according to KS formalism and provides the solution of the KS equation, Eq. (2.22). The KS formalism provides the exact solution of the many-body system by mapping the real interacting system to the auxiliary non-interacting system having the same density. However, the exact form of the exchange and correlation potential (V_{XC}) is still unknown and a research problem in itself, therefore the approximations are used for accurate determination of these parts of the energy.

2.3 Exchange-Correlation Functionals

In the KS formalism, the discrepancies between the real system of correlated particles and an auxiliary system of uncorrelated particles are merged under a single term, known as exchange and correlation functional [56]. The exact solution for this term is only known for a uniform electron gas (UEG). UEG is defined as an ensemble of interacting particles (electrons) spread over an infinite region with a uniform density ρ_0 , neutralized by a uniform background density ρ_+ . A sensible approach for obtaining the exchange and correlation potential of an infinite ensemble is to determine the energy density per each particle (ε_{XC}) [57]. By separating the exchange and correlation parts of the energy density, one may conveniently write as,

$$\varepsilon_{XC}^{UEG}(\rho) = \varepsilon_X^{UEG}(\rho) + \varepsilon_C^{UEG}(\rho) \quad (2.27)$$

Exchange energy density can be analytically solved with the help of the following expression as [50, 54]

$$\varepsilon_X^{UEG}(\rho) = -\frac{3}{4}e^2 \left(\frac{6}{\pi}\rho_0\right)^{\frac{1}{3}} \quad (2.28)$$

The correlation energy density can be analytically obtained for low and high-density regimes. The interpolation between these regimes is obtained with the help of Monte-Carlo algorithm combined with some other interpolation techniques [50, 57, 58]. The functional $E_{XC}[\rho]$ for a real system of non-uniformly distributed particles can thus be approximated with the help of exchange ε_X and correlation ε_C energy densities.

2.3.1 Local Density Approximations (LDA)

Local Density Approximation (LDA) locally treats the exchange and correlation parts of the potential based on a UEG model, such that the density at each position \mathbf{r} is constant, $\rho(\mathbf{r}) = \rho_0$. As described earlier, the exchange term ε_X^{UEG} is analytically obtained with the help of Eq. (2.28). Similarly, a mapping between the regions of high and low electronic densities with the help of Monte-Carlo simulations depicts the correlation term ε_C^{UEG} . Typically, the accuracy of the LDA approximation depends on the use of interpolation schemes. By combining ε_X^{UEG} and ε_C^{UEG} terms, the exchange-correlation functional within LDA framework can be written as follows [58],

$$E_{XC}^{LDA}[\rho(\mathbf{r})] = \int \varepsilon_{XC}^{UEG}(\rho) \rho(\mathbf{r}) d\mathbf{r} = \int ([\varepsilon_X^{UEG}(\rho) + \varepsilon_C^{UEG}(\rho)]) \rho(\mathbf{r}) d\mathbf{r} \quad (2.29)$$

LDA is a simple approximation that is expected to work well only for the systems with slowly varying charge densities, such as those which nearly resemble a UEG, for example, metals with free and valence electrons. However, the error cancellation in the exchange and correlation terms produces reliable results for a vast variety of systems including insulators and semiconductors [59].

Besides several advantages, there are a few major shortcomings associated with LDA functionals. For instance, larger computational discrepancies are noted for the systems with highly inhomogeneous charge densities, such as isolated atoms and molecules. Moreover, overestimated binding energies and cohesive energies, and underestimated bond lengths and bandgaps are reported. Similarly, electron localization according to LDA is well-suited for the systems with s and p electrons, however, inaccurate results are produced for the systems containing d and f electrons. Van der Waals and hydrogen bonding are poorly depicted with the help of this approximation. Few examples of LDA functionals are Perdew-Zunger (PZ81) [60], Perdew-Wang-92 (PW92) [61] and Vosko-Wilk-Nusair (VWN) [62].

2.3.2 Generalized Gradient Approximations (GGA)

The shortcomings of the LDA could be improved to a great extent with the help of generalized gradient approximation (GGA). GGA is based on the assumption that $\varepsilon_{XC}^{UEG}[\rho(\mathbf{r})]$ is not only a function of electronic density but also the gradient of electronic density at each position \mathbf{r} . For the systems with inhomogeneous electronic density, the gradient of density ($\nabla\rho$) is locally obtained for exchange and correlation parts. Based on this idea, the exchange-correlation functional [50] could be written as

$$E_{XC}^{GGA}[\rho(\mathbf{r})] = \int \varepsilon_{XC}[\rho(\mathbf{r}), \nabla\rho(\mathbf{r})] \rho(\mathbf{r}) d\mathbf{r}$$

$$= \int \varepsilon_X^{UEG}(\rho) F_{XC}[\rho(\mathbf{r}), \nabla\rho(\mathbf{r})] \rho(\mathbf{r}) d\mathbf{r} \quad (2.30)$$

Here, ε_X^{UEG} is the energy density of a UEG for exchange contribution. $F_{XC}(\rho, \nabla\rho)$ is the enhancement parameter of GGA which depends on a dimensionless quantity, the density gradient, s , defined as

$$s = \frac{|\nabla\rho|}{2k_f\rho} \quad (2.31)$$

The enhancement parameter, F_{XC} , considers the degree of deviation from UEG character. Several forms of F_{XC} were proposed in the past, however, most commonly known are provided by Becke (B88) [63], and Perdew, Burke and Ernzerhof (PBE) [64].

Most of the computational work in this thesis is based on PBE approximation which works fairly well for predicting the physical and chemical properties of materials. GGA functionals are generally known to overcome most of the limitations of LDA, for example, accurate description of the chemical energy in metals and semiconductors as well as hydrogen bonding in materials [61, 65–67]. However, there are certain cases where the accuracy of GGA functionals is compromised, for example, the systems where van der Waals forces are dominant [68]. Similarly, GGA functionals are inaccurate for the materials with strong correlation effects or the systems where self-interaction error is non-negligible [50, 69, 70].

2.4 Van der Waals Interactions

The long-range forces termed as *Van der Waals (vdW) forces* typically originate from three different modes of interactions between the dipoles, for instance, the forces between two permanent dipoles, one permanent and another induced dipole, or a pair of induced dipoles (known as London dispersion force). The dipole-dipole forces sometimes play a dominant role in the formation of materials, for example, in the organic molecules. The intermolecular binding of those structures is inaccurately predicted with LDA and GGA functionals because of the missing non-local correlation effects in these functionals.

In this section, the origin, the significance and the treatment of London dispersion interaction in conjunction with DFT formalism is described. London-dispersion forces are long-range attractive forces that are related to the distance as R^{-6} , where R indicates the distance between the corresponding group of molecules or atoms [71–74]. The exchange and correlation functionals that are local or semi-local, do not incorporate the non-local effects. The inability

of LDA and GGA functionals to predict the dispersion interactions encourages the development of alternative methods that are cost-effective and accurate.

A useful approach for computing the correct total energy is to compute the total pairwise potential between the molecules and include it in the DFT energy (based on Kohn-Sham formalism). This method of adding the intermolecular potentials to account for dispersion interactions was employed by Grimme [75–77], Tkatchenko and Scheffler (TS) [78], and Becke and Johnson (BJ) [79]. For the computations in this thesis, we employed vdW corrections of Grimme known as DFT-D2 and DFT-D3 to compute the accurate adsorption energies of the atoms and molecules on various nanostructures. In these methods, the total energy is written as the sum of KS energy and dispersion energy (E_{dis}) as

$$E_{DFT-D} = E_{KS} + E_{dis} \quad (2.32)$$

E_{KS} is obtained utilizing a self-consistent approach based on Kohn-Sham formalism. The term E_{disp} is the empirically corrected pairwise potential, defined as follows

$$E_{disp} = -s_6 \sum_{i=1}^{N_a-1} \sum_{j=i+1}^{N_a} \frac{C_6^{ij}}{R_{ij}^6} f_{damp}(R_{ij}) \quad (2.33)$$

Here, s_6 is a global scaling parameter and C_6^{ij} is a coefficient of dispersion for the $\langle ij \rangle$ atomic pair. The dispersion coefficient is obtained by computing a geometric mean of the terms C_6^i and C_6^j . The distance between the i th and j th atom is indicated as R_{ij} and N_a account for the total number of atoms that are responsible for dispersion forces. The damping factor f_{damp} in Eq. (2.33) accounts for the long-range nature of the dispersion interactions. f_{damp} is expressed as follows

$$f_{damp}(R_{ij}) = \frac{1}{1 + e^{-d(R_{ij}/R_r-1)}} \quad (2.34)$$

Here, d is the adjustable entity and $R_r = R_i + R_j$ is the total vdW radius obtained as a sum of the individual vdW radii of the i th and j th atom. This approach is very much time effective as compared to the self-consistent field procedure. However, the only problem is the non-flexible nature of C_6 parameter which does not consider the local chemical behaviors of the concerning species. This issue is eliminated in the DFT-D3 formalism, where the dispersion coefficient can be adjusted with respect to the liganacy of the concerning species.

2.5 Computational Methods

2.5.1 Basis Sets

The development of DFT theory along with efficient exchange and correlation functionals provides adequate foundations for the quantum computations. However, for the practical implication as a computational tool, one needs to find ways to conveniently compute the KS wavefunctions, ξ_i , and eigenvalues, ε_i , for an infinitely large number of interacting electrons influenced by the static potential provided by a huge number of nuclei. To simplify the computations, the KS wavefunction, ξ_i , can be expanded in the form of basis set, φ_γ , and the coefficients, $C_{i\gamma}$, as follows

$$\xi_i = \sum_{\gamma=1}^N C_{i\gamma} \varphi_\gamma \quad (2.35)$$

Here N corresponds to the number of each basis for the particular orbital. Eq. (2.35) is the mathematical expansion of ξ_i which can be inserted in the KS equations to reduce the problem to the form of a generalized matrix as follows

$$\left[-\frac{\hbar^2}{2m_e} \nabla^2 + V_{KS}(\mathbf{r}) \right] \sum_{\gamma=1}^N C_{i\gamma} \varphi_\gamma = \varepsilon_i \sum_{\gamma=1}^N C_{i\gamma} \varphi_\gamma \quad (2.36)$$

The equation can be multiplied with the conjugate basis function, φ^* , and integrated over the corresponding volume element as follows

$$\sum_{\gamma=1}^N C_{i\gamma} \int_V \varphi^* \mathfrak{h}_{KS} \varphi_\gamma d\mathbf{r} = \varepsilon_i \sum_{\gamma=1}^N C_{i\gamma} \int_V \varphi^* \varphi_\gamma d\mathbf{r} \quad (2.37)$$

here \mathfrak{h}_{KS} is given as,

$$\mathfrak{h}_{KS} = \left[-\frac{\hbar^2}{2m_e} \nabla^2 + V_{KS}(\mathbf{r}) \right] \quad (2.38)$$

The integral on the left-hand side in Eq. (2.37) is the KS Hamiltonian for a single particle which is symbolically represented as \mathbf{H}^{KS} . Similarly, integral on the right-hand side represents the overlap matrix, \mathbf{S} . Therefore, Eq. (2.37) can be symbolically expressed as

$$\mathbf{H}^{KS} \mathbf{C} = \mathbf{S} \mathbf{C} \quad (2.39)$$

Thus, the introduction of coefficients matrix, $C_{i\gamma}$, and eigenvalue matrix, ε_i , in the KS equations lead to the form of a generalized matrix which consists of KS Hamiltonian, \mathbf{H}^{KS} , and overlap matrix, \mathbf{S} . The solution of Eq. (2.39) is obtained by matrix diagonalization. Basis sets being the mathematical entities are written in various ways, however, *Plane Waves (PW)* offer several advantages for the systems where periodic boundary conditions are satisfied. In

this thesis work, PW basis sets are used for the treatment of periodic solid structures and molecules.

2.5.2 Periodicity in Solids and Bloch's Theorem

As stated in the previous section, the periodicity in solids is advantageous to further reduce the complexity of the many-electron problem. According to Bloch's theorem [80], the properties of the infinite number of electrons can be extracted by investigating only a finite number of electrons contained in a unit cell. The nature of the effective potential provided by the nuclei is periodic which further substantiates the application of periodic boundary conditions. Thus, KS orbitals can be written in the form of Bloch's periodic wavefunctions as under

$$\xi_{jk}(\mathbf{r}) = e^{i\mathbf{k} \cdot \mathbf{r}} u_{jk}(\mathbf{r}) \quad (2.40)$$

Here $u_{jk}(\mathbf{r})$ is a function that defines the periodicity of the crystal structure. Here, j stands for band index and \mathbf{k} is the wavevector which corresponds to the first Brillouin zone. The term, $u_{jk}(\mathbf{r})$, in Eq. (2.40) can be expanded by using the Fourier series as below

$$u_{jk}(\mathbf{r}) = \sum_{\mathbf{G}} \frac{1}{\sqrt{\Omega}} c_{jk}(\mathbf{G}) e^{i\mathbf{G} \cdot \mathbf{r}} \quad (2.41)$$

Here, Ω and c_{jk} indicate the volume of a primitive cell and the coefficients of expansion in the PW basis set, respectively. \mathbf{G} represents the lattice vector in the reciprocal space, thus, $\mathbf{G} \cdot \mathbf{r} = 2\pi m$, where \mathbf{r} is a vector in the real space and m is the integer value. Thus, the KS orbitals in the form of PW basis set can be expressed as

$$\xi_{jk}(\mathbf{r}) = \sum_{\mathbf{G}} c_{jk}(\mathbf{G}) \times \frac{1}{\sqrt{\Omega}} e^{i(\mathbf{k} + \mathbf{G}) \cdot \mathbf{r}} \quad (2.42)$$

KS equation is solved by setting a cutoff radius, \mathbf{k}_{max} , for the reciprocal lattice which is the upper limit for the choice of Bloch's wavevector. This employs that the values $\mathbf{k} > \mathbf{k}_{max}$ are not allowed. Similarly, KS orbitals are expanded as a linear combination of PW basis sets under periodic boundary conditions. Thus, by employing the plane-wave basis set and periodicity in the crystal lattice, the band structure is resolved by diagonalizing the Eq. (2.39) which generates the eigenvalues $\epsilon_j(\mathbf{k})$ and eigenfunctions, ξ_{jk} .

2.5.3 Projector Augmented Wave Method

The computations in this thesis are employed using the VASP software which is based on the Projector-augmented wave (PAW) method. The PAW approach is based on the assumption that a many-body system is comprised of two types of regions. The non-overlapping spherical domains around the ions form the augmented region while the remaining parts of the system form the interstitial region, therefore, wavefunctions can also be separately treated for both the regions. The inside and outside of the augmented spherical domains are treated with partial and envelop wavefunctions, respectively [81]. The wavefunctions must coincide outside the augmented sphere and preserve continuity at the boundaries of the augmented spheres. Typically, plenty of oscillating wavefunctions are available around the core, therefore, computing a real wavefunction (ψ) for all-electrons could be tedious. A computationally efficient way is to map the all-electrons single atom wavefunction with the auxiliary or pseudo wavefunction ($\tilde{\psi}$) which is expressed in terms of the fewer basis sets. This pseudo wavefunction appears as an eigenfunction in the KS equation for a single atom.

Considering that the volume of the augmented sphere is Ω_R , the pseudo wavefunction inside the volume, Ω_R , can be formed by linear mixing of the partial-wave basis, the same procedure is followed for writing the all-electrons wavefunction. Hence,

$$\begin{aligned} |\psi(\mathbf{r})\rangle &= \sum_i c_i |\phi_i(\mathbf{r})\rangle && \text{inside } \Omega_R \\ |\tilde{\psi}(\mathbf{r})\rangle &= \sum_i d_i |\tilde{\phi}_i(\mathbf{r})\rangle && \text{outside } \Omega_R \end{aligned} \quad (2.43)$$

Here, c_i , d_i are the coefficients of expansion and i is the index for angular momentum (l, m) at a position \mathbf{R} . Outside the augmented sphere, i.e. beyond a critical radius (r_c), partial and all-electron waves are matching

$$|\phi_i(\mathbf{r})\rangle = |\tilde{\phi}_i(\mathbf{r})\rangle \quad \text{outside } \Omega_R \quad (2.44)$$

The partial wavefunctions for all-electrons and the pseudo part are connected with the help of an operator, τ , as given below

$$|\psi\rangle = \tau |\tilde{\psi}\rangle \quad (2.45)$$

Here,

$$\tau = \hat{\mathbf{1}} + \sum_R S_R \quad (2.46)$$

The operator τ provides a linear transformation pathway to connect the true all-electron wavefunction to the pseudo wavefunction. As given in Eq. (2.46), τ is based on the identity operator $\hat{\mathbf{1}}$ and the atomic contribution parameter, S_R , at a position \mathbf{R} . S_R accounts for the differences between the all-electron and pseudo partial waves. Thus,

$$S_R|\tilde{\phi}_i\rangle = |\phi_i\rangle - |\tilde{\phi}_i\rangle \quad (2.47)$$

The projector operator $|\tilde{P}_i\rangle$, which fulfills the conditions (i) $|\tilde{\phi}_i\rangle\langle\tilde{P}_j| = \delta_{ij}$ for $i, j \in R$ and, (ii) $\sum_i |\tilde{\phi}_i\rangle\langle\tilde{P}_i| = 1$, can be used to connect the interstitial and augmented regions. Thus, the new form of the auxiliary wavefunction is as follows

$$|\tilde{\psi}\rangle = \sum_i |\tilde{\phi}_i\rangle\langle\tilde{P}_i|\tilde{\psi}\rangle \quad (2.48)$$

Combining Eq. (2.45) to Eq. (2.48), the wavefunction for all-electrons can be written as below

$$|\psi\rangle = |\tilde{\psi}\rangle + \sum_i (|\phi_i\rangle - |\tilde{\phi}_i\rangle)\langle\tilde{P}_i|\tilde{\psi}\rangle \quad (2.49)$$

$$= |\tilde{\psi}\rangle + \sum_R (|\psi_R^1\rangle - |\tilde{\psi}_R^1\rangle) \quad (2.50)$$

here,

$$|\psi_R^1\rangle = \sum_{i \in R} |\phi_i\rangle\langle\tilde{P}_i|\tilde{\psi}\rangle \quad (2.51)$$

$$|\tilde{\psi}_R^1\rangle = \sum_{i \in R} |\tilde{\phi}_i\rangle\langle\tilde{P}_i|\tilde{\psi}\rangle \quad (2.52)$$

The equations (2.51) and (2.52) represent the true all-electrons and auxiliary wavefunctions, respectively. Outside the spherical volume Ω_R , these wavefunctions are equal i.e., $|\psi_R^1\rangle = |\tilde{\psi}_R^1\rangle$. However, inside the augmented sphere, $|\psi\rangle = |\tilde{\psi}_R^1\rangle$. Based on these facts, we can rewrite the Eq. (2.49) as follows

$$|\psi\rangle = (\hat{1} + \sum_i (|\phi_i\rangle - |\tilde{\phi}_i\rangle)\langle\tilde{P}_i|) |\tilde{\psi}\rangle \quad (2.53)$$

By comparing Eq. (2.45) and (2.53), the transformation operator (τ) can be written as

$$\tau = \hat{1} + \sum_i (|\phi_i\rangle - |\tilde{\phi}_i\rangle)\langle\tilde{P}_i| \quad (2.54)$$

Using the operator τ , the new form of the KS equation is given as under

$$(\tilde{H} - \varepsilon\tilde{O}) |\tilde{\psi}\rangle = 0 \quad (2.55)$$

Also, $\tilde{H} = \tau^\dagger H \tau$ and $\tilde{O} = \tau^\dagger \tau$, where \tilde{H} represents the pseudo-Hamiltonian. Hence, PAW ansatz simplifies the computations by expressing the all-electron Hamiltonian to a pseudo-Hamiltonian which is solved with the help of fewer plane waves.

2.5.4 Force Theorem

The minimum energy state of a system can be depicted based on the fact that the total forces acting on a system are zero at the equilibrium state. In other words, non-zero residual forces reckon the non-equilibrium state of the corresponding group of atoms. In computational quantum physics, the ground state of a system is achieved by minimizing the forces on atoms in a process called geometry optimization. Considering, \mathbf{F}_N symbolizes the total force acting on the Nth nucleus at a position, \mathbf{R}_N , then \mathbf{F}_N can be written as

$$\mathbf{F}_N = -\frac{\partial E}{\partial \mathbf{R}_N} \quad (2.56)$$

Here, E is the total energy which can be expressed as

$$E = \frac{\langle \psi | H | \psi \rangle}{\langle \psi | \psi \rangle} \quad (2.57)$$

Considering that the KS orbitals ψ are normalized, i.e. $\langle \psi | \psi \rangle = 1$ and substituting Eq. (2.56) in Eq. (2.57), \mathbf{F}_N can be expressed as

$$\mathbf{F}_N = -\left\langle \psi \left| \frac{\partial H}{\partial \mathbf{R}_N} \right| \psi \right\rangle - \left\langle \frac{\partial \psi}{\partial \mathbf{R}_N} \left| H \right| \psi \right\rangle - \left\langle \psi \left| H \right| \frac{\partial \psi}{\partial \mathbf{R}_N} \right\rangle \quad (2.58)$$

Using $H|\psi\rangle = E|\psi\rangle$ and $\langle \psi | \psi \rangle = 1$, \mathbf{F}_N simplifies to the following expression

$$\begin{aligned} \mathbf{F}_N &= -\left\langle \psi \left| \frac{\partial H}{\partial \mathbf{R}_N} \right| \psi \right\rangle - E \left(\frac{\partial \langle \psi | \psi \rangle}{\partial \mathbf{R}_N} \right) \\ &= -\left\langle \psi \left| \frac{\partial H}{\partial \mathbf{R}_N} \right| \psi \right\rangle \end{aligned} \quad (2.59)$$

The Eq. (2.59) is known as the *Hellman-Feynman Force theorem* which states that the energy derivative for any variable equals the expectation value of the derivative of Hamiltonian [50]. DFT based electronic structure calculations use force theorem to predict the equilibrium structure in a process which computes the residual forces acting on atoms and moves the atoms in a way that the total forces can be minimized to zero (or typically to an acceptable force criterion of $\sim 10^{-2}$ eV/Å).

2.5.5 Molecular Dynamics

Molecular dynamic (MD) simulations are widely used in the sciences for predicting the dynamic evolution of the system under consideration. The movements of the atoms and molecules are studied at a particular temperature for a specific interval of time. There are two different approaches for performing MD simulations, known as, classical molecular dynamics (CMD) and ab-initio molecular dynamics (AIMD). The basic difference lies in the strategy for computing forces on the atoms. The CMD approach uses Newtonian mechanics for predicting the forces using the following relationship

$$\mathbf{F}_i = m_i \mathbf{a}_i = m_i \ddot{\mathbf{r}}_i \quad (2.60)$$

Here, forces on atoms are predicted by generating the model potentials [82, 83]. This scheme is suitable and cost-effective for treating a large system where plenty of atoms and molecules are present. However, the accuracy of the computations is compromised because it does not account for the details such as charge transfer, bond formation, and bond dissociations, etc. On the other hand, AIMD computations are accurate but the treatment of a very large number of particles is not practical in terms of computational cost. The forces are computed in AIMD as follows

$$\mathbf{F}_i = -\nabla E_i = m_i \ddot{\mathbf{r}}_i \quad (2.61)$$

In this thesis, AIMD simulations based on the Born-Oppenheimer model are used for predicting the thermal stability of the structures for the application as hydrogen storage media at ambient conditions.

Part II:
Summary of the Results

3 Solid-State Materials for Hydrogen Storage

Hydrogen (H_2) being a versatile carrier of energy can offer a CO_2 -neutral solution for fulfilling the energy demands of the world. A large part of the total energy consumption of the world, 30.3%, is attributed to the transportation sector [84]. Based on this fact, the transport sector could be a potential market for H_2 but its storage for transport applications is also a huge challenge. Currently, the vehicles based on batteries, H_2 , and hybrid batteries/ H_2 are leading contestants of the transport industry. The combination of superior energy density and durability of the fuel cell in H_2 vehicles make them superior to battery vehicles. However, the H_2 industry suffers from the low density of H_2 gas which makes it difficult to stock an adequate amount of H_2 for onboard usage, for example, 5kg to roughly drive a distance of 500 miles [85]. US Department of Energy (DOE) has defined certain criteria for the H_2 storage system to be used in vehicles. According to those criteria, both gravimetric and volumetric capacity of H_2 are important factors to consider, which further implies that the total weight of the system and volume of the container should be reasonable for the range and size of the vehicle. Similarly, the recyclability of the storage system should not be less than 500 times and the charging times for the storage system should be short, most preferably 3-5 minutes [86, 87].

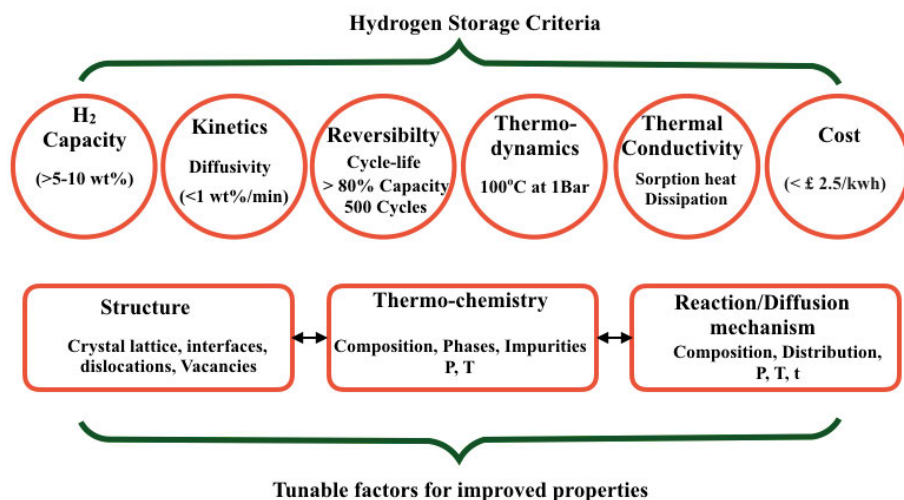


Figure 3.1. Practical limitations for onboard storage and the key factors to be improved.

The conventional ways of storing hydrogen under pressure and liquefaction face several limitations. For instance, compression (particularly at 700 bar) is an expensive process and a large amount of energy is expended during the gas storage. Besides that, special cylinders made of composite materials are required to withstand the pressure of 350 bar or 700 bar. Durability, weight, size, and shape of the cylinders cause potential concerns related to the safety of operation and practicality. For instance, gravimetric and volumetric capacities are affected by the aforementioned factors and the placement of cylinders inside the cars and smaller vehicles could be another problem. Similar kinds of packing challenges are offered by liquid hydrogen cylinders. Cryogenic storage or hydrogen liquefaction requires a temperature of 20 K which is crucial to maintain. The cost of the liquefaction is very high compared to the standard of DOE. The heat conductivity could also happen through walls of the cylinders or due to the higher surface area of the storage system, causing a boil-off which is extremely undesirable especially when a vehicle is parked in an enclosed area or garage for longer time period. The delivery tubes and internal walls of the storage tank need cooling as well because the loss of energy via hydrogen evaporation is quite probable. Due to these practical challenges and limitations, hydrogen storage via conventional compression and liquefaction techniques is not ideal for fuel cell vehicles. The unconventional approach, which is based on the capture of hydrogen inside the solid-state materials is preferred over conventional storage techniques due to the high gravimetric and volumetric capacities, cost-effectiveness, and safety of operation. There are two types of materials-based hydrogen storage techniques, namely chemisorption and physisorption, which will be discussed in the following sections.

3.1 Hydrogen Storage via Chemisorption

Hydrogen chemisorption typically means that H_2 bond dissociates and a reaction of H atoms with the host material occurs according to the following equation



Here M stands for the elements in the host material. H_2 molecule splits on the surface of the host and chemically reacts with other elements. Upon dissociation, H_2 can either bind to the surface or it can penetrate inside the bulk to occupy interstitial sites. Initially, a solid solution is formed due to the interstitial site occupation by H atoms but higher concentrations transform the structure to a new phase of a compound or a chemical hydride [88]. Being a very reactive element, hydrogen reacts with various elements resulting in the formation of compounds. These compounds are distinguishable from each other

depending on the type and nature of the elements and nature of the interaction between the hydrogen and the host. With light metals (such as alkali and alkaline earth metals), hydrogen forms ionic bond resulting in the formation of light metal hydrides or saline hydrides [89–92]. On the contrary, transition metal atoms and non-metals, form metallic/semiconducting, and covalent hydrides, respectively [93–96]. Similarly, complex hydrides are designed by a combination of hydrogen with the elements belonging to the group I-III of the periodic table, such as LiAlH_4 and LiBH_4 . For metal hydrides, a large weight of the system could lead to lower gravimetric densities. So far, achieving a reversible gravimetric capacity of 6 wt% along with cycling capability below 100°C (1bar) is a great challenge for metal alloys. Some light metal hydrides and complex hydrides are reported to exhibit high storage capacities but their thermodynamic conditions are not favorable for practical fuel cell conditions. Desorption of stored hydrogen requires increasing the temperature or reducing the pressure. The temperature/pressure requirements for adsorption and desorption processes act as the decisive parameters which entail the practicability of the storage media. Magnesium hydride is extensively investigated as a high capacity system for which the cycling temperature lower than 200°C (at 1Bar) could not be achieved [89, 97]. Aluminum hydrides, AlH_3 , is another example of a thoroughly investigated chemical storage system that offers high capacity but the process of hydrogenation requires very high pressure which is economically not viable [98]. Complex hydrides, such as, borohydrides offer high storage capacities but reversibility is again problematic. The reversibility of tetrahydridoborates of metals (e.g., magnesium and transition metals) leads to the emission of diborane gas which is poisonous for fuel cell, moreover, continuous degradation of the material in terms of storage capacity due to the boron deficiency is reported [99, 100]. Besides practical challenges, the research on chemical storage systems is bristling with new ideas and evolving with time, and the quest for ideal storage system has intensified. Designing the alternate and efficient means of hydrogen storage with favorable thermodynamics and economic viability is momentous. In this context, molecular adsorption on material surfaces is considered an ideal solution that can offer fast kinetics and cost-effectiveness.

3.2 Hydrogen Storage via Physisorption

The physically adsorbed H_2 retains its molecular state and interacts with the host materials via weak van der Waals forces. The adsorption energy of H_2 with host material is typically the order of ~ 0.1 eV. To match the DOE standard established in 2010 for H_2 gravimetric and volumetric capacities, a storage material should have a density around ~ 1 g/cm^3 which means that the material's weight should be comparable to that of water. Fortunately, physisorption

is supported on the materials with a high surface-to-volume ratio, which consequently leads to higher gravimetric capacities. In this context, extensive investigations on the carbon nanotube (CNT), graphene, graphane, metal-organic frameworks, nanoribbons, zeolites, BN sheets, and several other lightweight systems were performed and reported in the literature [101–110]. Another advantage is related to the reversibility which is again attributed to weaker adsorption energies of H_2 with the host material. The weaker interaction of H_2 with the substrate can suffice faster kinetics (adsorption/desorption), the character which is lacking in the chemical storage systems. The desorption of H_2 from the surface happens without distorting the structure of the host. A small amount of energy can simultaneously dehydrogenate the whole surface of the storage media in a very short time interval. Since the H_2 desorption is an endothermic process, the leakage of H_2 from the storage material does not cause any explosion. Due to these remarkable traits and the synthesis of novel materials with high surface-to-volume ratio, H_2 storage via physisorption has boomed for several years.

3.2.1 Challenges of Hydrogen Physisorption

Concerning the DOE criteria for H_2 storage, hydrogen physisorption technique suffers from some unavoidable challenges. Storage capacity is greatly affected by the weight of the storage media, therefore, only the lightweight or porous materials can be ideal for H_2 storage. The light weight and high surface area of graphene seem promising for H_2 physisorption, however, the full coverage of H_2 on both sides of graphene could result in a storage capacity of 5 wt% which is not sufficient according to DOE criteria [111]. The small gravimetric capacity, in this case, is related to the adsorption geometries and distances between H_2 molecules. Since adsorbed H_2 molecules tend to keep a van der Waals distance of ~ 0.3 nm between each other, therefore, only a limited number of molecules can be compensated on each side of the graphene sheet. To tackle the problem of storage capacity, the area of adsorbent surfaces must be comparable or greater than the area of graphene which is ~ 2600 m²/g [111]. Therefore, single-layered materials such as single-walled carbon nanotubes (CNTs), boron nitride (BN) sheets, and metal-organic frameworks (MOFs) are expected to yield higher storage capacities. MOFs showed great potential due to their high surface area (~ 3000 m²/g) and lightweight, as mostly these structures are porous and based on C atoms [105, 106, 112, 113]. The H_2 storage capacity of 6–8 wt% is reported for MOFs at around 77 K, however, the capacity drops to 1 wt% at 300 K. The drop in H_2 storage capacity is attributed to feeble van der Waals interactions between the H_2 and the adsorbent. H_2 adsorption at room temperature (300 K) can be achieved if the adsorption energy of H_2 is between 0.25–0.3 eV [111]. For smaller adsorption energies,

one needs to provide low temperature or higher pressure conditions. This situation makes it challenging to store H_2 via physisorption under room temperature and pressure constraints.

In this scenario, it is crucial to design new materials with lightweight and large surface area which are capable to bind H_2 with adequate adsorption strength. Introducing the topological defects or dopants on the surfaces, applying the electric field and functionalizing with foreign molecules could be suitable mechanisms for tuning the adsorption strength of H_2 molecules on the sheet. In the next sections, the strategies for improving the adsorption energy and storage capacity of storage media are discussed along with some important results obtained from our computations.

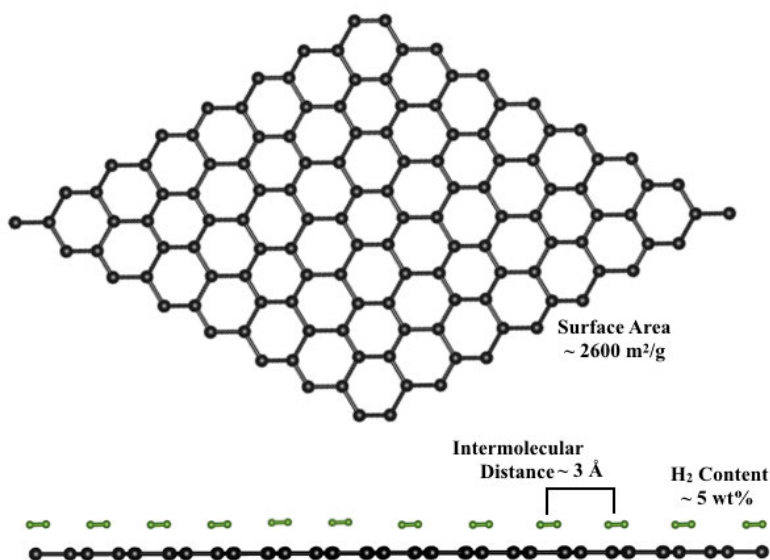


Figure 3.2. The storage capacity for fully hydrogenated graphene sheets with a surface area of $\sim 2600 \text{ m}^2/\text{g}$ is only 5 wt%.

3.3 Strategies for Efficient Non-dissociative Hydrogen Storage

In the following sections, some of the important results from our studies are summarized. For the details of the computational methodology and results, please refer to the attached papers.

3.3.1 H₂ Adsorption on Metallized Structures

3.3.1.1 Metal-doped Graphdiyne sheets

As discussed in the previous section, a high gravimetric capacity for H₂ storage can be achieved when the adsorbent material is made up of light elements, such as carbon (C), boron (B), nitrogen (N), etc. In this regard, carbon-based single-layered structures are very interesting particularly those with large pore sizes. One such example is graphdiyne (GDY) nanosheet, which is experimentally synthesized very stable diacetylene allotrope of carbon. The geometrical structure of GDY sheets is shown in Figure 3.3. The lattice structure consists of large pores in the form of benzene rings with both sp and sp² hybridization of carbon atoms. The bandgap opening for the experimentally synthesized GDY sheet is reported as 0.46 eV [114]. GDY sheets are reported to show high mobility of electrons which is comparable with graphene [114]. Furthermore, catalytic abilities of GDY sheets for CO oxidation in the presence of Ag₃₈ cluster and metal-free oxygen reduction are reported elsewhere [115], [116]. Due to the lightweight and large pore sizes, high H₂ uptake is possible on the surface of GDY sheets. However, tuning the adsorption energy of H₂ molecules to meet the room-temperature storage conditions is essential.

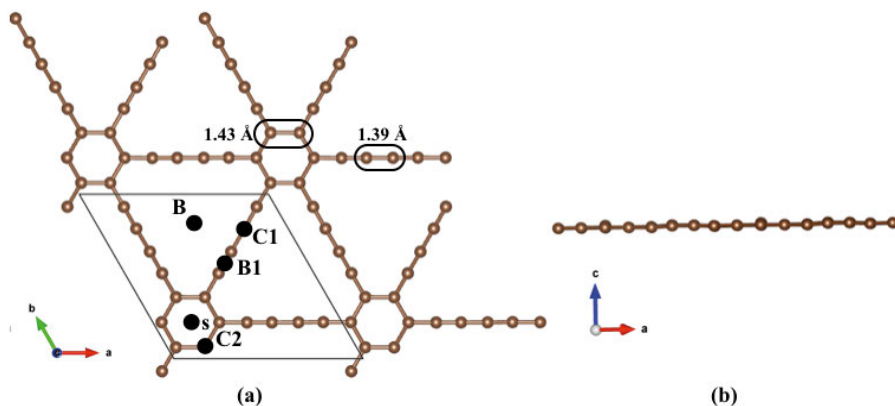


Figure 3.3. Top and side views of the planar GDY sheet. The unit cell enclosed by black lines consists of 18 atoms. Dotted (black) spots represent possible adsorption sites for adatoms. The C-C bond length for small and large pores are 1.43 and 1.39 Å, respectively.

We introduced light metal adatoms Li, Na, K, Ca, Sc and Ti on GDY sheets to capture the large number of H₂ molecules with improved binding strength. The top and side views of the unit cell of the GDY sheet having 18 atoms are shown in Figure 3.3. The structure consists of various binding sites for the adsorption of adatoms, for example, small pore (s) and large pore (B), C top in the large pore (C1), C top in the small pore (C2), and bridge site (B1), marked with black dotted spots in Figure 3.3. Adatoms were placed over all

the possible adsorption sites and the most stable site was the one with the strongest adsorption energy for the adatom. Initially, one adatom was allowed to adsorb on the sheet which prefers to bind at the large pore (B) site. Later, the interaction of the second atom was investigated in the presence of first adsorbed atom. The most favorable binding sites for all the metal adatoms was the hollow of the large pore (B). The adsorption energies, the distances between metal-sheet and metal-metal, and the bader charge per metal adatom are listed in Table 3.1.

Table 3.1. *The adsorption energies (eV), the average distances $D_{\text{Metal-C}}$ (between the metal adatom and the sheet) and $D_{\text{Metal-Metal}}$ (between the adatoms), and charges on adatoms are listed.*

Adatom	E_{ads} (1 atom) (eV)	E_{ads} (2 atoms) (eV)	$D_{\text{Metal-C}}$ (Å)	$D_{\text{Metal-Metal}}$ (Å)	Charge (e)
Li	-4.31	-2.28	2.21	4.76	+0.90
Na	-3.45	-2.00	2.81	5.46	+0.90
K	-4.30	-2.39	2.96	5.48	+0.90
Ca	-3.06	-3.23	1.41	3.78	+0.55
Sc	-5.19	-4.93	2.16	4.75	+2.04
Ti	-3.73	-5.23	2.09	4.88	+1.96

The adsorption energies for all the adatoms were strong enough to rule out the metal clustering, whereas, the adsorption energies of Sc and Ti were strongest amongst all the dopants. The adsorption energies were computed according to the following expression,

$$E_{\text{ads}} = E(DFT)_{\text{GDY}+M} - [E(DFT)_{\text{GDY}} + E(DFT)_M] \quad (3.1)$$

Here, $E(DFT)_{\text{GDY}+M}$, $E(DFT)_{\text{GDY}}$, and $E(DFT)_M$ are the total energies of the metallized GDY sheet, pristine GDY sheet, and the metal atoms, respectively. The total energy was computed using KS DFT along with GGA functional and van der Waals DFT-D3 correction. The electronic structure of the pristine and Li-, Sc-, and Ti-doped GDY sheets are plotted as the partial density of states (PDOS) in Figure 3.4. As compared to other metals, the strongest interactions of Sc and Ti atoms with the sheet were confirmed with the study of electronic structure. In Figure 3.4(c), the strong hybridization of Sc (3d) and Sc (4s) with C (p) states is noticeable near the Fermi level. Similarly overlapping Ti (3d) and Ti (4s) states with C (p) states near the Fermi level are visible in Figure 3.4(d). For further details of the electronic structure and charge transfer, readers are referred to Paper V.

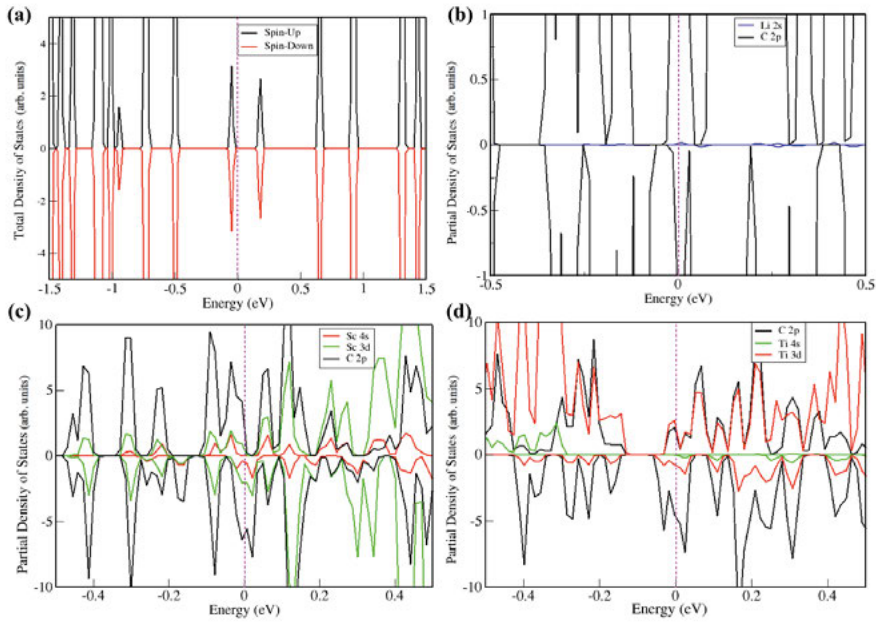


Figure 3.4. The electronic structure plotted as PDOS for (a) pure GDY sheet, (b) Li-(c) Sc-, and (d) Ti-doped GDY sheets. The metal doping turns the small bandgap semiconducting GDY sheets to metallic sheets. Reproduced with permission from Paper V. Copyright ©2018 IOP publishing Ltd.

The metallized structures were then exposed to H_2 molecules in different possible geometries. The number of H_2 molecules was gradually increased and gravimetric capacities for maximum hydrogenation cases were computed using the following formula,

$$H_2(G) = \frac{N_H \times W_H}{[(N_C \times W_C) + (N_M \times W_M) + (N_H \times W_H)]} \quad (3.2)$$

Here N and W represent the number and weight of atoms and M represents the metal atoms ($M = Li, Na, K, Ca, Sc,$ and Ti). Each metal atom could capture maximum of four H_2 molecules which yielded a high storage capacity of 6.50, 5.80, 5.20, 5.13, 5.0, and 4.91 wt% for Li, Na, K, Ca, Sc, and Ti-doped GDY sheets, respectively. The fully hydrogenated Li-doped GDY sheet which yielded the highest gravimetric capacity amongst all is shown in Figure 3.5. The binding/adsorption energies of H_2 molecules were computed using the expression,

$$E_{ads} = \frac{[E_{M-GDY-nH_2} - (E_{M-GDY} + nE_{H_2})]}{n} \quad (3.3)$$

Here, n , $E_{M-GDY-nH_2}$, E_{M-GDY} , and E_{H_2} represent the number of H_2 molecules and the total energies of hydrogenated metallized GDY sheet, metallized sheet and H_2 molecule, respectively.

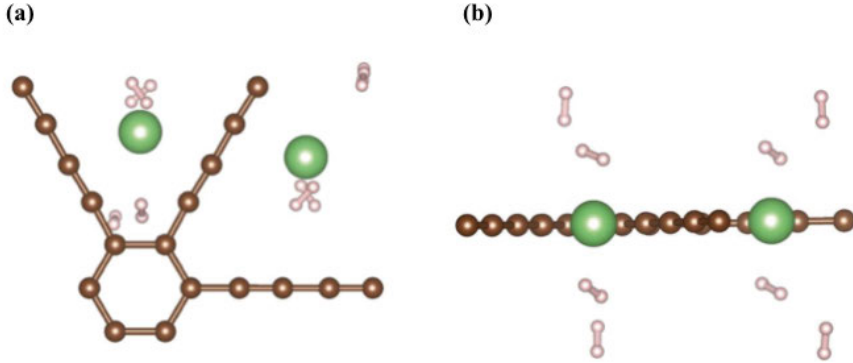


Figure 3.5. (a) Top and (b) side view of Li-doped hydrogenated GDY sheets. Each metal site could capture four H_2 molecules leading to a high gravimetric capacity of 6.5 wt%. Here, brown, green and pink colors correspond to C, Li, and H atoms.

Here it is important to mention that H_2 molecules interact with the GDY sheets via van der Waals forces which are challenging to accurately compute using DFT. The accurate computation of these forces requires the inclusion of exchange and correlation functionals. The unique feature of this paper is that three different functionals GGA, non-local vdW and DFT-D3 are used for the accurate computations of the adsorption energies of H_2 molecules on the functionalized sheets. Regardless of the computational approach, adsorption energies of H_2 are always adequate for room-temperature H_2 storage. The adsorption energies for 4, 6 and 8 H_2 molecules computed with three different functionals are plotted in Figure 3.6.

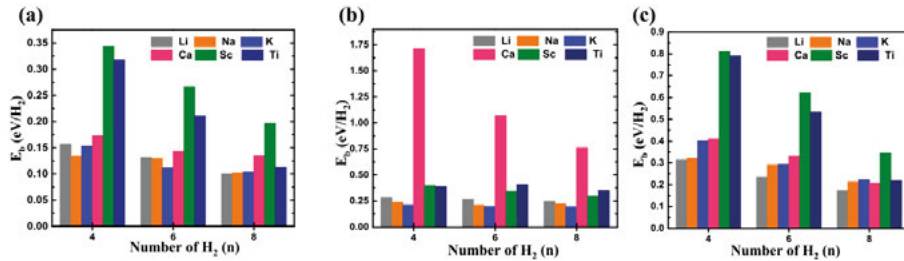


Figure 3.6. The average adsorption energies per H_2 in cases of 4, 6 and 8 H_2 on metal functionalized GDY sheets computed by (a) GGA, (b) vdW-DF, (c) DFT-D3. Reproduced with permission from Paper V. Copyright ©2018 IOP publishing Ltd.

3.3.1.2 Siligraphene (SiC_7) sheets with light metals

In Paper III, a honeycomb planar structure named siligraphene (SiC_7) was investigated for H_2 storage. As previously discussed, carbon-based structures are promising for H_2 storage applications particularly due to their light atomic weight, however, the binding of the H_2 molecules on several experimentally tested carbon nanostructures is weaker for practical storage conditions. As compared to CNTs, the adsorption energies of the H_2 molecules were reported to increase by 20% when adsorbed on silicon carbide nanotubes (SiCNTs), owing to the alternative charges located in the structure [117]. As reported, the electronic properties of silicon carbide ($\text{Si}_x\text{C}_{1-x}$) monolayers (with $0 < x < 1$) were greatly dependent on x , therefore varying the composition could result in outstanding and versatile characteristics [118]. The experimental synthesis of siligraphene (SiC_7) monolayers was considered a breakthrough discovery due to the outstanding mechanical, electronic, and optical characteristics [119]. Similar to carbonaceous nanostructures, the interaction between H_2 molecules and pure SiC_7 sheets were weak (< 0.1 eV), therefore, doping with light alkali (Li, Na, K), alkaline earth (Mg, Ca) and transition metal (Sc, Ti) adatoms was chosen as a route for improved H_2 adsorption. We performed electronic structure calculations using the GGA-PBE method which depicted that pure SiC_7 is a semiconductor with a bandgap of 0.70 eV, whereas the experimental bandgap of 1.13 eV is reported elsewhere [119]. It is important to mention that the GGA-PBE method usually underestimates the bandgap. The accurate bandgap could be computed with the help of computationally expensive hybrid functionals, however, it was beyond the purview of this particular study. The adsorption of metal adatoms yielded a significant effect on the electronic structures of SiC_7 sheets. The interaction between the electronic states of adatoms and semiconducting SiC_7 sheets tuned the structure from semiconducting to metallic. The optimized geometry and electronic structure of pure SiC_7 sheets is shown in Figure 3.7.

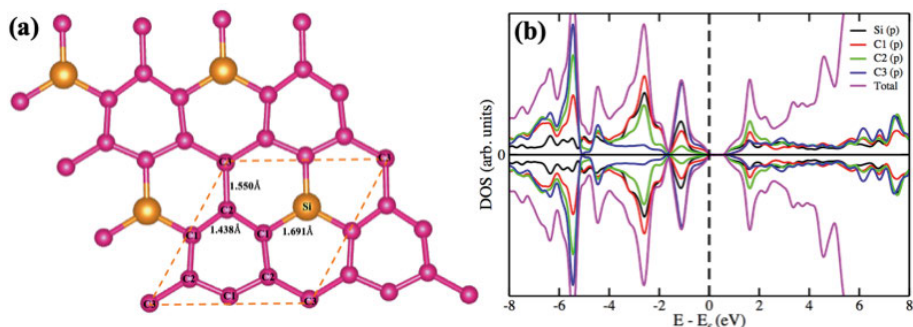


Figure 3.7. (a) The $(2 \times 2 \times 1)$ supercell of SiC_7 sheet consists of 28 C and 4 Si atoms. (b) The electronic structure of SiC_7 shows a small bandgap of 0.70 eV. Reproduced with permission from Paper III. Copyright © 2018, Springer Nature

The E_{ads} values of adatoms were computed in a similar approach as in Eq. (3.1). Among all the adatoms, Mg showed a tendency for cluster formation, as the E_{ads} for Mg was lower than the reported cohesive energy (E_c) [120]. Similarly, higher concentrations of Ti were prone to cluster formation, therefore H_2 storage was not investigated for those cases. We further tested the possibility of dimer formation on the SiC_7 sheets by investigating their adsorption behavior. The E_{ads} values of individual adatoms were stronger on the SiC_7 sheets compared to corresponding dimers which suggested that formation of dimers is not favorable. Before hydrogenation, the thermal stability of metallized SiC_7 sheets was investigated at 300 K for 6 ps using ab-initio molecular dynamics (MD) simulations. The results of MD simulations revealed that structures were stable at 300 K, which authenticated the reversibility of metal-doped SiC_7 for room-temperature applications.

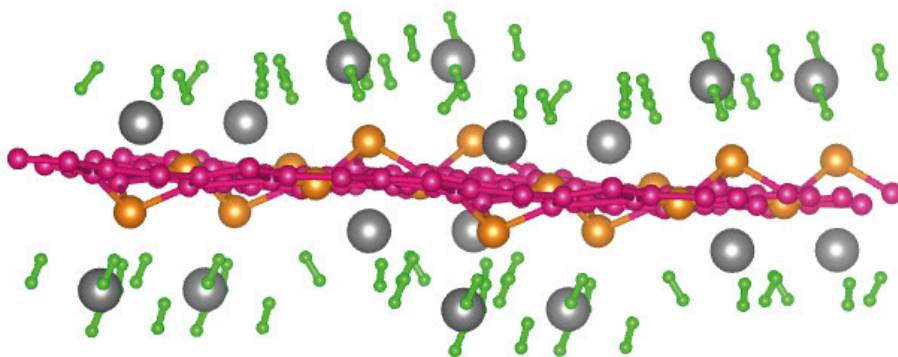


Figure 3.8. The extended view of the Li-doped SiC_7 sheet with maximum H_2 uptake. The adsorption energy of H_2 molecules is 0.286 eV. Here, pink, orange, grey and green colors refer to C, Si, Li, and H atoms, respectively.

Hydrogenation of the metallized SiC_7 sheets revealed that each metal adatom could capture four or five H_2 molecules and the maximum storage capacity was obtained for Li metal which is the lightest amongst all the adatoms. The structure of the hydrogenated Li- SiC_7 sheet is shown in Figure 3.8.

In Table 3.2, the average E_{ads} of metal adatoms, maximum storage capacity, and H_2 adsorption energies are listed, which are the decisive parameters to find the potential of the H_2 storage media. The ratio $E_{\text{ads}}/E_c > 1$, depicted the possibility of uniform and cluster-free distribution of adatoms on the SiC_7 sheets. Our results revealed that highest H_2 storage capacities of 6.34 and 5.63 wt% are obtained in the cases of Li and Na doped SiC_7 sheets, respectively. E_{ads} values of H_2 molecules on all the metallized SiC_7 systems, except K, were found promising for fuel cell applications at room temperature.

Table 3.2. *The adsorption energy of adatom on the sheet (eV), the ratio of adsorption energy to cohesive energy, the adsorption energy of H₂ molecules in the vicinity of adatom (eV) and storage capacity (wt. %) for maximum dopant concentration (12.5%) are listed.*

Adatom (12.5%)	E _{ads} (metal) (eV)	E _{ads} / E _{coh}	E _{ads} (H ₂) (eV)	Gravimetric density (wt.%)
Li-SiC ₇	−1.94	1.19	−0.29	6.34
Na-SiC ₇	−1.50	1.35	−0.24	5.63
K-SiC ₇	−1.96	2.10	−0.13	5.06
Ca-SiC ₇	−1.73	0.94	−0.27	5.03
Sc-SiC ₇	−4.55	1.17	−0.28	4.59

3.3.1.3 Boron carbide (BC₃) sheets under varied Scandium (Sc) doping

The introduction of metal dopants on relatively inert surfaces has proven to be an efficacious procedure that can enhance the reactivity of inert surfaces. This strategy is employed for the capture of gas molecules on nanostructures, particularly for the perspective of gas sensing and H₂ storage [121, 122]. However, the type of charged site (the metal dopant) further decides the binding enthalpy and the mode of interaction between a gas molecule and the doped nanostructure. The efficiency of AM doped carbon nanostructures is reported to decline under the effect of increasing temperature, this phenomenon is not ideal for H₂ storage at room temperature [123]. In the context of adequate H₂ adsorption enthalpy, TM dopants are superior to AM or AEM dopants due to a relatively stronger nature of the interaction between the d-orbitals of TM and the σ or σ^* orbitals of the H₂. However, heavier TM atoms typically cause lower gravimetric capacities due to the large overall weight of the storage system. Another problem arises due to the cohesion of TM atoms as compared to their interaction with the nanostructure, which can hinder the non-uniform distribution of metal atoms on the surface. For higher H₂ uptake and reversibility, metal atoms should uniformly and strongly bind with the surface of nanosheet. For this reason, in the Paper I, we used scandium (Sc) atoms to manipulate the H₂ storage performance of BC₃ sheets. Furthermore, the effect of different doping concentrations on the metal-to-sheet and metal-H₂ interactions were investigated. Based on the previous reports, we expected that the presence of boron atoms in the BC₃ sheet could facilitate the stronger metal-sheet interactions and hinder the metal-metal cohesion [124, 125].

Our computations based on vdW-corrected DFT with GGA-PBE functional depicted that BC₃ sheets are capable to bind Sc atoms with adsorption energies −7.11, −6.02, and −5.45 eV in case of 3.12, 6.25, and 12.5 doping percentages, respectively. Thus, the adsorption energies of Sc were higher than the cohesive energies of Sc reported for the bulk structure [120]. The distances between the metal atoms were adequate for accommodating multiple H₂ molecules. The binding between Sc atoms and the BC₃ sheets was accompanied by the charge redistribution process. The quantification of the charge

transfer between metal and BC_3 was performed with the help of bader technique. Each Sc atom gave a large fraction of its charge to the sheets and resulting positively charged Sc atoms were capable to polarize the H_2 molecules. The adsorption of Sc on BC_3 further affected the electronic structure, thus, a metal-to-semiconducting transformation of the doped BC_3 sheets was noted.

Table 3.3. Average adsorption energies (eV) of H_2 molecules on BC_3 sheets in cases of different Sc content (Sc %).

No. of H_2 / Sc	E_{ads} (eV)	E_{ads} (eV)	E_{ads} (eV)
	3.12 (Sc %)	6.25 (Sc %)	12.5 (Sc %)
1 H_2 /Sc	−0.40	−0.44	−0.53
2 H_2 /Sc	−0.41	−0.43	−0.56
3 H_2 /Sc	−0.41	−0.41	−0.41
4 H_2 /Sc	−0.38	−0.33	−0.38
5 H_2 /Sc	−0.34	−0.31	−0.17

In the case of 12.5 Sc %, we observed the bond dissociation of one H_2 molecule which was situated in the vicinity between two Sc atoms. The charge analysis revealed that the higher charge accumulation in the region between two Sc atoms was responsible for the H_2 bond dissociation. For all the Sc doping concentrations, each metal site could adsorb five H_2 molecules with binding energies in the range of 0.53–0.17 eV. The gravimetric capacity in the case of highest Sc doping concentration was achieved as 5.5 wt %.

3.3.1.4 Li and Na doped Boron Phosphide (BP) sheets

The monolayers of the groups III-V elements, particularly h-BN, have received a huge research interest because of the outstanding mechanical, electronic, and optical properties. Similar to h-BN, boron phosphide (BP) monolayer is currently in the limelight due to its structural resemblance with graphene and h-BN. Theoretical predictions revealed that BP monolayer is a small bandgap (0.91 eV) semiconductor with high mechanical stability [126]. Similarly, the efficient performance of BP monolayer as an anode material for Li, Na, and K ion batteries was reported elsewhere [127]. In paper IX, we investigated the potential of BP monolayer as the H_2 storage media. Similar to h-BN, the BP monolayer showed weak adsorption affinity for H_2 molecules. Therefore, for improvement of the adsorption strength, we introduced light AM atoms (Li and Na) on the BP structure. The study of electronic structure and charge transfer revealed that Li and Na atoms tend to transform the BP structure to metal, meanwhile, each metal atom loses the significant quantity of electronic charge to the BP sheet. We further verified the thermal stabilities of doped BP sheets for room temperature applications.

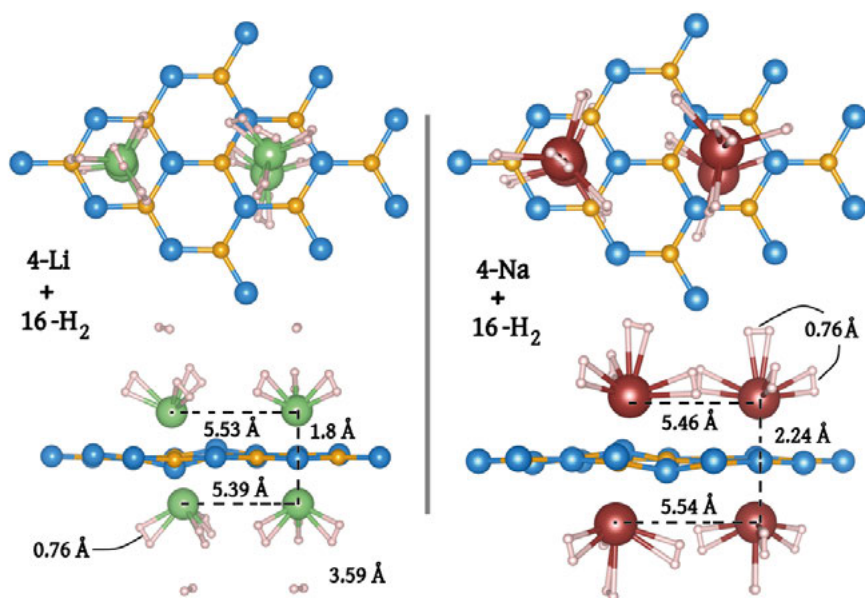


Figure 3.9. Adsorption of multiple H_2 molecules around Li and Na dopants on BP monolayer. Distances between the dopants and average H_2 bond lengths are mentioned for each structure. Here blue, orange, green, red and pink spheres represent B, P, Li, Na, and H atoms, respectively.

High gravimetric capacities of 7.402 and 6.446 wt% with adsorption energies in the range of 0.33-0.19 and 0.24-0.17 eV for Li and Na doped BP, respectively, suggested that BP monolayer could perform as a reversible H_2 storage medium for onboard applications.

3.3.2 Molecular Functionalization for Enhanced H_2 Capture

Besides metal doping, H_2 storage performance of typically inert nanostructures (e.g., graphene, h-BN, CNTs) could be tuned by introducing molecular dopants, such as lithium-rich species or polar molecules which could bind H_2 via physisorption mechanism. The prerequisite for these molecules is the strong interaction with the host structures, which guarantees the reversibility of storage media. Amongst other molecular dopants, Li_2F molecules on fullerenes C_{60} were reported to improve the binding strength of H_2 molecules on the host [128]. Similarly, coatings of small polar molecules OLi and ONa on C_{60} fullerenes were theoretically proposed for high H_2 gravimetric densities [129]. Lithium rich species known as polyolithiated molecules captured particular attention in this context. Several examples of C and O based polyolithiated molecules are available in the literature, for example, OLi, OLi_2 , OLi_3 , CLi, CLi_2 , CLi_3 , CLi_4 [130–133]. In the next sections, we have summarized our

projects where molecular dopants are employed as a tool for improved H₂ storage performance.

3.3.2.1 h-BN sheets with OLi, ONa, and Li₂F molecules

In paper II, hexagonal boron nitride (h-BN) sheets functionalized with OLi, ONa, and Li₂F molecules were investigated for H₂ storage. h-BN sheet, often known as an inorganic alternate of graphene, is mechanically and thermally stable wide bandgap semiconductor. The pristine h-BN structure shows inert behavior towards H₂ molecules which is similar to graphene. The interaction of H₂ and h-BN could be tuned by introducing light-weight molecular dopants on the sheet. Since OLi, ONa, and Li₂F were reported to capture multiple H₂ on carbonaceous structures with optimum binding strength, therefore, the interaction of these molecules with h-BN sheets was investigated. For efficient H₂ capture, the molecular dopants were required to strongly bind with the h-BN sheet having adequate intermolecular separation to accommodate multiple H₂ molecules. In this context, different adsorption sites on the h-BN sheet were taken into consideration, such as hollow of hexagon, B and N top, and BN bridge sites. Different molecular orientations on the sheet were also investigated, for example, the OLi molecule could be vertically placed on the sheet in two possible geometries with either O or Li binding with the sheet or in a horizontal orientation parallel to the sheet. For each molecule, adsorption energies were computed in a similar fashion as in Eq. (3.1). The adsorption energies of OLi and ONa on h-BN were stronger than graphene and CNTs [129, 134].

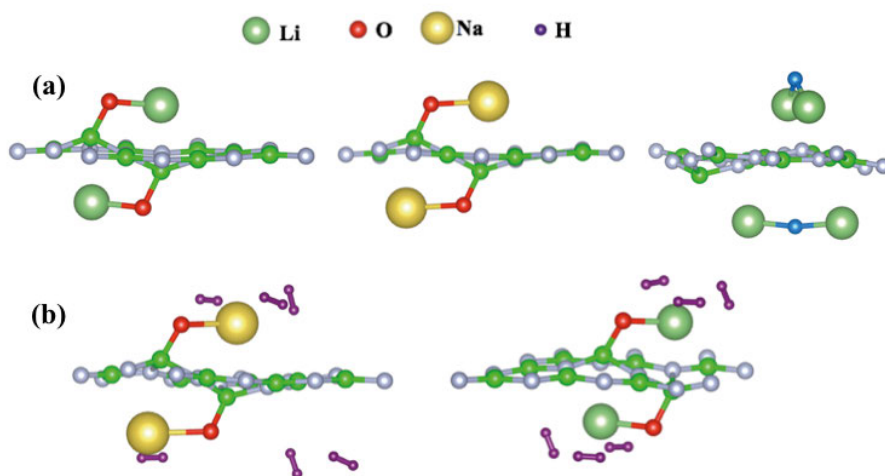


Figure 3.10. Side views of (left to right) (a) OLi, ONa, and Li₂F doped h-BN sheets. (b) OLi and ONa doped sheets with maximum H₂ uptake. Reproduced with permission from Paper III. Copyright © 2017, John Wiley and Sons.

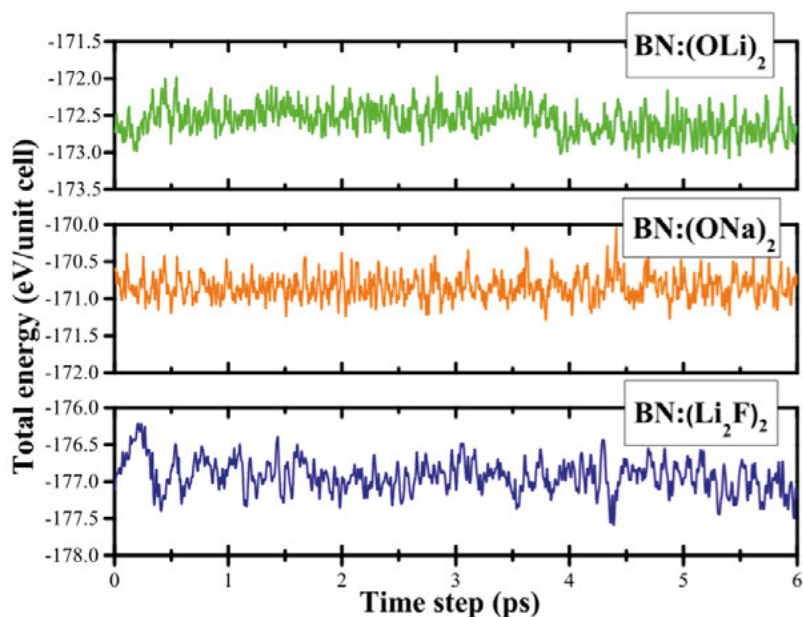


Figure 3.11. Molecular Dynamics (MD) simulation of doped h-BN sheets at 400 K with a time step of 1 ps. Plots represent the variation in energy with respect to time. Reproduced with permission from Paper III. Copyright © 2017, John Wiley and Sons.

We further investigated the thermal stability of doped h-BN sheets at 400 K using MD simulations. The results of MD simulations are shown in Figure 3.11, which depicted that OLi and ONa doped sheets are thermodynamically stable at 400 K. On the other hand, the output structure and the variation in total energy (Figure 3.11) for Li_2F doped h-BN sheets revealed the formation of the molecular cluster which weakly remained intact with the sheet. One of the Li_2F molecules detached from the h-BN sheet and bound with the neighboring Li_2F molecule. The weaker interaction of Li_2F with the h-BN sheets suggested that this structure is not suitable for H_2 storage. However, OLi and ONa doped structures were further considered for H_2 storage studies.

For hydrogenation, each dopant molecule on h-BN sheets was initially exposed to the single H_2 molecule and the corresponding adsorption energies were obtained. The van der Waals corrected adsorption energies for first H_2 molecule on OLi and ONa doped structures were computed as 0.28 and 0.23 eV, respectively. The number of H_2 was then gradually increased to three per dopant and the total of 6 H_2 molecules could be adsorbed on each system. The adsorption energies of H_2 in the case of maximum hydrogenation were 0.21 and 0.20 eV for OLi-BN and ONa-BN structures, respectively. These adsorption energies fall in the acceptable window (0.2 – 0.6 eV) for H_2 storage according to DOE criteria.

3.3.2.2 Carbon Nanotubes (CNTs) with polyolithiated Molecules

Carbon nanotubes (CNTs) have long been in the limelight for their outstanding mechanical, electrical and optoelectronic behavior. Earlier, experimental reports claimed that CNTs are capable to perform as an efficient H₂ storage material at room temperature with considerably high storage capacity (5-10 wt %) [135]. However, further studies depicted that H₂ binds with CNTs via weak Van der Waals forces which are not suitable for fuel cell applications [136, 137]. Meanwhile, surface coating with molecules or adatoms were employed to improve the adsorption enthalpy and storage capacity of CNTs [41, 138–141].

The unfulfilled quest for ideal H₂ storage material inspired us to investigate CNTs doped with polyolithiated molecules (PLMs). In Paper VI, we reported the structure, stability and H₂ storage performance of CNTs doped with PLMs CLi_n (n=1,2,3) and OLi_m (m=1,2,3). The adsorption energies for PLMs were computed using the following equation,

$$E_{ads} = [E(CNT - y CLi_n / OLi_m) - E(CNT) - yE(CLi_n / OLi_m)]/y \quad (3.4)$$

Here, $m = n = y = 1, 2, 3$. The total energies of CNTs with adsorbed PLMs, pure CNT, and PLMs are expressed as the first, second, and third term in the above equation. The electron density plots for all the doped CNTs are given in Figure 3.12.

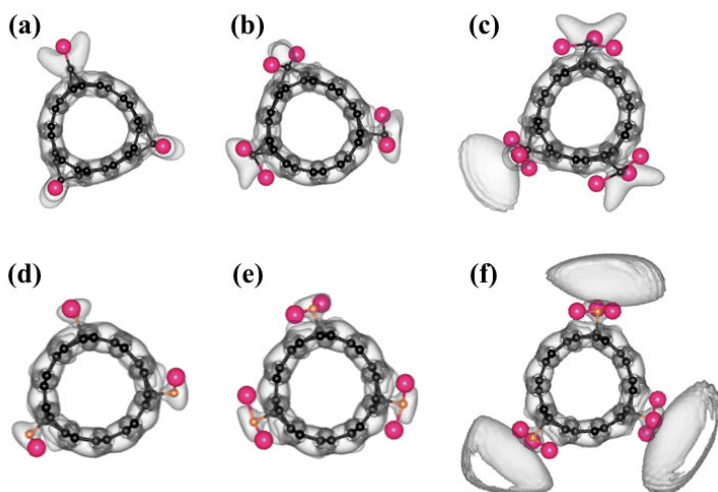


Figure 3.12. Electron density plots (cross-sectional view) for doped CNTs with (a) 3 CLi, (b) 3 CLi₂, (c) 3 CLi₃, (d) 3 OLi, (e) 3 OLi₂, and (f) 3 OLi₃. Plots are obtained with an isosurface value of 0.4 e/bohr³. Here black, orange, and pink colors correspond to C, O, and Li atoms. Reproduced with permission from Paper III. Copyright © 2018 Elsevier B. V. All rights reserved.

The adsorption energies in case of three OLi_n ($n=1,2,3$) and CLi_m ($m=1,2,3$) were -2.00 , -1.51 , -1.00 , -3.08 , -3.35 and -3.63 eV, respectively. The PDOS for OLi_3 and CLi_3 doped CNTs are plotted in Figure 3.13. The electronic structures of pure and functionalized CNTs show metallic behavior. The interaction of each PLM with CNT affects the electronic densities of states, therefore, a significant overlap of the Li (s), O (p) with C_{CNT} (p) states is observed in the case of OLi_n molecules. Similarly, overlapping C_{CNT} (p) with Li (s), C(p) states describes the strong chemical bonding between the CLi_m molecules and CNT.

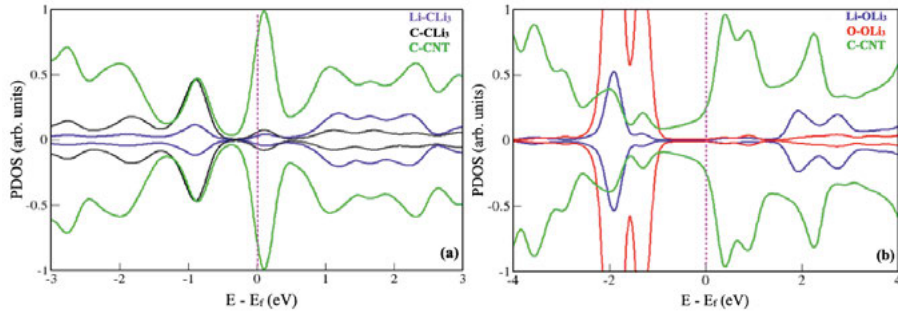


Figure 3.13. Partial density of states (PDOS) plots for doped CNTs with (a) CLi_3 , and (b) OLi_3 molecules.

The interaction of H_2 molecules and the functionalized CNTs is evaluated in terms of adsorption energies of the molecules, according to the following expression,

$$E_{ads} = [E (CNT - CLi_n / OLi_m + zH_2) - E (CNT - CLi_n / OLi_m + (z - 1)H_2) - E (H_2)] \quad (3.5)$$

Here, First and second terms are energies of the functionalized CNTs with z and $z-1$ H_2 . The third term considers the total energy of the H_2 molecule. It is important to mention that the vdW correction of Grimme is included to compute the accurate forces between the molecules and the host [76]. The structures OLi_3 -CNT and CLi_3 -CNT which yield maximum H_2 capture are shown in Figure 3.14. Large H_2 uptake with adsorption energies in the range (0.33 – 0.15 eV) suggested that CNTs doped with OLi_3 and CLi_3 molecules should be experimentally tested as the H_2 storage materials.

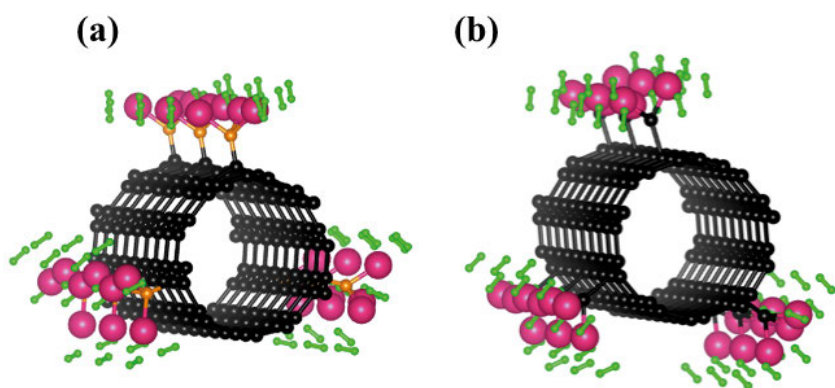


Figure 3.14. The structure of fully hydrogenated (a) OLi_3 and (b) CLi_3 doped CNTs yielding the maximum H_2 capture. Black, pink, orange, and green colors correspond to C, Li, O, and H atoms, respectively.

4 Two-dimensional (2D) Structures for Gas Sensing Applications

Gas sensing is a process of identifying or quantifying the nature, presence and, properties of various pollutants, such as toxic molecules or organic vapors. Various pollutants are emitted in the atmosphere through industrial, transport and biological processes. Amongst them, gases such as carbon dioxide (CO_2) and methane (CH_4) enormously contribute towards global warming which is one of the biggest problems of the present era. These gases are produced from the combustion of fossil fuels and degradation of organic matter [142]. CH_4 in lower concentrations is non-hazardous, however, concentrations higher than 4.5 % in the air could be dangerous because of the combustible nature of this gas. Similarly, CO_2 which is an odorless and colorless gas causes headaches, dizziness, and shortness of breath with a concentration of 1-3 % in the air. Its concentrations above 3 % can cause hypercapnia, a condition that effects the pH value of blood and consequently leads to brain dysfunction and unconsciousness. Elevated concentrations of CO_2 above 5-10 % can lead to a sudden death [143]. Carbon monoxide (CO) is another side-product of the incomplete combustion of fossil fuels, which is reported to cause serious health issues including heart problems at concentrations above 100 ppm (parts per million) [144]. Industrial processes and combustion of sulfur contaminated fossil fuels result in the emissions of sulfur-containing toxic gases, for example, hydrogen sulfide (H_2S) and sulfur dioxide (SO_2). H_2S which smells like a rotten-egg causes irreversible damage to the tissues at the concentrations higher than 3×10^{-3} % [143]. Similarly, SO_2 causes mild to severe problems in the eyes, nose, skin and the respiratory system. Besides above-mentioned gases, monitoring and detection of nitrogen oxides (NO_x) and ammonia (NH_3) are also crucial due to their adverse effects on the climate and public health [145]. Such gases are produced through natural, agricultural and industrial factors such as lightning strikes, agricultural fertilizers/manures, and fuel combustion. Serious health hazards of NO_x and NH_3 at higher concentrations include metabolic and hematologic problems, abnormal blood pressure, vomiting, diarrhea, and respiratory failures. Gas sensor devices based on different types of materials are being utilized for the sensing of these molecules, such as conducting polymers, semiconducting metal oxides, graphene, and CNTs. This chapter summarizes our results of DFT based computations on 2D materials for their pro-

spective gas sensing applications. Before discussing the performance of sensing materials, it is important to understand the mechanism behind the gas sensing and important parameters related to the sensing performance.

4.1 Basic Mechanism of Gas Sensing

The conventional metal oxide sensors usually offer the advantage of cost-effectiveness and sensitivity, however, higher temperatures and large power are required for the normal operation. Within a required range of operating temperature (typically 200 to 500 °C), oxygen ions adsorbed on the surface of metal oxide materials react with incident gas molecules and resulting changes in the conductivity of metal oxides are measured. These oxygen ions (O^{2-} , O^- , and O_2^-) negatively charge the surface, therefore, an increase in the conductivity of metal oxide is observed when an electron donor molecule interacts with the oxygen ions and donates the negative charge. Likewise, the electron acceptor gas interacts with the ions and receives a negative charge, hence the conductivity of sensing material decreases [146]. The mechanism of gas sensing in graphene and other analogous structures is different from metal oxide sensors. In those cases, charge transfer directly occurs between the nanosheet and the gas molecules. Incident gas molecules can either accept or donate the charges to the sensing material [147]. The amount of charge transfer and the direction of charge depletion affects the resistance of sensing materials. The sensing material retains its initial resistance when gas molecules are desorbed due to the temperature or pressure changes. This mechanism of gas detection is reported for various nanosheets including MoS_2 , graphene, ZnO , and Ti_2CO_2 MXenes [148–151]. In Figure 4.1, the distribution of surface charge density for V_2NS_2 MXene with adsorbed NH_3 molecule is plotted which shows that the gas adsorption on V_2NS_2 MXene causes a depletion of negative charge $\sim 0.048e$ from NH_3 molecule to the sheet. The detailed charge analysis of NH_3 molecule depicted that N atom carries a negative charge $\sim 1.207 e$ and H atoms on average lose a charge $\sim 0.4 e$.

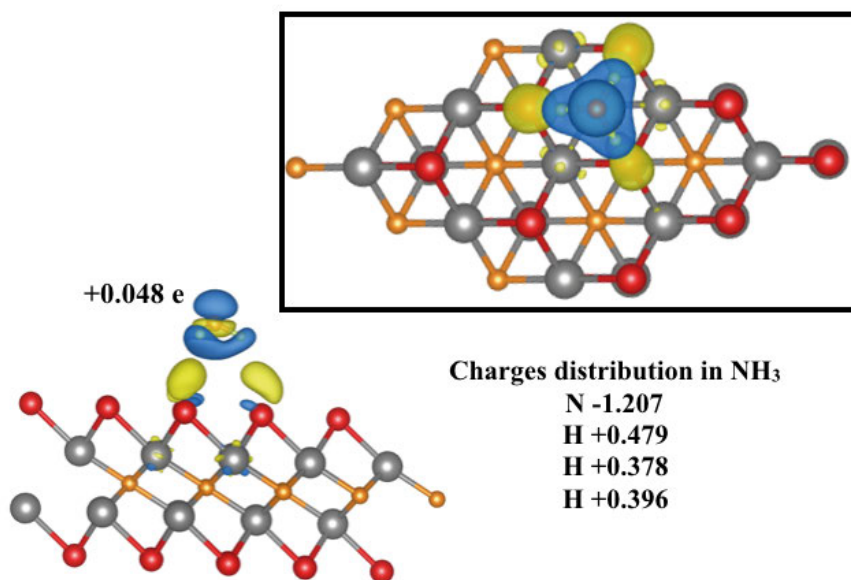


Figure 4.1. Isosurface charge density distribution for V_2NS_2 MXene sheet with adsorbed NH_3 molecule. Positive and negative regions of charge are blue and yellow, respectively. The NH_3 molecule loses a net charge of ~ 0.048 e to the surface. Here, Red, Grey, light green and orange spheres indicate S, V, H and N atoms, respectively.

4.2 Gas Sensors Based on 2D Nanostructures

The sensing performance is quantified based on the parameters such as sensor response, stability, selectivity, sensitivity and recovery periods. Several sensors are designed and utilized till date, however, some of the required performance criteria are not fulfilled or the operating conditions are strenuous. Semiconducting metal oxide sensors are low cost and sensitive materials which are conventionally used for gas sensing but suffer from low selectivity and difficult operating conditions (for example, operating temperature and power consumption) [152]. On the contrary, CNTs are reported to manifest high selectivity and sensitivity at room temperature but extended recovery periods limit their applicability [48]. The hunt for efficient sensing material possessing high sensitivity and selectivity with desired operating conditions has resulted in the persistent development of novel 2D nanostructures. Hereof, graphene and analogous structures with extraordinary mechanical attributes, the large surface area for gas adsorption, and fast carrier mobility are reported as efficient sensors. Examples include graphene oxides (GO), h-BN, transition metal dichalcogenides (TMDs), silicene and phosphorene monolayers in pure and functionalized forms [147]. Despite appreciable attempts for designing

and developing materials, several factors still hinder the efficiency of nanoscale gas sensors, e.g., low sensitivity for some pollutants, poor selectivity, irreversible adsorption, and sensitivity to environmental factors. The sensitivity of a sensor is mainly affected by two factors (a) electrical noise and (b) quality/strength of the signal. Most of the sensing materials suffer from these problems, therefore, the quest for ultrasensitive nanomaterial remains unsatisfied [153]. In this context, we theoretically investigated the capability of S-terminated nitride MXenes (Paper VII) and functionalized BC_3 sheets (Paper VIII), as summarized in the following sections.

4.2.1 MXene Sheets

The first MXene sheet was synthesized in 2011 and after that several new members emerged in the family with outstanding attributes, such as high thermal and mechanical stability, flexibility, acid-resistance and superior capacity of ion-exchange [154, 155]. The extraordinary role of MXenes for batteries, hydrogen storage, catalysis, supercapacitors, and gas sensing applications are reported in the literature [153, 156–159]. The ultra-high sensitivity of Ti_3C_2 MXene for Volatile Organic Compounds (VOCs) makes it superior to graphene and MoS_2 gas sensors. The detection of VOCs in exhaled breath with a part per billion (ppb) accuracy could be achieved due to the low noise and high quality of the signal in the MXene sensor [153]. Here, we theoretically investigated the sensing properties of one of the thinnest MXenes M_2N ($\text{M} = \text{Ti}, \text{V}$). In our study, we considered sulfur(S) terminations on M_2N MXenes which were previously not studied for gas sensing, however, their remarkable behavior for anode applications in batteries was reported [160].

Table 4.1. *The structural parameters for M_2N ($\text{M} = \text{Ti}$ and V) sheets with and without the surface terminations.*

Structure parameters (Å)	Ti_2N	Ti_2NS_2	V_2N	V_2NS_2
Lattice constant	2.93	3.16	2.83	3.09
$D_{\text{Metal-Metal}}$ (In-plane)	2.86	2.96	2.69	2.75
$D_{\text{Metal-Metal}}$ (Out-of-plane)	2.93	3.16	2.83	3.09
$D_{\text{Metal-Nitrogen}}$	2.04	2.16	1.97	2.06
$D_{\text{Metal-Sulfur}}$	-----	2.39	-----	2.35

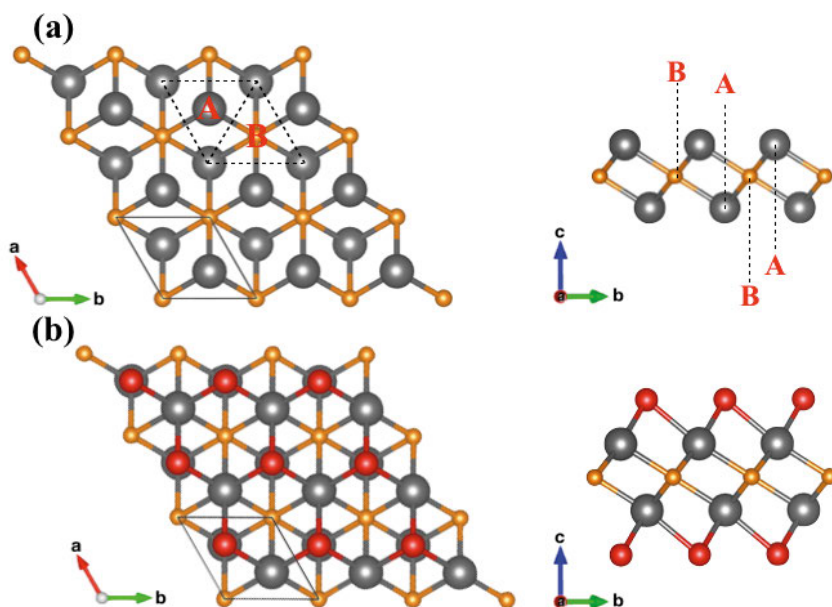


Figure 4.2. Top and side views of (a) Relaxed V_2N MXene sheet without surface terminations. The region enclosed by solid lines indicates the unit cell. The hollow sites of triangles A and B (enclosed by dotted lines) denote the possible adsorption sites for surface terminating atoms, and (b) Relaxed V_2NS_2 MXene sheets. Here, Red, Grey, and orange spheres indicate S, V, and N atoms, respectively.

The structure of 2D transition metal carbides/nitrides is described with a chemical formula $M_{n+1}AX_n$ ($n=1, 2$, or 3), where “M” is the transition metal, “X” stands for C or N, and “A” element belongs to group IIIA or IVA in the periodic table [161, 162]. MXenes are terminated with surface terminal groups ($T=O, F, OH$ or S) and the properties of these sheets are distinctive based on the type of their surface terminations. The unit cell of Ti_2N and V_2N sheets were first relaxed and then S adsorption on both sides of the sheets was achieved. Transition metal ions can generally form six bonds with the surrounding atoms due to the coordination number 6, therefore, the surface terminated structures M_2NS_2 are formed. S atoms could adsorb on two types of hollow sites (A and B), as highlighted in Figure 4.2(a). We checked four different possibilities for both sided surface terminations and named them as models 1, 2, 3 and 4. In model 1, hollow A sites were chosen for both sides S coverage. Similarly in model 2, S atoms were allowed to relax at hollow B sites. In Model 3, the possibility of S adsorption on top of the transition metal atoms was tested. In model 4, S atom on one side of the sheet adsorbs on A site and on the other side it adsorbs at the B site. The structure of Ti_2N MXene with and without the surface terminations are shown in Figure 4.2(a-b), re-

spectively. Detailed description of the structure and our computational methodology are contained in paper VII. We investigated the adsorption behavior of eight gases CH₄, CO, CO₂, SO₂, H₂S, NO₂, NO, and NH₃ on Ti₂NS₂ and V₂NS₂ MXene sheets. The adsorption energies are computed using the following formula,

$$E_{ads} = E_{MXene+Gas} - E_{MXene} - E_{Gas} \quad (4.1)$$

here, first, second and third terms in the above expression represent the total energies of the MXene sheet with the adsorbed molecule, pristine MXene sheet, and the gas molecule, respectively.

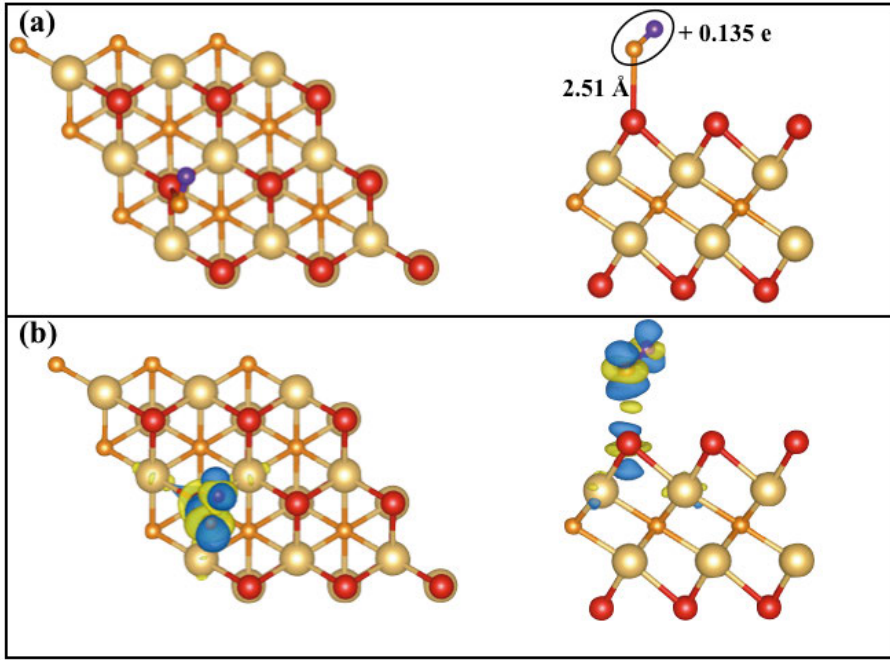


Figure 4.3. Top and side views of (a) Ti₂NS₂ sheet with adsorbed NO molecule. The net charge on the molecule is +0.135 e. The distance between the molecule and sheet is 2.51 Å. (b) Isosurface charge density plot for NO molecule adsorbed on the Ti₂NS₂ sheet. Yellow and blue colors indicate the negative and positive charge regimes, respectively. Red, golden, and orange spheres indicate S, Ti, and N atoms, respectively.

The adsorption of gases on M₂NS₂ sheets leads to the charge redistribution on the surface and affects the electronic structure of the MXene sheets. Charges on the adsorbed molecules and MXene sheets were quantified with the help of bader charge technique. Here, it is worthwhile to mention that E_{ads} values of atoms and molecules reported in this thesis are always negative because the

interactions are exothermic and kinetically favored. Adsorption studies revealed that both MXene sheets show comparatively stronger interactions with the molecules NO, NO₂, H₂S, and SO₂. E_{ads} values in most cases fall in the physisorption or weak chemisorption regime of molecular interactions with the sheets, which is suitable for efficient and fast recovery of the sensing device after gas detection. Charge analysis describes that CO₂ and SO₂ act as charge acceptors on both the sheets and receive some fraction of electronic charges from the nearest atoms on the host. The NO molecule gets adsorbed on the Ti₂NS₂ sheet with the strongest adsorption affinity (−0.406 eV) amongst all. The structure and isosurface charge density for NO molecule on the Ti₂NS₂ sheet are shown in Figure 4.3. The adsorption process leads to a reshuffling of the surface charges and the NO molecule carries a net charge equal to +0.134 e. The careful analysis of the charges by bader technique reveals that the N atom in the NO molecule donates the charge equivalent to 0.160 e to the sheet and O atom receives the charge 0.026 e. As a consequence of the charge donation, the bond length of the NO molecule reduces to 1.16 Å, whereas the pre-adsorption bond length is 1.17 Å. The adsorption of molecules also affects the electronic structure of MXene sheets which plays a vital role in the gas detection. The total density of states (TDOS) plot for NO molecule adsorbed on Ti₂NS₂ sheets is shown in Figure 4.4.

Here, a significant effect of NO adsorption on the electronic structure is visible around the Fermi level, as the peaks become broader and shift towards the Fermi level. NO molecule is paramagnetic in the gaseous state, therefore, the molecule induces magnetism in the Ti₂NS₂ sheet upon adsorption. Similar investigations on all the gases revealed that both M₂NS₂ sheets show high sensitivity towards NO, NO₂, H₂S, and SO₂ molecules. Particularly, the adsorption energies of NO and NO₂ molecules are favorable for reversible gas sensing, which means that gases can be detected on the MXene sheets and later the structure can quickly retain its pristine state. Our findings reveal that the Ti₂NS₂ and V₂NS₂ sheets can function as efficient nanosensors materials for NO and NO₂ molecules. Sensing of the material for other gases is comparatively lower but we expect that it could be enhanced by applying the external electric field or tensile strain as previously achieved for the Sc₂CO₂ and Ti₂CO₂ MXenes-based SO₂ and NH₃ sensors.

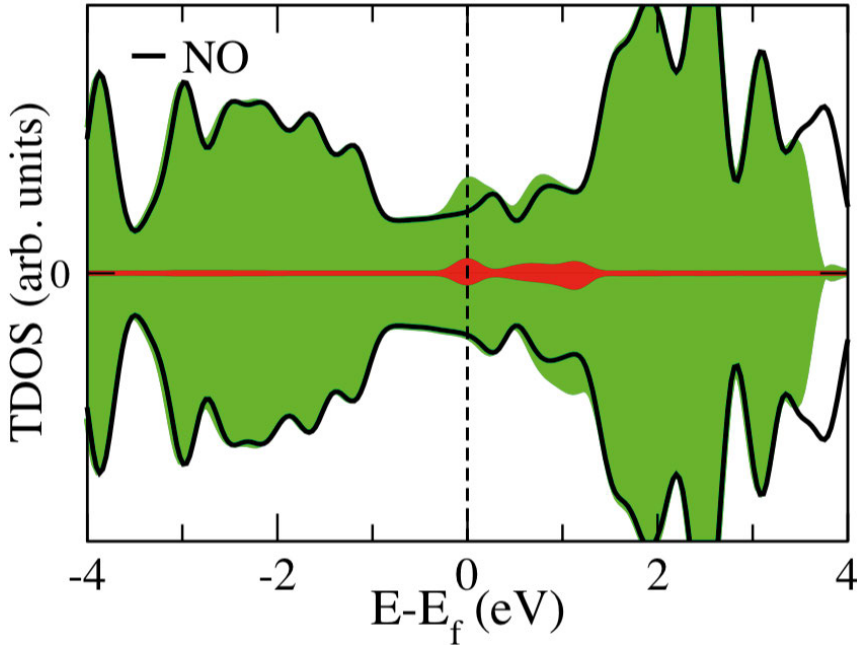


Figure 4.4. Total density of states (TDOS) plot for NO molecule adsorbed on the Ti_2NS_2 sheet. The red shaded region represents the projected DOS for the NO molecule. The black solid line indicates the TDOS for the Ti_2NS_2 and the green shaded region represents TDOS of the Ti_2NS_2 after NO adsorption.

4.2.2 Metal Functionalized BC_3 Sheets

Carbon-based nanomaterials, particularly graphene, hold great potential for the applications in the field of nanoscale gas sensing owing to a large surface area, superior conductivity, and fast mobility of electrons. Reduced electrical noise in graphene compared to the conventional sensors creates the possibility of an exceptional gas sensing response. Similarly, humidity which acts a limiting parameter for the performance of the gas sensors, no longer remains an issue because the graphene-based sensors are reported to overcome humidity related sensing issues without external heating [163]. Dopants and defects can further enhance the sensitivity of graphene and other carbon-based nanostructures. The properties of graphene, however, greatly vary depending on the type of dopant, for instance, boron (B) doping in graphene could enhance the sensitivity for NO and NO_2 molecules [164]. The size of the B atom is similar to C, which makes it feasible to design B-C based functional materials. The experimental synthesis of the BC_3 sheet is one such milestone discovery that opened up the possibility to design a sensor with exceptional sensitivity and selectivity. The structural resemblance with graphene, semiconducting nature, high strength and mechanical stability, good optical response, and heat conductivity make BC_3 sheets interesting for nanoscale device applications.

In Paper VIII, we investigated the gas sensing performance of BC_3 sheets for carbonaceous pollutants CO , CO_2 , and CH_4 . The adsorption energies of molecules were computed on pristine BC_3 sheets which revealed that the CH_4 weakly binds to the BC_3 sheet with an adsorption energy of 0.14 eV. Likewise, the weak physisorption governs the interaction of CO_2 with BC_3 sheet with a adsorption strength of 0.19 eV. The adsorption energy of CO molecule (0.74 eV) depicts a relatively higher sensitivity of pristine BC_3 sheets for CO as compared to the other two gases. To enhance the sensitivity of BC_3 sheets for CO_2 and CH_4 molecules, we employed the metal-doping strategy. Previously metal dopants, such as, aluminum (Al) and lithium (Li) were reported to improve the sensitivity of graphene- and hydrogenated graphene-based sensors, respectively [165, 166]. Here, we doped BC_3 sheets with light AM (Li, Na, K) and AEM (Be, Mg, Ca) atoms and observed the enhanced sensing aptitude of the metal-doped sheets. Pristine BC_3 sheets were semiconducting with an indirect bandgap of 0.65 eV. Metal atoms strongly adsorbed on the pristine BC_3 sheets and donated the bulk of their atomic charges to the sheet. Metal adatoms could bind with the BC_3 sheet uniformly without cluster formation, which is an important attainment towards material design. The electronic structure of the BC_3 sheets turned metallic upon metal doping as the new electronic states emerge around the fermi level. In Figure 4.5(a-b), the adsorption geometry, the partial electronic density of states (PDOS) and isosurface charge density are shown for Li doped BC_3 sheets.

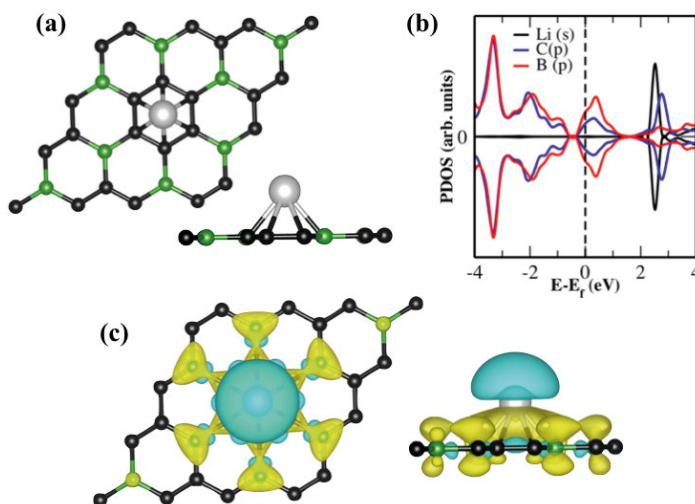


Figure 4.5. (a) Top and side views, (b) Partial density of states (PDOS) plot, and (c) Isosurface charge density distribution for Li doped BC_3 sheets. Here green, black, and silver spheres represent B, C, and Li atoms, respectively.

To estimate the sensitivity of doped BC_3 sheets for gas molecules, we investigated the charge distribution, electronic structure and work function of the

BC₃ sheets before and after the gas adsorption. The work function which is computed as a difference of electrostatic potential at the level of vacuum and the energy at the Fermi level, is a useful parameter to detect gases. Particularly, surface work function variation (SWF) sensors work on the principle of the work function measurement as the gases adsorb on the sensitive surface. Our computations revealed that the work function of the sheets before and after the gas adsorption significantly changes owing to the sensitive nature of doped BC₃ sheets for all the gas molecules. In Figure 4.6(a-c), the total density of states (TDOS) for Li doped BC₃ sheets with and without CO, CO₂, and CH₄ adsorption are plotted. The change in TDOS after the gas adsorption, particularly near the Fermi level, facilitates the process of gas detection.

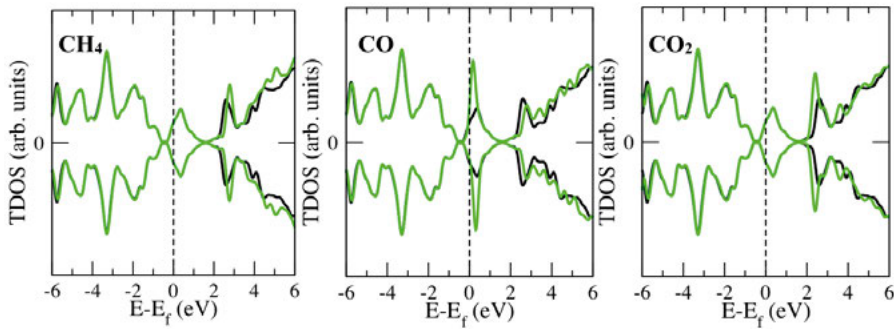


Figure 4.6. Total density of states (DOS) plots for Li doped BC₃ sheets with CH₄, CO, and CO₂ molecules (Left to right). Green and black lines indicate the TDOS of Li doped BC₃ with and without adsorbed gases, respectively.

5 Tuning the Structure and Electronic Properties of 2D Materials

Design and synthesis of novel materials are constantly revolutionizing the electronic industry for almost the last 75 years. Research on 2D materials is increasing day by day and new members are being added to the family, namely, graphene, hydrogenated-graphene, graphyne, graphone, graphdiyne, silicene, germanene, silicane, phosphorene, antimonene, arsenene, borophene, hexagonal boron nitride, boron carbide, MXenes and transition metal dichalcogenides (TMDs). These materials have captured great interest owing to their outstanding and diverse chemical, electrical, optical, mechanical and electronic characteristics. Amongst other 2D materials, graphene, TMDs, and MXenes are being tested for the fabrication of the nanoscale electronic devices. However, except graphene, none of the available 2D materials has yet been commercially employed for large-scale manufacturing of the devices [167]. For improved performance, tuning or readjustments of the material properties by means of doping, chemical modifications, electric field, compression, and strain is often required.

With advanced computational tools, now it is possible to access the properties of materials under the effect of external tuning parameters. Theoretical predictions of the material properties under varied external factors not only facilitate the experimental design and testing but also provide a better picture of the ongoing physical phenomena. In this chapter, the role of adatoms/dopants on the properties of 2D stanene sheet is discussed. Detailed results and methodology of our theoretical investigation are available in paper IV.

5.1 Doping Characteristics of Stanene Monolayer

Stanene, as the suffix *ene* suggests, is an elemental 2D material composed of Sn atoms. This monolayer is semiconducting with a small bandgap (72 meV) and manifest structural similarity with other group IV monolayers, namely, silicene and germanene [168]. Semiconducting nature, high dynamic stability, and room-temperature Quantum Anomalous Hall (QAH) effect make it interesting for the optoelectronic industry [169]. Previous studies revealed that doping with adatoms could enhance the potential of 2D structures for various applications, e.g., hydrogen storage, photocatalytic activity, super-capacitance

and gas sensing performance [160, 170–173]. We, hereby, investigated the structural distortions and electronic properties of pristine and doped stanene monolayers with 31 different adatoms from AM (Li–K), AEM (Be–Ca), TM (Sc–Zn) and metal/non-metals (Al, Ga, B, Si, Ge, As, C, N, O, P, S, Se, F, Cl, Br) of groups III–VII in the periodic table. We further investigated the adsorption energies, charge transfer, and change in the surface work function for doped stanene sheets.

5.1.1 Adsorption Energies and Diffusion Pathways

Stanene monolayer is a buckled structure consisting of hexagonal rings of sp^3 bonded Sn atoms. The adsorption sites for adatoms are H (hollow), B (bridge), T (top), and V (valley), as indicated in Figure 5.1. We investigated the adsorption behavior of all the adatoms on these four adsorption sites. The differences in the adsorption energies between nearest adsorption sites yield the information about energy barriers for the diffusion of adatoms on the monolayer. The strongest adsorption energies and corresponding adsorption positions are listed in Table 5.1. In view of cluster-free adsorption of adatoms, the experimental cohesive energies (E_{coh}) in the bulk phase were compared with the adsorption energies of adatoms on the stanene monolayer [120]. In most cases, the adsorption energies are stronger enough to ensure a uniform distribution of adatoms on the stanene sheet, which further ensure that atoms can form 2D layers on stanene surface. The detailed description of migration energies of all the adatoms is provided in Paper IV. Here, we discuss the selective cases from different groups of atoms.

All the AM atoms (Li, Na, K) behave alike and prefer the H site for adsorption. B site acts as a non-stable (transition state) adsorption site and the adatom moves to the nearest V site. Similarly, T site is the least favorable for adsorption of AM adatoms. Conversely, AEM atoms (Be, Mg, Ca) differently interact with stanene monolayer, for example, Mg and Ca prefer to get adsorbed at H site, unlike Be atom which strongly binds at V site with a adsorption energy of 3.152 eV. TM atoms strongly interact with stanene monolayer as compared to other group IV monolayers.

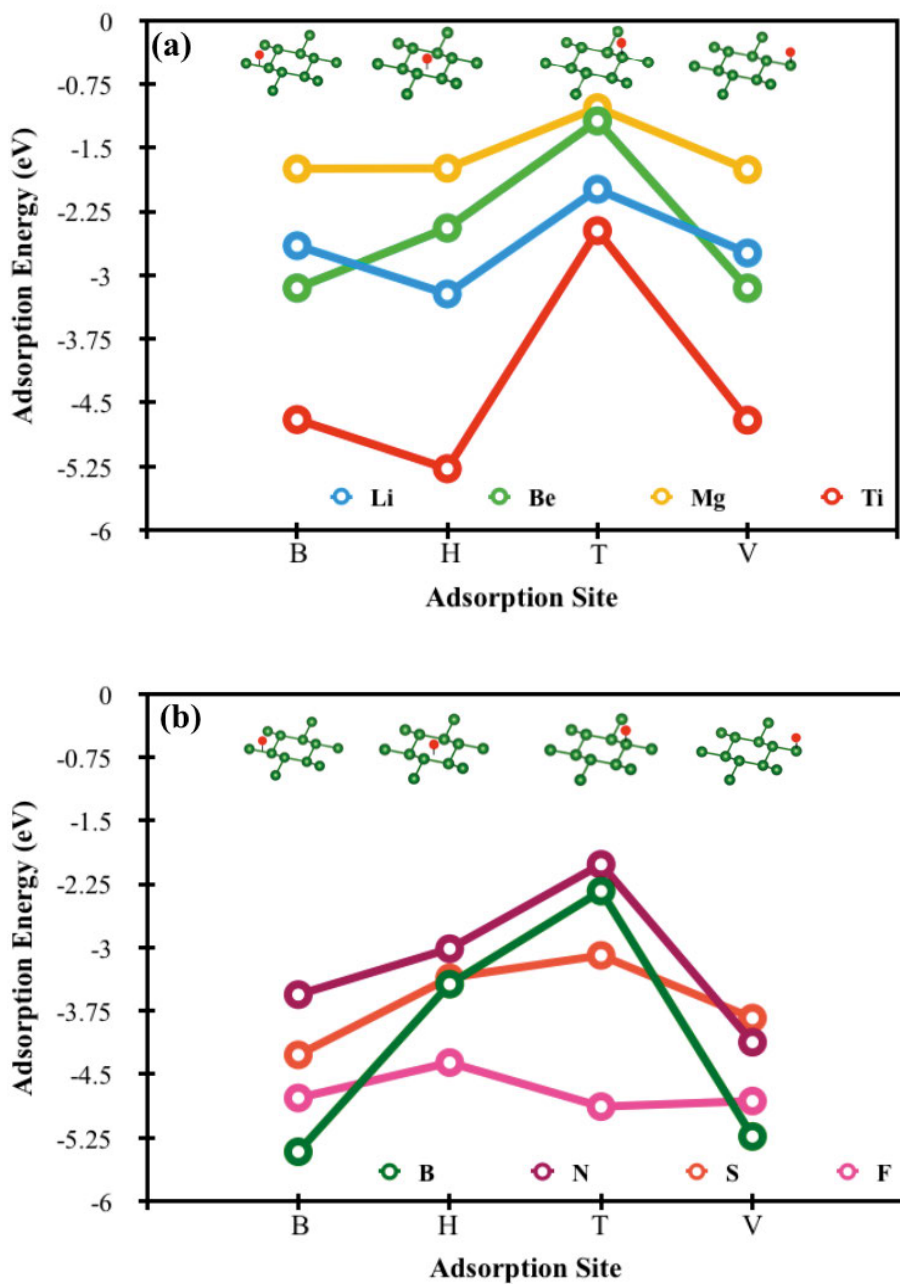


Figure 5.1. The adsorption energies of (a) Metals (Li, Be, Mg, and Ti), (b) Group III-VII elements (B, S, N, and F) for different possible adsorption sites.

Table 5.1. For each atom on stanene monolayer, most stable adsorption sites (B, H, T, and V indicating bridge, hollow, top, and valley sites, respectively), the adsorption energies (eV), $E_{\text{ads}}/E_{\text{coh}}$, and structural distortion δ_{Sn} (10^{-1} Å) are listed.

Adatom	Adsorption site	Adsorption energy (eV)	$E_{\text{ads}}/E_{\text{coh}}$	Distortion δ_{Sn} (10^{-1} Å)
Li	H	-3.220	1.98	0.0
Na	H	-2.643	2.37	0.2
K	H	-2.694	2.88	0.4
Be	V	-3.152	0.94	0.2
Mg	H	-1.756	1.16	0.2
Ca	H	-3.351	1.82	0.2
Sc	H	-4.938	1.27	0.0
Ti	H	-5.277	1.09	0.1
V	H	-4.214	0.79	0.1
Cr	H	-3.019	0.73	0.0
Mn	H	-3.075	1.05	0.0
Fe	H	-3.759	0.88	0.2
Co	V	-4.281	0.97	0.2
Ni	V	-4.839	1.09	0.2
Cu	H	-3.282	0.94	0.0
Zn	V	-1.162	0.86	0.1
B	V	-5.410	0.93	0.3
Al	B	-3.390	1.0	0.1
Ga	H	-3.240	1.15	0.3
N	V	-4.120	0.84	0.3
P	V	-3.670	1.08	0.0
As	T	-3.680	1.24	0.3
O	B	-5.700	2.19	0.0
S	B	-4.270	1.49	0.2
Se	B	-3.850	1.56	0.2
F	T	-4.880	0.84	0.0
Cl	T	-3.490	2.49	0.1
Br	T	-3.060	2.51	0.3

H site is preferred by most of the TM atoms in minimum energy configuration except Ni, Co, and Zn, whereas B is the transition site for all the TM atoms except Zn. Compared to all the TM atoms, the strongest interaction with stanene monolayer is noted for Ti which also experiences a high migration energy barrier between different adsorption sites. Group IIIA elements, B, Al, and Ga show distinct adsorption trends on stanene, as B atom prefers V site, whereas Al and Ga prefer B and H sites for adsorption, respectively. Group IVA elements (C, Si, Ge, and Sn) adsorb on the stanene monolayer and lead to structural instability, as confirmed by MD simulations at the temperature of 150 K. Group (V-VI)A elements strongly bind on stanene monolayer (with $E_{\text{ads}}/E_{\text{coh}} > 1$) in most cases. Similarly, halogens Cl and Br strongly interact with the sheet and F exhibits weaker interaction, as indicated by $E_{\text{ads}}/E_{\text{coh}}$ ratios for each of these atoms. In Figure 5.1(a-b), the adsorption energies against the

adsorption site are plotted for selective atoms from different groups of the periodic table.

5.1.2 Structural Deformations

The adsorption of adatoms leads to different structural changes in the stanene monolayers, for example, Be atom propels the Sn atom at V site and substitutes it. Mg atom adsorbs on the V site forming a dumbbell type structure by slightly repelling Sn atom out of the sheet.

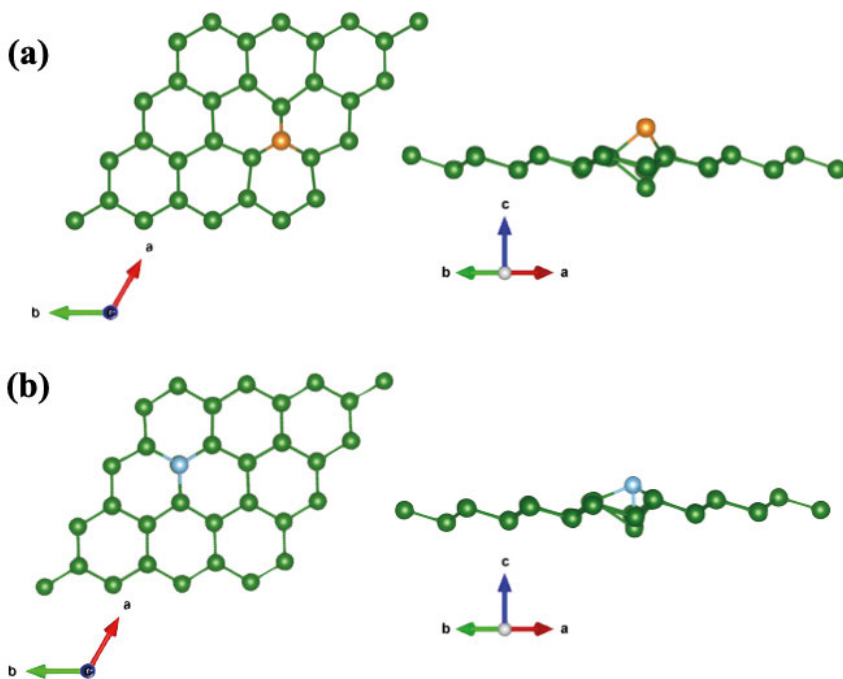


Figure 5.2. Structural changes in stanene monolayer due to (a) Mg, and (b) Ti atom adsorption.

Similarly, all the TM atoms placed at V site repel Sn atoms out of the sheet and form dumbbell structures. We quantified the structural distortion δ_{Sn} by computing the change in z-coordinate of the Sn atoms before and after adatom adsorption. Due to the higher structural stability, only small distortions (<0.05 Å) are observed for each case, as listed in Table 5.1. In Figure 5.2, Mg and Ti adsorption on the stanene monolayer on V site is shown where structural distortion and formation of dumbbell structure are apparent.

5.1.3 Electronic Structure and Charge Analysis

The adsorption of adatoms on the stanene surface is further accompanied by charge redistributions between the adatoms and the monolayers. Each atom interacts with the monolayer via charge donation or acceptance based on the electronegativity of dopant with respect to Sn atoms in stanene monolayer. For the cases when electronegativity of adatom is lower than Sn, the charge transfer takes place from adatom to the sheet, e.g., AM, AEM, and TM atoms except for Ni, Co, and Cu. Similarly, higher electronegativities of adatoms cause the transfer of charges from sheet to adatom, e.g., O, F, and Cl.

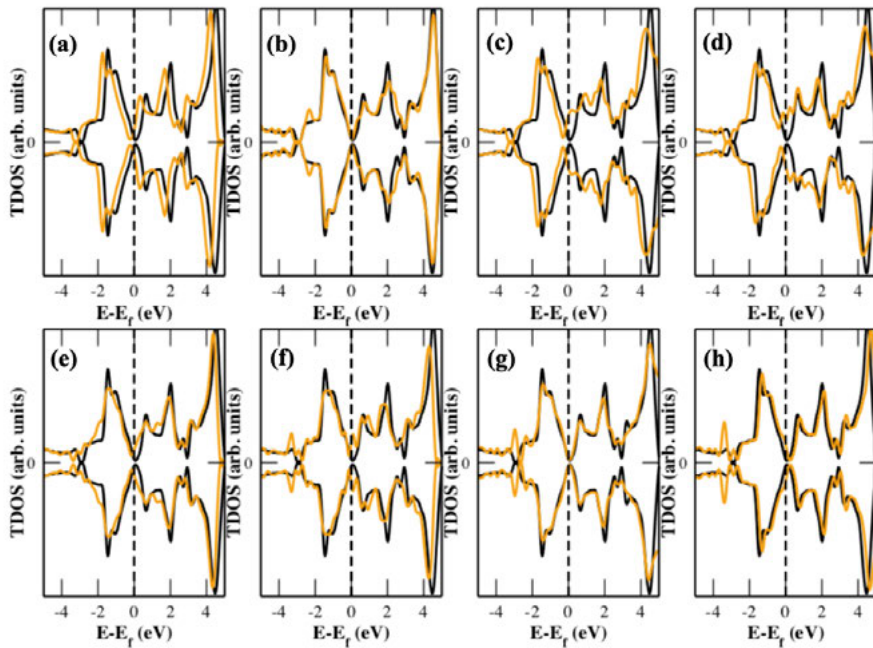


Figure 5.3. TDOS for pristine (black) and doped stanene (orange) sheets with (a) Li, (b) Be, (c) Sc, (d) Ti, (e) B, (f) N, (g) O, and (h) F atoms.

The interaction of adatoms further affects the electronic structure of the stanene sheets. The black and orange lines in the plots indicate TDOS for pristine and doped stanene sheets. The TDOS of stanene sheets with and without adsorbed adatoms (Li, Be, Sc, Ti, B, N, O, and F, respectively) are plotted in Figure 5.3(a-h) where the broadening and shifting of the electronic states are visible close to the Fermi level.

Part III:
Final Remarks

6 Summary and Outlook

The rate of worldwide fossil fuel consumption is alarmingly high which points towards the possible energy crisis in the near future. Besides the sharp decay of fossil reserves, the combustion of hydrocarbons is associated with the emission of hazardous gases in the environment. Global warming caused by the emission of CO₂ and other greenhouse gases does not only call for sustainable, economical, and environmentally benign harvesting of energy but also demands the development of efficient gas sensors or capturers. In this thesis work, low-dimensional materials are designed and investigated for their applications in the field of clean energy harvesting and gas sensing. We used van der Waals (vdW) corrected density functional theory (DFT) to compute and modify the properties of the materials at the atomic scale for applications in the aforementioned fields.

The detailed theoretical background of DFT along with computational methods is presented in *Chapter 2*. The interaction of molecules with nanostructures is typically administered by long-range forces that aren't contained in the Kohn-Sham (KS) DFT. Therefore, vdW correction terms are deliberately included in the DFT computations for an accurate depiction of the total free energy of the system and other material properties.

In *Chapter 3*, the strategies of materials-based hydrogen (H₂) storage are discussed along with the challenges and limitations of chemisorption and physisorption techniques. H₂ is an ideal carrier of energy due to its high energy content and abundance in nature. Being an environment friendly, economical and sustainable energy carrier, H₂ is capable to completely replace fossil fuels for energy applications. However, the gaseous nature and low volume density of H₂ makes it difficult to store for practical applications. Conventional ways for storing H₂, liquefaction and pressurized hydrogen, are considered unsafe and economically impracticable.

Chemical storage of atomic hydrogen in solid-state materials, such as metal hydrides, is glimpsed as a viable solution for H₂ storage, however, the inadequate adsorption energies and unfavorable adsorption/desorption kinetics hinder the reversibility and practicability of the storage medium. The physical adsorption of H₂ on the surfaces of nanostructures offers faster kinetics, reversibility, and economic viability but the strength of H₂ adsorption and storage capacity of the medium needs further improvements. Ideally, these systems should be capable to bind H₂ with adsorption energies in the range of

0.2–0.6 eV and practical gravimetric capacities of > 5 wt%. Hereby, we modeled and explored the low-dimensional nanostructures for enhanced H_2 uptake. In this context, the strategies of metal doping and molecular functionalization were considered. The decoration of light metal adatoms on nanosheets, graphdiyne (GDY), siligraphene (SiC_7), boron carbide (BC_3), and boron phosphide (BP) sheets could enhance the strength of the interaction between H_2 and the host, therefore, the adsorption energies in most cases were ultimate for practical implementations in the fuel cell. Each metal center could hold multiple H_2 leading to reasonably high gravimetric capacities of the storage system. The high storage capacity was further facilitated by the large surface-to-volume ratio of the nanostructures. Similar to atomic doping, the storage capacity and interaction of H_2 could be enhanced by molecular functionalization. For instance, h-BN sheets functionalized with OLi and ONa, and carbon nanotubes (CNTs) with polyolithiated species could capture a large amount of H_2 with adequate strength of adsorption. Based on our DFT computations, we proposed that our functionalized nanosheets and CNTs are worth experimental exploration for H_2 storage.

In *Chapter 4*, the potential of 2D S-functionalized nitride MXenes (Ti_2NS_2 and V_2NS_2) and light metal functionalized boron carbide (BC_3) sheets is studied for the sensing and capturing of various hazardous molecules. The adsorption of molecules on the nanosheets leads to a change in the electronic properties, geometry, and surface work function of the sheets. The computed adsorption energies of molecules on MXene sheets depicted that both Ti_2NS_2 and V_2NS_2 sheets could efficiently sense NO and NO_2 molecules with intermediate adsorption strength, which is suitable for fast recovery of the nanosheets after gas sensing. MXene sheets were least sensitive to the carbon-containing gases CO, CO_2 , and CH_4 . On the contrary, we depicted higher sensitivity of metal-doped BC_3 sheets for the aforementioned carbonaceous gases. From DFT computations, it is predicted that S-functionalized nitride MXenes and metallized BC_3 sheets can serve as the efficient 2D gas sensors for particular gas molecules.

Subsequently, *Chapter 5* is dedicated to investigating the effect of foreign adatoms on the properties of 2D materials. The structural, electronic, and mechanical properties of 2D materials are greatly influenced due to the adsorption of adatoms, which serves as an important tool for materials design for various applications. In this regard, we studied the stanene monolayer with thirty-one different atoms belonging to different groups of the periodic table. Adsorption of adatoms leads to the structural deformations, charge redistributions, variation in the surface work function, and the electronic properties of the stanene monolayer, which were computed with the help of DFT computations.

In a nutshell, this thesis work is based on the DFT computations which serve as a guideline for the design of efficient H_2 storage and gas sensing materials. The practical implementation of the H_2 storage system can turn the

vision of the H₂ economy into a reality that can consequently promise environmental sustainability. Meanwhile, the sensing and monitoring of harmful pollutants and controlling their concentration in the air play an important role for health and safety.

7 Svensk Sammanfattning

Den globala konsumtionen av fossila bränslen är oroväckande hög vilket pekar mot en eventuell energikris inom en snar framtid. Förutom den kraftiga minskningen av fossila reserver hör förbränningen av kolväten samman med utsläpp av miljöfarliga gaser. Den globala uppvärmningen som orsakas av utsläpp av koldioxid och andra växthusgaser kräver inte bara en hållbar, ekonomisk och miljövänlig energitillverkning utan också utveckling av effektiva gassensorer och infångare. I denna avhandling designas och undersöks lågdimensionella material för tillämpningar inom grön energitillverkning och gassensorer. Vi har använt oss av van der Waals (vdW) densitetsfunktionsteori (DFT) för att beräkna och modifiera egenskaper hos material på atomnivå för tillämpningar inom ovan nämnda områden.

Den detaljerade teoretisk bakgrunden för DFT tillsammans med beräkningsmetoder presenteras i kapitel 2. Interaktionen mellan molekyler och nanostrukturer styrs vanligtvis av krafter med lång räckvidd som inte ingår i Kohn-Sham (KS) DFT. Därför har vdW-korrigeringsfaktorer inkluderats i DFT-beräkningarna för att ge en exakt bild av den totala fria energin i systemen och andra materialegenskaper.

I kapitel 3 diskuteras strategier för materialbaserad vätgaslagring (H_2) tillsammans med utmaningar och begränsningar för kemisorption och fysisorptionstekniker. H_2 är en idealisk energibärare på grund av sitt höga energiinnehåll och sin rikliga naturliga förekomst. Som en miljövänlig, ekonomisk och hållbar energibärare har H_2 möjlighet att helt ersätta fossila bränslen i energitillämpningar. Dock är H_2 svår att lagra för praktiska tillämpningar på grund av att den i normaltillståndet existerar i gasfas och har en låg volymdensiteten. Konventionella sätt att lagra H_2 , via förvätskning och komprimering, anses vara osäkra och ekonomiskt olönsamma.

Kemisk lagring av väte i fasta material, såsom metallhydrider, förefaller vara en genomförbar lösning för H_2 -lagring, men otillräcklig adsorptionsenergi och ogynnsam adsorption/desorptions-kinetik försämrar reversibiliteten och dess praktiska användbarhet. Den fysiska adsorptionen av H_2 på ytorna av nanostrukturer erbjuder snabbare kinetik, reversibilitet och ekonomisk lönsamhet, men styrkan på H_2 -adsorptionen och lagringskapaciteten hos mediet behöver förbättras ytterligare. I bästa fall borde dessa system kunna binda H_2 med en adsorptionsenergi i intervallet 0,2-0,6 eV och en praktiska gravimetrisk kapacitet på >5 viktprocent. Därför modellerade och undersökte vi lågdimensionella nanostrukturer för ett förbättrat H_2 -upptag. I denna kontext

överbägsdes metoderna metall doping och molekylär funktionalisering. Dekorationen av lätta metalladatomer på nanoskikt, grafdiyn (GDY), siligrafen (SiC₇), borkarbid (BC₃) och borfosfid (BP)-skikt, kunde öka styrkan i interaktionen mellan H₂ och värdmaterialen, och genom detta var adsorption-senergierna i de flesta fall helt ändamålsenliga för praktisk tillämpning i bränsleceller. Varje metallcenter kunde hålla flera H₂ vilket gav tillräckligt hög gravimetrisk kapacitet hos systemen. Den höga lagringskapaciteten underlättades ytterligare genom nanostrukturernas stora yta-till-volymförhållande. Liksom vid atomdoping kunde lagringskapaciteten och interaktionen av H₂ förbättras genom molekylär funktionalisering. Exempelvis kunde h-BN-skikt som funktionaliserats med OLi och ONa, och kolnanorör (CNT) med polyli-tierade ämnen, fånga stora mängder H₂ med tillräcklig adsorptionsstyrka. Med utgångspunkt i våra DFT-beräkningar föreslog vi att våra funktionaliserade nanoskikt och CNT:er är värda att undersöka experimentellt för vätagaslagring.

I kapitel 4 studeras 2D S-funktionaliserade nitrid- MXener (Ti₂NS₂ och V₂NS₂) och lättmetallfunktionaliserade borkarbidskikt (BC₃) med avseende på deras potential för att känna av och fånga in olika skadliga molekyler. Adsorptionen av molekyler på nanoskikten leder till förändringar i skiktens elektroniska egenskaper, geometri och arbetsfunktion. De beräknade adsorptionsenergierna för molekyler på MXene-skikten visar att både Ti₂NS₂- och V₂NS₂-skikt effektivt kunde känna av NO- och NO₂-molekyler med mellanliggande bindningsstyrka, vilket är lämpligt för snabb återhämtning av nanoskikten efter gasavkänning. MXene-skikten var minst känsliga för de kolhaltiga gaserna CO, CO₂ och CH₄. Å andra sidan påvisade vi högre känslighet hos metall dopade BC₃-skikt för de kolhaltiga gaserna. Från DFT-beräkningar framgår att S-funktionaliserade nitrid- MXener och metalliserade BC₃-skikt bör kunna fungera som effektiva 2D-gassensorer för specifika gasmolekyler.

Därefter ägnas kapitel 5 åt att undersöka effekten av främmande adatomer på 2D-materialens egenskaper. De strukturella, elektroniska och mekaniska egenskaperna hos 2D-material påverkas i hög grad av adsorptionen av adatomer, något som utgör ett viktigt verktyg vid materialdesign för olika tillämpningar. På detta sätt studerade vi stanene monolager med trettioett olika atomer tillhörande olika grupper i det periodiska systemet. Adsorption av adatomer leder till strukturella deformationer, laddningsomfördelningar, variationer i ytans arbetsfunktion och i de elektroniska egenskaperna för stanen monolagren, vilket beräknades med hjälp av DFT-beräkningar.

Sammanfattningsvis är denna avhandling baserad på DFT-beräkningar vilka fungerar som guider för utformningen av effektiva H₂-lagrings- och gas-sensor-material. Den praktiska tillämpningen av H₂-lagringssystem kan förvandla visionen om H₂-ekonomin till en verklighet som följaktligen kan lova miljömässig hållbarhet. På samma gång spelar avkänning och övervakning av skadliga föroreningar och kontroll av deras koncentration i luften en viktig roll för hälsan och säkerheten.

8 Acknowledgements

Before anything else, I want to thank Almighty Allah for His countless blessings. This is all because of Allah's mercy that I joined the research group of amazing people in some of the really unpredictable circumstances.

I am immensely grateful to many people who helped me throughout my PhD journey but my supervisor **Prof. Rajeiv Ahuja** comes at the first place. I find myself short of words when I want to say thanks to him. I am indebted to him because he accepted me as his PhD student and always helped me in my work. I am also very much grateful to my co-supervisor **Wei Luo** for bearing with me. She is one of the sweetest, kindest and most understanding people in Uppsala. Thanks to my co-supervisor **Anton Greigorev** who always helped me to understand difficult concepts of solid-state physics and supported me for my research work.

I am highly indebted to my research mentor and a very good friend **Tanveer Hussain** who recommended me for PhD in his former group and guided me in the research work throughout these years. This PhD thesis and most of my research work could not be completed without his immense support, patience and guidance. Thanks to all the coauthors in my publications who co-operated with me and helped me to publish our papers in good journals. I would also like to thank my office/corridor mates and friends Vivek, Giane, Pritam, Nabil, Deobrat, Emel, Fairoja, Arnab, M.S Islam (Late), Xiaoyong, Erna, Raghuveer and Sudip for always cooperating with me, sharing knowledge with me, and making my time memorable at Uppsala university. Vivek, Giane, and Puspamitra were the most supportive friends throughout these four years and especially during the thesis writing. Special thanks to my amazing friend Elisabet Petersson for her help with writing the thesis summary in Swedish language. Bundle of thanks to all the colleagues and friends who read parts of my thesis and suggested corrections, especially Tanveer, Arnab, Vivekanand (Vivek), Deobrat, and Emil. I am grateful to my teacher in Pakistan Muhammad Usman for his help for getting the PhD position in Uppsala University. Thanks to my previous co-supervisor Anders Hallen for his kindness and support in my toughest times.

I want to say bundle of thanks to the lovely couple Jasim (bhai) and Shumaila Sayyab for their support during my stay in Uppsala. Many thanks to my lovely friends Puspamitra, Myskal, Omneya, Sadhna, Shreemoi, and Elisabeth Petersson for giving me beautiful memories in Uppsala. My friends in Stockholm Amber, Maryam, Asifa, Tayyaba, Sumera, and Sitwat made my life

beautiful and made me realize that we can enjoy even when life is burdened with so many responsibilities. I am immensely thankful to all these friends for their love and support. I might have forgotten to mention someone, but I would always be thankful to those who supported me in any way.

Thanks to my family, especially my loving husband Umair for his support and love. This thesis work was never possible without his endless support and compromises. Thanks to the most amazing kid on earth, my love, my soul, my dear son Usaim for making my dark days brighter with his beautiful presence. Acknowledgement section would be incomplete without thanking my parents and siblings (especially my sister Rabia) whose love and prayers were besides me at all the times. I am nothing without my parent's support, prayers, and love. My father has played the most vital role in my success and I want to say special thanks to him because he is the biggest reason for any progress that I have ever made in my life.

Reference

- [1] World Bank, Guide to climate change adaptation in cities. Science, 2011.
- [2] A. L. Daniau, P. J. Bartlein, S. P. Harrison, I. C. Prentice, S. Brewer, ... and S. Mooney, Predictability of biomass burning in response to climate changes, *Global Biogeochem. Cycles*, 26(4), 2012.
- [3] International Energy Agency, *World Energy Outlook 2011*, OECD Publishing, Paris, 2011.
- [4] S. Shafiee and E. Topal, When will fossil fuel reserves be diminished?, *Energy Policy*, 37(1):181-189, 2009.
- [5] N. Kannan and D. Vakeesan, Solar energy for future world, *Renewable Sustainable Energy Rev.*, 62:1092-1105, 2016.
- [6] M. S. Dresselhaus and I. L. Thomas, Alternative energy technologies, *Nature*, 414(6861):332-337, 2001.
- [7] I. G. Mason, S. C. Page, and A. G. Williamson, A 100% renewable electricity generation system for New Zealand utilising hydro, wind, geothermal and biomass resources, *Energy Policy*, 38(8):3973-3984, 2010.
- [8] M. Salah, P. Murphy, C. Hall, C. Francis, R. Kerr, and M. Fabretto, Pure silicon thin-film anodes for lithium-ion batteries: A review, *J. Power Sources*, 414:48-67, 2019.
- [9] M. Hirscher, V. A. Yartys, V. A. Barrico, ... and Y. W. Cho, Materials for hydrogen-based energy storage – past, recent progress and future outlook, *J. Alloys Compd*, 827:153548, 2020.
- [10] C. Lang, Y. Jia, and X. Yao, Recent advances in liquid-phase chemical hydrogen storage, *Energy Storage Mater.*, 26:290-312, 2020.
- [11] R. Coontz and B. Hanson, Not so simple, *Science*, 304(5686):957, 2004.
- [12] A. Züttel, A. Remhof, A. Borgschulte, and O. Friedrichs, Hydrogen: The future energy carrier, *Philosophical Transactions of the Royal Society A: Mathematical, Physical and Engineering Sciences*, 368(1923):3329-3342, 2010.
- [13] S. Pacala and R. Socolow, Stabilization wedges: Solving the climate problem for the next 50 years with current technologies, *Science*, 305:398, 2004.
- [14] P. L. Bora, R. Ahmad, ... and A. K. Singh, Remarkable enhancement in hydrogen storage on free-standing Ti_3B and BC_3 supported Ti_3 clusters, *Int. J. Hydrogen Energy*, 40(2):1054-1061, 2015.
- [15] T. Hussain, B. Pathak, M. Ramzan, T. A. Maark, ... and R. Ahuja, Calcium doped graphane as a hydrogen storage material, *Appl. Phys. Lett.*, 100(18):183902, 2012.
- [16] C. E. Thomas, Fuel cell and battery electric vehicles compared, *Int. J. Hydrogen Energy*, 34(15):6005-6020, 2009.
- [17] J. M. Andújar and F. Segura, Fuel cells: History and updating. A walk along two centuries, *Renewable Sustainable Energy Rev.*, 13(9):2309-2322, 2009.

- [18] L. E. Klebanoff, Hydrogen storage technology: Materials and applications, CRC Press. 2012.
- [19] C. Acar and I. Dincer, Comparative assessment of hydrogen production methods from renewable and non-renewable sources, *Int. J. Hydrogen Energy*, 39(1):1-12, 2014.
- [20] D. Jing, L. Guo, L. Zhao, X. Zhang, H. Liu, ... and K. Zhang, Efficient solar hydrogen production by photocatalytic water splitting: From fundamental study to pilot demonstration, *Int. J. Hydrogen Energy*, 35(13):7087-7097, 2010.
- [21] K. Maeda and K. Domen, Photocatalytic water splitting: Recent progress and future challenges, *J. Phys. Chem. Lett.*, 1(18):2655-2661, 2010.
- [22] S. Y. Tee, K. Y. Win, W. S. Teo, L. D. Koh, ... and M. Y. Han, Recent progress in energy-driven water splitting, *Adv. Science*, 4(5):1600337, 2017.
- [23] T. Q. Hua, R. K. Ahluwalia, J. K. Peng, M. Kromer, ... and J. Sinha, Technical assessment of compressed hydrogen storage tank systems for automotive applications, *Int. J. Hydrogen Energy*, 36(4):3037-3049, 2011.
- [24] M. T. I. Khan, M. Monde, and T. Setoguchi, Hydrogen gas filling into an actual tank at high pressure and optimization of its thermal characteristics, *J. Therm. Sci.*, 18(3):235-240, 2009.
- [25] P. Xu, J. Zheng, H. Chen, and P. Liu, Optimal design of high pressure hydrogen storage vessel using an adaptive genetic algorithm, *Int. J. Hydrogen Energy*, 35(7):2840-2846, 2010.
- [26] S. W. Jorgensen, Hydrogen storage tanks for vehicles: Recent progress and current status, *Curr. Opin. Solid State Mater. Sci.*, 15(2):39-43, 2011.
- [27] D. J. Durbin and C. Malardier-Jugroot, Review of hydrogen storage techniques for on board vehicle applications, *Int. J. Hydrogen Energy*, 38(34):14595-14617, 2013.
- [28] S. M. Aceves, F. Espinoza-Loza, ... and O. Kircher, High-density automotive hydrogen storage with cryogenic capable pressure vessels, *Int. J. Hydrogen Energy*, 35(3):1219-1226, 2010.
- [29] R. K. Ahluwalia, T. Q. Hua, J. K. Peng, ... and M. Gardiner, Technical assessment of cryo-compressed hydrogen storage tank systems for automotive applications, *Int. J. Hydrogen Energy*, 35(9):4171-4184, 2010.
- [30] C. L. Aardahl and S. D. Rassat, Overview of systems considerations for on-board chemical hydrogen storage, *Int. J. Hydrogen Energy*, 34(16):6676-6683, 2009.
- [31] K. Gandhi, D. K. Dixit, and B. K. Dixit, Hydrogen desorption energies of Aluminum hydride (Al_nH_{3n}) clusters, *Phys. B Condens. Matter*, 405(15):3075-3081, 2010.
- [32] M. Resan, M. D. Hampton, J. K. Lomness, and D. K. Slattey, Effect of Ti_xAl_y catalysts on hydrogen storage properties of LiAlH_4 and NaAlH_4 , *Int. J. Hydrogen Energy*, 30(13-14):1417-1421, 2005.
- [33] B. Bogdanović, M. Felderhoff, A. Pommerin, F. Schüth, and N. Spielkamp, Advanced hydrogen-storage materials based on Sc, Ce-, and Pr-doped NaAlH_4 , *Adv. Mater.*, 18(9):1198-1201, 2006.
- [34] H. Morioka, K. Kakizaki, S. C. Chung, and A. Yamada, Reversible hydrogen decomposition of KAlH_4 , *J. Alloys Compd.*, 353(1-2):310-314, 2003.

- [35] T. Ichikawa, N. Hanada, S. Isobe, H. Leng, and H. Fujii, Mechanism of novel reaction from LiNH_2 and LiH to Li_2NH and H_2 as a promising hydrogen storage system, *J. Phys. Chem. B*, 108(23):7887-7892, 2004.
- [36] S. A. Jin, Y. S. Lee, J. H. Shim, and Y. W. Cho, Reversible hydrogen storage in $\text{LiBH}_4\text{-MH}_2$ ($\text{M} = \text{Ce, Ca}$) composites, *J. Phys. Chem. C*, 112(25):9520-9524, 2008.
- [37] T. Kelkar and S. Pal, A computational study of electronic structure, thermodynamics and kinetics of hydrogen desorption from Al- and Si-doped α -, γ -, and β - MgH_2 , *J. Mater. Chem.*, 19(25):4348-4355, 2009.
- [38] P. K. Cheekatamarla and C. M. Finnerty, Reforming catalysts for hydrogen generation in fuel cell applications, *J. Power Sources*, 160(1):490-499, 2006.
- [39] E. Newson and T. B. Truong, Low-temperature catalytic partial oxidation of hydrocarbons ($\text{C}_1\text{-C}_{10}$) for hydrogen production, *Int. J. Hydrogen Energy*, 28(12):1379-1386, 2003.
- [40] T. Umegaki, J. M. Yan, X. B. Zhang, H. Shioyama, N. Kuriyama, and Q. Xu, Boron and nitrogen-based chemical hydrogen storage materials, *Int. J. Hydrogen Energy*, 34(5):2303-2311, 2009.
- [41] T. Yildirim and S. Ciraci, Titanium-decorated carbon nanotubes as a potential high-capacity hydrogen storage medium, *Phys. Rev. Lett.*, 94(17):175501, 2005.
- [42] E. Durgun, S. Ciraci, W. Zhou, and T. Yildirim, Transition-metal-ethylene complexes as high-capacity hydrogen-storage media, *Phys. Rev. Lett.*, 97(22):226102, 2006.
- [43] A. Blomqvist, C. M. Araújo, P. Srepusharawoot, and R. Ahuja, Li-decorated metal-organic framework 5: A route to achieving a suitable hydrogen storage medium, *Proc. Natl. Acad. Sci. U. S. A.*, 104(51):20173-20176, 2007.
- [44] S. A. Shevlin and Z. X. Guo, Hydrogen sorption in defective hexagonal BN sheets and BN nanotubes, *Phys. Rev. B - Condens. Matter Mater. Phys.*, 76(2):024104, 2007.
- [45] N. S. Venkataramanan, R. V. Belosludov, R. Note, R. Sahara, H. Mizuseki, and Y. Kawazoe, Theoretical investigation on the alkali-metal doped BN fullerene as a material for hydrogen storage, *Chem. Phys.*, 377(1-3):54-59, 2010.
- [46] G. F. Fine, L. M. Cavanagh, A. Afonja, and R. Binions, Metal oxide semiconductor gas sensors in environmental monitoring, *Sensors*, 10(6):5469-5502, 2010.
- [47] K. Suematsu, Y. Shin. N. Ma, ... and K. Shimano, Pulse-driven micro gas sensor fitted with clustered Pd/SnO_2 nanoparticles, *Anal. Chem.*, 87(16):8407-8415, 2015.
- [48] K. H. An, S. Y. Jeong, H. R. Hwang, and Y. H. Lee, Enhanced sensitivity of a gas sensor incorporating single-walled carbon nanotube-polypyrrole nanocomposites, *Adv. Mater.*, 16(12):1005-1009, 2004.
- [49] K. Cheah, M. Forsyth, and V. T. Truong, Ordering and stability in conducting polypyrrole, *Synth. Met.*, 94(2):215-219, 1998.
- [50] R. M. Martin, *Electronic structure basic theory and practical methods*, Cambridge University Press, 2004.
- [51] M. Born and R. Oppenheimer, Zur quantentheorie der molekeln, *Ann. Phys.*, 389(20):457-484, 1927.

- [52] L. H. Thomas, The calculation of atomic fields, *Math. Proc. Cambridge Philos. Soc.*, 23(5):542-548, 1927.
- [53] E. Fermi, A statistical method for the determination of some atomic properties and the application of this method to the theory of the periodic system of elements, *Z. Phys.*, 48(73):29, 1975.
- [54] P. A. M. Dirac, Note on exchange phenomena in the Thomas atom, *Math. Proc. Cambridge Philos. Soc.*, 26(3):376-385, 1930.
- [55] P. Hohenberg and W. Kohn, Inhomogeneous electron gas, *Phys. Rev.* 136(3B):B864-B871, 1964.
- [56] W. Kohn and L. J. Sham, Self-consistent equations including exchange and correlation effects, *Phys. Rev.*, 140(4A):A1133, 1965.
- [57] E. Engel and R. M. Dreizler, *Density Functional Theory: An advanced course*, *Theor. Math. Phys.*, Berlin Springer, 2011.
- [58] A. Szabo and N. Ostlund, *Modern quantum chemistry: Introduction to advanced electronic structure theory*, Courier Corporation, 2012.
- [59] P. Giannozzi, *Numerical methods in quantum mechanics (Lecture Notes)*, www.fisica.uniud.it, 2014.
- [60] J. P. Perdew and A. Zunger, Self-interaction correction to density-functional approximations for many-electron systems, *Phys. Rev. B*, 23(10):5048, 1981.
- [61] J. P. Perdew and Y. Wang, Accurate and simple analytic representation of the electron-gas correlation energy, *Phys. Rev. B*, 45(23), 13244, 1992.
- [62] S. H. Vosko, L. Wilk, and M. Nusair, Accurate spin-dependent electron liquid correlation energies for local spin density calculations: a critical analysis, *Can. J. Phys.*, 58(8):1200-1211, 1980.
- [63] A. D. Becke, Density-functional exchange-energy approximation with correct asymptotic behavior, *Phys. Rev. A*, 38(6):3098, 1988.
- [64] J. P. Perdew, K. Burke, and M. Ernzerhof, Generalized gradient approximation made simple, *Phys. Rev. Lett.*, 77(18):3865, 1996.
- [65] A. D. Becke, Density-functional thermochemistry. V. Systematic optimization of exchange-correlation functionals, *J. Chem. Phys.*, 107(20):8554-8560, 1997.
- [66] B. Hammer, M. Scheffler, K. W. Jacobsen, and J. K. Nørskov, Multidimensional potential energy surface for H₂ dissociation over Cu(111), *Phys. Rev. Lett.*, 73(10):1400, 1994.
- [67] E. Penev, P. Kratzer, and M. Scheffler, Effect of the cluster size in modeling the H₂ desorption and dissociative adsorption on Si(001), *J. Chem. Phys.*, 110(8):3986-3994, 1999.
- [68] J. Klimeš and A. Michaelides, Perspective: Advances and challenges in treating van der Waals dispersion forces in density functional theory, *J. Chem. Phys.* 137(12):120901, 2012.
- [69] P. Mori-Sánchez, A. J. Cohen, and W. Yang, Localization and delocalization errors in density functional theory and implications for band-gap prediction, *Phys. Rev. Lett.*, 100(14):146401, 2008.
- [70] A. J. Cohen, P. Mori-Sánchez, and W. Yang, Insights into current limitations of density functional theory, *Science*, 321(5890):792-794, 2008.
- [71] S. Kristyán and P. Pulay, Can (semi)local density functional theory account for the London dispersion forces?, *Chem. Phys. Lett.*, 229(3):175-180, 1994.

- [72] P. Hobza, J. šponer, and T. Reschel, Density functional theory and molecular clusters, *J. Comput. Chem.*, 16(11):1315-1325, 1995.
- [73] J. M. Pérez-Jordá and A. D. Becke, A density-functional study of van der Waals forces: rare gas diatomics, *Chem. Phys. Lett.*, 233(1-2):134-137, 1995.
- [74] J. F. Dobson and T. Gould, Calculation of dispersion energies, *J. Phys. Condensed Matter*, 24(7):073201, 2012.
- [75] S. Grimme, Accurate description of van der Waals complexes by density functional theory including empirical corrections, *J. Comput. Chem.*, 25(12): 1463-1473, 2004.
- [76] S. Grimme, Semiempirical GGA-type density functional constructed with a long-range dispersion correction, *J. Comput. Chem.*, 27(15):1787-1799, 2006.
- [77] S. Grimme, J. Antony, S. Ehrlich, and H. Krieg, A consistent and accurate ab initio parametrization of density functional dispersion correction (DFT-D) for the 94 elements H-Pu, *J. Chem. Phys.*, 132(15):154104, 2010.
- [78] A. Tkatchenko and M. Scheffler, Accurate molecular van der Waals interactions from ground-state electron density and free-atom reference data, *Phys. Rev. Lett.*, 102(7):073005, 2009.
- [79] A. D. Becke and E. R. Johnson, A density-functional model of the dispersion interaction, *J. Chem. Phys.*, 123(15):154101, 2005.
- [80] V. N. W. Ashcroft and N. D. Mermin, *Solid state physics*, Holt, Rinehart and Winston, New York, 1976.
- [81] P. E. Blöchl, Projector augmented-wave method, *Phys. Rev. B*, 50(24):17953, 1994.
- [82] M. W. Finnis and J. E. Sinclair, A simple empirical N-body potential for transition metals, *Philos. Mag. A*, 50(1):45-55, 1984.
- [83] J. Tersoff, Modeling solid-state chemistry: Interatomic potentials for multi-component systems, *Phys. Rev. B*, 39(8):5566, 1989.
- [84] International Energy Agency, *Key World Energy Statistics 2006*, Int. Energy Agency, 2006.
- [85] L. Schlapbach and A. Züttel, Hydrogen-storage materials for mobile applications, *Nature*, 265-270, 2001.
- [86] Department of Energy, DOE technical targets for onboard hydrogen storage for light duty vehicles, <https://www.energy.gov/eere/fuelcells/doe-technical-targets-onboard-hydrogen-storage-light-duty-vehicles>, Last accessed on 20-04-2020.
- [87] S. Satyapal, DOE hydrogen and fuel cells program, FY2015 Annual Progress Report, 2015.
- [88] V. Bérubé, G. Radtke, M. Dresselhaus, and G. Chen, Size effects on the hydrogen storage properties of nanostructured metal hydrides: A review, *Int. J. Energy Research*. 31(6-7):637-663, 2007.
- [89] J. J. Vajo, F. Mertens, C. C. Ahn, R. C. Bowman, and B. Fultz, Altering hydrogen storage properties by hydride destabilization through alloy formation: LiH and MgH₂ destabilized with Si, *J. Phys. Chem. B*, 108(37):13977-13983, 2004.
- [90] W. Grochala and P. P. Edwards, Thermal decomposition of the non-interstitial hydrides for the storage and production of hydrogen, *Chem. Rev.*, 104(3):1283-1316, 2004.

- [91] F. Y. Naumkin and D. J. Wales, Beryllium cluster cages endohedrally doped by hydrogen: $H_2@Be_n$ ($8 \leq n \leq 14$), *Int. J. Quantum Chem.*, 112(18):3068-3075, 2012.
- [92] P. Larsson, C. M. Araújo, J. A. Larsson, P. Jena, and R. Ahuja, Role of catalysts in dehydrogenation of MgH_2 nanoclusters, *Proc. Natl. Acad. Sci. U. S. A.*, 105(24):8227-8231, 2008.
- [93] A. Züttel, P. Wenger, S. Rentsch, P. Sudan, P. Mauron, and C. Emmenegger, $LiBH_4$ a new hydrogen storage material, *J. Power Sources*, 118(1-2):1-7, 2003.
- [94] K. Takahashi, S. Isobe, and S. Ohnuki, Chemisorption of hydrogen on Fe clusters through hybrid bonding mechanisms, *Appl. Phys. Lett.*, 102(11):113108, 2013.
- [95] C. X. Shang, M. Bououdina, and Z. X. Guo, Structural stability of mechanically alloyed ($Mg + 10 Nb$) and ($MgH_2 + 10 Nb$) powder mixtures, *J. Alloys Compd.*, 349(1-2):217-223, 2003.
- [96] J. Charbonnier, P. De Rango, D. Fruchart,... and P. Vulliet, Hydrogenation of transition element additives (Ti, V) during ball milling of magnesium hydride, *J. Alloys Compd.*, 383(1-2):205-208, 2004.
- [97] G. Walker, *Solid-state hydrogen storage: Materials and chemistry*, Elsevier, 2008.
- [98] J. Graetz and J. J. Reilly, Kinetically stabilized hydrogen storage materials, *Scripta Materialia*, 56(10):835-839, 2007.
- [99] K. Chlopek, C. Frommen, A. Léon, O. Zabara, and M. Fichtner, Synthesis and properties of magnesium tetrahydroborate, $Mg(BH_4)_2$, *J. Mater. Chem.*, 17(33):3496-3503, 2007.
- [100] E. Jeon and Y. W. Cho, Mechanochemical synthesis and thermal decomposition of zinc borohydride, *J. Alloys Compd.*, 422(1-2):273-275, 2006.
- [101] H. M. Cheng, Q. H. Yang, and C. Liu, Hydrogen storage in carbon nanotubes, *Carbon*, 39(10):1447-1454, 2001.
- [102] Hirscher, Michael, M. Becher, M. Haluska,... and S. Roth, Are carbon nanostructures an efficient hydrogen storage medium?, *J. Alloys Compd.*, 356:433-437, 2003.
- [103] M. Yoon, S. Yang, C. Hicke, E. Wang, D. Geohegan, and Z. Zhang, Calcium as the superior coating metal in functionalization of carbon fullerenes for high-capacity hydrogen storage, *Phys. Rev. Lett.*, 100(20):206806, 2008.
- [104] Q. Sun, Q. Wang, P. Jena, and Y. Kawazoe, Clustering of Ti on a C_{60} surface and its effect on hydrogen storage, *J. Am. Chem. Soc.*, 127(42):14582-14583, 2005.
- [105] L. J. Murray, M. Dincă, and J. R. Long, Hydrogen storage in metal-organic frameworks, *Chem. Soc. Rev.*, 38(5):1294-1314, 2009.
- [106] J. L. C. Rowsell and O. M. Yaghi, Strategies for hydrogen storage in metal-organic frameworks, *Angewandte Chemie - International Edition*, 44(30):4670-4679, 2005.
- [107] Z. Yang, Y. Xia, and R. Mokaya, Enhanced hydrogen storage capacity of high surface area zeolite-like carbon materials, *J. Am. Chem. Soc.*, 129(6):1673-1679, 2007.

- [108] Y. Lin, F. Ding, and B. I. Yakobson, Hydrogen storage by spillover on graphene as a phase nucleation process, *Phys. Rev. B - Condens. Matter Mater. Phys.*, 78(4):041402, 2008.
- [109] T. Hussain, B. Pathak, T. A. Maark, C. M. Araujo, R. H. Scheicher, and R. Ahuja, Ab initio study of lithium-doped graphane for hydrogen storage, *EPL (Europhysics Letters)*, 92(2):27013, 2011.
- [110] C. Tang, Y. Bando, X. Ding, S. Qi, and D. Golberg, Catalyzed collapse and enhanced hydrogen storage of BN nanotubes, *J. Am. Chem. Soc.*, 124(49):14550-14551, 2002.
- [111] F. Ding and B. I. Yakobson, Challenges in hydrogen adsorptions: From physisorption to chemisorption, *Frontiers of Physics*, 6(2)142-150, 2011.
- [112] M. Dincă and J. R. Long, Hydrogen storage in microporous metal-organic frameworks with exposed metal sites, *Angewandte Chemie - International Edition.*, 47(36):6766-6779, 2008.
- [113] M. Dincă, A. F. Yu, and J. R. Long, Microporous metal-organic frameworks incorporating 1, 4-benzeneditetrazolate: Syntheses, structures, and hydrogen storage properties, *J. Am. Chem. Soc.*, 128(27):8904-8913 2006.
- [114] M. Long, L. Tang, D. Wang, Y. Li, and Z. Shuai, Electronic structure and carrier mobility in graphdiyne sheet and nanoribbons: Theoretical predictions, *ACS Nano*, 5(4):2593-2600, 2011.
- [115] Z. W. Chen, Z. Wen, and Q. Jiang, Rational design of Ag₃₈ cluster supported by graphdiyne for catalytic CO oxidation, *J. Phys. Chem. C*, 121(6):3463-3468, 2017.
- [116] Q. Lv, W. Si, Z. Yang, N. Wang, Z. Tu, Y. Yi, Nitrogen-doped porous graphdiyne: a highly efficient metal-free electrocatalyst for oxygen reduction reaction, *ACS Appl. Mater. Interfaces*, 9(35):29744-29752, 2017.
- [117] G. Mpourmpakis, G. E. Froudakis, G. P. Lithoxoos, and J. Samios, SiC nanotubes: A novel material for hydrogen storage, *Nano Lett.*, 6(8):1581-1582, 2006.
- [118] Z. Shi, Z. Zhang, A. Kutana, and B. I. Yakobson, Predicting two-dimensional silicon carbide monolayers, *ACS Nano*, 9(10):9802-9809, 2015.
- [119] H. Dong, L. Zhou, T. Frauenheim, T. Hou, S. T. Lee, and Y. Li, SiC₇ siligraphene: A novel donor material with extraordinary sunlight absorption, *Nanoscale*, 8(13):6994-6999, 2016.
- [120] C. Kittel, Introduction to solid state physics, 8th edition, Wiley Sons, New York, NY, 2004.
- [121] J. Hu, L. Zhao, J. Du, and G. Jiang, Adsorption of rare gases on pristine and doped phosphorene, *Appl. Surf. Sci.*, 504:144326, 2020.
- [122] P. Panigrahi, A. Kumar, A. Kartan, R. Ahuja, and T. Hussain, Remarkable improvement in hydrogen storage capacities of two-dimensional carbon nitride (g-C₃N₄) nanosheets under selected transition metal doping, *Int. J. Hydrogen Energy*, 45(4):3035-3045, 2020.
- [123] W. Q. Deng, X. Xu, and W. A. Goddard, New alkali doped pillared carbon materials designed to achieve practical reversible hydrogen storage for transportation, *Phys. Rev. Lett.*, 92(16):166103, 2004.
- [124] S. Nachimuthu, P. J. Lai, E. G. Leggesse, and J. C. Jiang, A first principles study on boron-doped graphene decorated by Ni-Ti-Mg atoms for enhanced hydrogen storage performance, *Sci. Rep.*, 5(1):1-8, 2015.

- [125] S. Nachimuthu, P. J. Lai, and J. C. Jiang, Efficient hydrogen storage in boron doped graphene decorated by transition metals - A first-principles study, *Carbon*, 73:132-140, 2014.
- [126] D. Çakir, D. Kecik, H. Sahin, E. Durgun, and F. M. Peeters, Realization of a p-n junction in a single layer boron-phosphide, *Phys. Chem. Chem. Phys.*, 17(19):13013-13020, 2015.
- [127] H. R. Jiang, W. Shyy, M. Liu, L. Wei, M. C. Wu, and T. S. Zhao, Boron phosphide monolayer as a potential anode material for alkali metal-based batteries, *J. Mater. Chem. A*, 5(2):672-679, 2017.
- [128] K. Wang, Z. Liu, X. Wang, and X. Cui, Enhancement of hydrogen binding affinity with low ionization energy Li_2F coating on C_{60} to improve hydrogen storage capacity, *Int. J. Hydrogen Energy*, 39(28):15639-15645, 2014.
- [129] Q. Peng, G. Chen, H. Mizuseki, and Y. Kawazoe, Hydrogen storage capacity of $\text{C}_{60}(\text{OM})_{12}$ ($\text{M}=\text{Li}$ and Na) clusters, *J. Chem. Phys.*, 131(21):214505, 2009.
- [130] C. H. Wu, H. Kudo, and H. R. Ihle, Thermochemical properties of gaseous Li_3O and Li_2O_2 , *J. Chem. Phys.*, 70(4):1815-1820, 1979.
- [131] P. V. R. Schleyer, E.-U. Wuerthwein, E. Kaufman, T. Clark, and J. A. Pople, Effectively hypervalent molecules. 2. Lithium carbide (CLi_5), Lithium carbide (CLi_6), and the related effectively hypervalent first row molecules, $\text{CLi}_{5-n}\text{H}_n$ and $\text{CLi}_{6-n}\text{H}_n$, *J. Am. Chem. Soc.*, 105(18):5930-5932, 1983.
- [132] H. Kudo, Observation of hypervalent CLi_6 by Knudsen-effusion mass spectrometry, *Nature*, 355(6359):432-434, 1992.
- [133] S. Er., G. A. De Wijs, and G. Brocks, Hydrogen storage by polyolithiated molecules and nanostructures, *J. Phys. Chem. C*, 113(20):8997-9002, 2009.
- [134] R. Davy, E. Skoumbourdis, and T. Kompanchenko, Complexation of hydrogen by lithium: Structures, energies and vibrational spectra of $\text{Li}^+(\text{H}_2)_n$ ($n = 1-4$), $\text{Li-H}(\text{H}_2)_m$ and $\text{Li-H}^+(\text{H}_2)_m$ ($m = 1-3$), *Mol. Phys.*, 97(12):1263-1271, 1999.
- [135] A. C. Dillon, K. M. Jones, T. A. Bekkedahl, C. H. Kiang, D. S. Bethune, and M. J. Heben, Storage of hydrogen in single-walled carbon nanotubes, *Nature*, 386(6623):377-379, 1997.
- [136] M. Rzepka, P. Lamp, and M. A. De La Casa-Lillo, Physisorption of hydrogen on microporous carbon and carbon nanotubes, *J. Phys. Chem. B*, 102(52):10894-10898, 1998.
- [137] G. G. Tibbetts, G. P. Meisner, and C. H. Olk, Hydrogen storage capacity of carbon nanotubes, filaments, and vapor-grown fibers, *Carbon*, 39(15):2291-2301, 2001.
- [138] H. S. Kim, H. Lee, K. S. Han,... and J. K. Kang, Hydrogen storage in Ni nanoparticle-dispersed multiwalled carbon nanotubes, *J. Phys. Chem. B*, 109(18):8983-8986, 2005.
- [139] L. Chen, Y. Zhang, N. Koratkar, P. Jena, and S. K. Nayak, First-principles study of interaction of molecular hydrogen with Li-doped carbon nanotube peapod structures, *Phys. Rev. B - Condens. Matter Mater. Phys.*, 77(3):033405, 2008.
- [140] D. Silambarasan, V. J. Surya, V. Vasu, and K. Iyakutti, One-step process of hydrogen storage in single walled carbon nanotubes-tin oxide nano composite, *Int. J. Hydrogen Energy*, 38(10):4011-4016, 2013.

- [141] J. Beheshtian, A. A. Peyghan, and Z. Bagheri, Hydrogen dissociation on diene-functionalized carbon nanotubes, *J. Mol. Model.*, 19(1):255-261, 2013.
- [142] F. Guérin, G. Abril, S. Richard, B. Burhan, C. Reynouard, P. Seyler and R. Delmas, Methane and carbon dioxide emissions from tropical reservoirs: Significance of downstream rivers, *Geophys. Res. Lett.*, 33(21), 2006.
- [143] J. J. Roberts, R. A. Wood, and R. S. Haszeldine, Assessing the health risks of natural CO₂ seeps in Italy, *Proc. Natl. Acad. Sci. U. S. A.*, 108(40):16545-16548, 2011.
- [144] T. F. Booze, T. E. Reinhardt, S. J. Quiring, and R. D. Ottmar, A Screening-Level Assessment of the health risks of chronic smoke exposure for wildland firefighters, *J. Occup. Environ. Hyg.*, 1(2):296-305, 2004.
- [145] K. J. Donham and W. J. Pependorf, Ambient levels of selected gases inside swine confinement buildings, *Am. Ind. Hyg. Assoc. J.*, 46(11):658-661, 1985.
- [146] N. Barsan and U. Weimar, Conduction model of metal oxide gas sensors, *J. Electroceramics*, 7(3):143-167, 2001.
- [147] S. Yang, C. Jiang, and S. huai Wei, Gas sensing in 2D materials, *Appl. Phys. Rev.*, 4(2):021304, 2017.
- [148] Q. Yue, Z. Shao, S. Chang, and J. Li, Adsorption of gas molecules on monolayer MoS₂ and effect of applied electric field, *Nanoscale Res. Lett.*, 8(1):425, 2013.
- [149] A. S. Rad, First principles study of Al-doped graphene as nanostructure adsorbent for NO₂ and N₂O: DFT calculations, *Appl. Surf. Sci.*, 357:1217-1224, 2015.
- [150] G. S. Rao, T. Hussain, M. S. Islam, M. Aagynbaeva, D. Gupta, P. Panigrahi, R. Ahuja, Adsorption mechanism of graphene-like ZnO monolayer towards CO₂ molecules: Enhanced CO₂ capture, *Nanotechnology*, 27(1):015502, 2015.
- [151] X. F. Yu, Y. C. Li, J. B. Cheng, Z. B. Liu, Q. Z. Li, W. Z. Li, X. Yang and B. Xiao, Monolayer Ti₂CO₂: A promising candidate for NH₃ sensor or capturer with high sensitivity and selectivity, *ACS Appl. Mater. Interfaces*, 7(24):13707-13713, 2015.
- [152] C. Wang, L. Yin, L. Zhang, D. Xiang, and R. Gao, Metal oxide gas sensors: Sensitivity and influencing factors, *Sensors*, 10(3):2088-2106, 2010.
- [153] S. J. Kim, H. J. Koh, C. E. Ren, O. Kwon,.... and Y. Gogotsi, Metallic Ti₃C₂T_x MXene gas sensors with ultrahigh signal-to-noise ratio, *ACS Nano*, 12(2):986-993, 2018.
- [154] M. Naguib, V. N. Mochalin, M. W. Barsoum, and Y. Gogotsi, MXenes: A new family of two-dimensional materials, *Adv. Mater.*, 26(7):992-1005, 2014.
- [155] L. Wang, Efficient U(VI) reduction and sequestration by Ti₂CT_x MXene, *Environ. Sci. Technol.*, 52(18):10748-10756, 2018.
- [156] Q. Tang, Z. Zhou, and P. Shen, Are MXenes promising anode materials for Li ion batteries? Computational studies on electronic properties and Li storage capability of Ti₃C₂ and Ti₃C₂X₂ (X = F, OH) monolayer, *J. Am. Chem. Soc.*, 134(40):16909-16916, 2012.
- [157] H. Zhang, G. Yang, X. Zuo, H. Tang, Q. Yang, and G. Li, Computational studies on the structural, electronic and optical properties of graphene-like

- MXenes (M_2CT_2 , $M = Ti, Zr, Hf$; $T = O, F, OH$) and their potential applications as visible-light driven photocatalysts, *J. Mater. Chem. A*, 4(33):12913-12920, 2016.
- [158] M. R. Lukatskaya, O. Mashtalir, C. Ren,... and Y. Gogotsi, Cation intercalation and high volumetric capacitance of two-dimensional titanium carbide, *Science*, 341(6153):1502-1505, 2013.
 - [159] Q. Hu, D. Sun, Q. Wu,... and J. He, MXene: A new family of promising hydrogen storage medium, *J. Phys. Chem. A*, 117(51):14253-14260, 2013.
 - [160] V. Shukla, N. K. Jena, S. R. Naqvi, W. Luo, and R. Ahuja, Modelling high-performing batteries with Mxenes: The case of S-functionalized two-dimensional nitride Mxene electrode, *Nano Energy*, 58:877-885, 2019.
 - [161] M. Naguib, M. Kurtoglu, V. Presser,... and M. W. Barsoum, Two-Dimensional Nanocrystals Produced by Exfoliation of Ti_3AlC_2 , *Adv. materials*, 23(37):4248-4253, 2011.
 - [162] M. Naguib, O. Mashtalir, J. Carle,... and M. W. Barsoum, Two-dimensional transition metal carbides, *ACS Nano*, 6(2):1322-1331, 2012.
 - [163] Y. H. Kim, S. J. Kim, Y. J. Kim,... and H. W. Jang, Self-activated transparent all-graphene gas sensor with endurance to humidity and mechanical bending, *ACS Nano*, 9(10):10453-10460, 2015.
 - [164] Y. Wang, J. Chen, and X. Huang, Adsorption behavior of B-doped/N-doped graphene sheets toward NO_2 , NO and NH_3 molecules: A first-principles study, *Phys. Status Solidi Curr. Top. Solid State Phys.*, 14(3-4):1600110, 2017.
 - [165] Z. M. Ao, J. Yang, S. Li, and Q. Jiang, Enhancement of CO detection in Al doped graphene, *Chem. Phys. Lett.*, 461(4-6):276-279, 2008.
 - [166] T. Hussain, P. Panigrahi, and R. Ahuja, Enriching physisorption of H_2S and NH_3 gases on a graphene sheet by doping with Li adatoms, *Phys. Chem. Chem. Phys.*, 16(17):8100-8105, 2014.
 - [167] P. K. Nayak, Two-dimensional materials - Synthesis, characterization and potential applications, BoD (Books on Demand), 2016.
 - [168] X. Chen, C. Tan, Q. Yang, R. Meng, S. Zang, Q. Liang, M. Cai and J. Jiang, Ab Initio study of the adsorption of small molecules on Stanene, *J. Phys. Chem. C*, 120(26):13987-13994, 2016.
 - [169] S. C. Wu, G. Shan, and B. Yan, Prediction of near-room-temperature quantum anomalous hall effect on honeycomb materials, *Phys. Rev. Lett.*, 113(25):256401, 2014.
 - [170] S. R. Naqvi, T. Hussain, W. Luo, and R. Ahuja, Metallized siligraphene nanosheets (SiC_7) as high capacity hydrogen storage materials, *Nano Res.*, 11(7):3802-3813, 2018.
 - [171] S. R. Naqvi, T. Hussain, P. Panigrahi, W. Luo, and R. Ahuja, Manipulating energy storage characteristics of ultrathin boron carbide monolayer under varied scandium doping, *RSC Adv.*, 7(14):8598-8605, 2017.
 - [172] S. R. Naqvi, T. Hussain, S. R. Gollu, W. Luo, and R. Ahuja, Applied Surface Science Superior sensitivity of metal functionalized boron carbide (BC_3) monolayer towards carbonaceous pollutants, *Appl. Surf. Sci.*, 512:145637, 2020.
 - [173] Q. Xiang, J. Yu, W. Wang, and M. Jaroniec, Nitrogen self-doped nanosized TiO_2 sheets with exposed $\{001\}$ facets for enhanced visible-light photocatalytic activity, *Chem. Commun.*, 47(24):6906-6909, 2011.

Acta Universitatis Upsaliensis

*Digital Comprehensive Summaries of Uppsala Dissertations
from the Faculty of Science and Technology 1938*

Editor: The Dean of the Faculty of Science and Technology

A doctoral dissertation from the Faculty of Science and Technology, Uppsala University, is usually a summary of a number of papers. A few copies of the complete dissertation are kept at major Swedish research libraries, while the summary alone is distributed internationally through the series Digital Comprehensive Summaries of Uppsala Dissertations from the Faculty of Science and Technology. (Prior to January, 2005, the series was published under the title "Comprehensive Summaries of Uppsala Dissertations from the Faculty of Science and Technology".)



ACTA
UNIVERSITATIS
UPSALIENSIS
UPPSALA
2020

Distribution: publications.uu.se
urn:nbn:se:uu:diva-409006